JOHANNES GUTENBERG UNIVERSITÄT MAINZ

Upscaling of fluid flow in fractured rock masses

Dissertation
zur Erlangung des Grades
"Doktor der Naturwissenschaften"
im Promotionsfach Geologie/Paläontologie
am Fachbereich Chemie, Pharmazie, Geographie und Geowissenschaften
der Johannes Gutenberg Universität Mainz

von

Maximilian Oskar Kottwitz
geboren in Wiesbaden

Mainz, 2021

1. Gutachter:
Prof. Dr. Boris J. P. Kaus

2. Gutachter:
Dr. Anton A. Popov

Tag der mündlichen Prüfung:
11.10.2021

"Qui bene bibet bene vivit.
Qui bene vivit bene dormit.
Qui bene dormit non peccat.
Qui non peccat in cælum venit.
Ergo qui bene bibet in cælum venit. "

- Latin saying

Abstract

Numerical modeling of fluid flow is applied to assess hydraulic reservoir properties and their uncertainties for decades and thus proven to be an essential part of geo-resource exploration. Yet, one of its main challenges is how to properly translate flow from the pore- to the reservoir-scale - the so-called upscaling problem. For fractured reservoirs, where flow predominantly localizes in large individuals or connected networks of open discontinuities, this may be cumbersome, as their mechanically induced structures are often complex and inherently multi-scale. Field-data-constrained stochastic fracture network models with reduced-order discrete fracture representations are the most common approach to model multi-scale fracture systems in 3D. Upscaling their effective properties like permeability or porosity crucially relies on parametrizations prescribing an average flow behavior at the single fracture scale to model network-scale flow. Advancing the accuracy and applicability of these techniques to model fluid flow in fractured rock masses from the fracture to the network scale is the main scope of this thesis.

Initially, a new scheme to quantify the non-planar geometry of single fractures is established as a basis to derive a refined parallel plate parametrization from the results of numerous 3D Stokes flow simulations in synthetically generated fractures. The accuracy of this prediction scheme depends on the ratio between the fracture size and the length scale of the long-range correlations in its aperture field. Analyzing these correlation lengths in 3D-imaged, naturally occurring discontinuities revealed that simple linear relationships to their mean apertures serve as an approximation of this property in network-scale models. Prior knowledge of the fractures correlation length enables determining the lowest scale in the upscaling process, at which using reduced-order fracture network models with parameterized flow behavior accounting for in-fracture flow variability is statistically valid.

As a next step, the flow complexities in fracture intersections were explored in numerical simulations, revealing that they represent preferred pathways for fluid migration compared to the crossing fractures and that, if its orientation aligns with the applied pressure gradient and its length is close to the system size, it enhances effective permeabilities. A newly established pipe-flow parametrization scheme enables including these effects into network-scale simulations. There, computational limitations for networks with many fractures and incorporating hydraulic properties of the matrix represent current issues in discrete fracture network flow methods. Developing a new single continuum discretization method for discrete fracture networks that includes parametrizations for fracture and intersection flow to generate high-resolved grids of individual, fully anisotropic permeability tensors helps tackle these problems. Combining this with a newly developed, massively parallelized finite-element Darcy-flow code capable of incorporating anisotropic permeability tensors at the local scale improves the efficiency of upscaling hydraulic properties of fractured-porous media. Furthermore, the provided discretization guidelines help to avoid the resolution dependency of single continuum methods while conserving the anisotropic character of complex multi-scale fracture networks during the upscaling process.

Zusammenfassung

Das numerische Modellieren von Fluidfluss in Gesteinen ist seit Jahren ein wichtiges Werkzeug in der Exploration von Georessourcen, um die hydraulischen Eigenschaften poröser und geklüfteter Reservoire besser abschätzen zu können. Eine der größten Herausforderungen dabei ist das korrekte Hochskalieren (engl.: *upscaling*) der Strömungseigenschaften von der Poren- auf die Reservoir-Skala. Besonders in bruchdominierten Reservoiren erweist sich das oft als schwierig, da die hydraulischen Eigenschaften maßgeblich von einzelnen oder in Netzwerken verbundenen Klüften beeinflusst werden. Aufgrund des skalenübergreifenden Auftretens hydraulisch aktiver Diskontinuitäten werden oftmals auf Felddaten gestützte, stochastische Bruchnetzwerkmodelle mit diskreten Bruchdarstellungen reduzierter Ordnung verwendet, um mehrskalige Bruchsysteme in 3D zu modellieren. Das durchschnittliche Fließverhalten auf der Kluft- und Poren-Skala wird dann mit Hilfe von Parametrisierungen vorgegeben und der effektive Permeabilitäts-Tensor des Bruchsystems durch einen Darcy-Ansatz berechnet. Die Verbesserung der Genauigkeit und Anwendbarkeit dieser Techniken zur Modellierung von Fluidfluss in geklüfteten Gesteinsmassen von der Kluft- bis zur Netzwerkskala ist das Hauptanliegen dieser Arbeit.

Zunächst wird ein neues Schema zur Quantifizierung der nicht-planaren Geometrie einzelner Klüfte erarbeitet. Dies dient als Grundlage für die Herleitung einer verfeinerten Parametrisierung der Kluft-Permeabilität auf Basis zahlreicher 3D-Stokes-Simulationen in synthetisch generierten Klüften dient. Es wird gezeigt, dass die Genauigkeit dieser Parametrisierung vom Verhältnis zwischen der Größe des Risses und der internen Korrelations-Länge des Aperture-Feldes abhängt. Die Analyse dieser Korrelationslänge in 3D-verbildlichten realen Diskontinuitäten ergab, dass einfache lineare Beziehungen zu deren mittleren Aperturen verwendet werden können, um diesen Parameter in Modellen auf Bruchnetzwerk-Skala vorzugeben. Dadurch ist es möglich, die niedrigste Skala im Hochskalierungs-Prozess zu bestimmen, bei der die Verwendung von diskreten Bruchnetzwerkmodellen mit parametrisiertem Strömungsverhalten auf der Kluft-Skala statistisch aussagekräftig ist.

Anschließend wird die Komplexität von Fluidströmungen in Kreuzungen von Klüften mit 3D-Stokes-Simulationen untersucht. Dabei wird gezeigt, dass Kluft-Kreuzungen bevorzugte Wegsamkeiten für Fluide darstellen, wenn deren räumliche Orientierung ähnlich zur allgemeinen Fließrichtung ausgerichtet ist und deren Länge nah an der Gesamtlänge des betrachteten Systems liegt. Mit Hilfe einer neu entwickelten Parametrisierung der Kluft-Kreuzungs-Permeabilität kann dieser Effekt in Fluidfluss-Simulationen auf der Bruchnetzwerk-Skala integriert werden. Dort stellen rechnerische Einschränkungen für Bruchsysteme mit einer hohen Anzahl an Klüften und die Integration der hydraulischen Eigenschaften der Matrix aktuelle Probleme klassischer Methoden zur Fluidfluss-Simulation in diskreten Bruchnetzwerk-Modellen dar. Um diese zu lösen, wird eine neue Diskretisierungs-Methode entwickelt, die Parametrisierungen für Kluft- und Kluft-Kreuzungs-Permeabilitäten heranzieht, um Kontinuums-Gitter-Modelle mit anisotropen Permeabilitäts-Tensoren aus diskreten Bruchnetzwerk-Modellen zu erstellen. Mit Hilfe einer neu entwickelten, massiv parallelisierten Finite-Elemente-Software, die in der Lage ist, anisotrope Permeabilitäts-Tensore auf lokaler Ebene mit einzubeziehen, können dann effektive Permeabilitäten von Bruchnetzwerken mit einem Darcy-Ansatz ermittelt werden. Dabei wird die für Kontinuums-Methoden oft beobachtete Auflösungsabhängigkeit untersucht, um Diskretisierungs-Vorgaben zur akkuraten, Anisotropie-konservierenden Hochskalierung hydraulischer Eigenschaften mehrskaliger Bruchnetzwerke abzuleiten.

Contents

List of Figures

List of Tables

Dedicated to Franziska

Chapter 1

Introduction

Assessing the permeabilities of fractured reservoirs or fault zones is a key challenge of reservoir engineering in the fields of natural resource production (Khelifa et al., 2014; Ghosh et al., 2020), geothermal energy recovery (Bodvarsson et al., 1985; Patterson et al., 2020), nuclear waste disposal (SKB, 1992; La Pointe et al., 1995) and CO2-sequestration (IPCC, 2005; March et al., 2018). Thus, advancements in this research field have, besides their scientific benefits, a profound societal impact by ensuring long-term resource supplies and counterbalancing the challenges induced by climate change.
A common characteristic of fractured reservoirs is a low permeable host rock, which causes most fluids to migrate through connected networks or large individuals of open discontinuities (Barenblatt et al., 1960; Warren and Root, 1963), more generally known as fractures. They can be observed at the smallest scales by microscopes, up to the largest scales from satellite images (Hardebol et al., 2015; Espejel et al., 2020). Thus, fractured reservoirs exhibit a strong multi-scale character with distinct hydraulic features across scales, distinguishing them from conventional, unfractured reservoirs. Numerous studies have revealed the structural heterogeneities of naturally occurring fracture networks (Dershowitz and Einstein, 1988; Odling et al., 1999; Bonnet et al., 2001; Neuman, 2005). They represent essential parts of brittle fault zones in the upper crust, whose structural appearance relates to their mechanical origin (Fossen et al., 2007; Faulkner et al., 2010). Non-stationary and potentially anisotropic hydraulic properties across scales are the direct consequences of these structural complexities and difficult to predict only from outcrop- and production-data or well-tests (Berkowitz, 2002; Bourbiaux et al., 2005). Thus, numerical methods to model fluid flow and predict effective permeabilities have gained increasing popularity throughout the past decades to complement field and laboratory measurements while assessing the hydraulic properties of the reservoir.

1.1 Fluid flow modeling in fractured rocks

Modeling fluid flow in fractured or porous media can broadly be separated into direct- and continuum-flow modeling approaches. For direct-flow modeling, the incompressible Navier-Stokes equations (e.g., eq. 4.3.35 in Bear, 1972) usually provide the foundation to model the migration of a single phase of fluid through a digital representation of the rock's pore space. For most subsurface flow conditions, it is common to assume laminar flow conditions, i.e., Reynolds numbers below 1 - 10 (Bear, 1972), which enables the use of the Stokes equations

for similar tasks. After discretizing these equations with, for example, finite difference (e.g., Strikwerda, 1984; Kaus et al., 2016), finite element (e.g., Girault and Raviart, 1986; Zienkiewicz and Taylor, 2000) or finite volume (e.g., LeVeque, 2002; Perić, 2020) techniques and applying pressure boundary conditions, one can solve for the velocity distribution within the digital representation of the rocks pore space, under the assumption that the rock matrix is fully impermeable. Volume averaging of the velocities (e.g., Osorno et al., 2015) and substituting into Darcy's law for flow through porous media (Darcy, 1856) yields an directional permeability value that has been proven to reflect experimental measurements, if resolved sufficiently (e.g., Eichheimer et al., 2019; Eichheimer et al., 2020). Alternatively, Lattice-Boltzmann techniques are applied to solve similar problems (e.g., Jin et al., 2017; Zambrano et al., 2019). While direct-flow modeling is a well-established method in the field of digital rock physics (DRP, e.g., Andrä et al., 2013a; Schepp et al., 2020) to compute effective properties of imaged rocks, its limitation lies in the applicable scale. The techniques to obtain the required digital representations of the rocks pore space, usually done with high-resolution X-ray computed tomography (HRXCT) or micro-CT (μCT) (Andrä et al., 2013a; Cnudde and Boone, 2013), are limited in their maximum scannable size and respective trade-off to resolution, i.e., medical CT-scans of drill-cores (e.g., St-Onge et al., 2007). Hence, direct-flow modeling is only applicable to small scales (nanometer to a couple of decimeters). For larger scales, continuum-flow modeling approaches serve to simulate fluid flow and compute effective permeabilities. There, the concepts for flow through porous media proposed by Darcy (1856) serve as the basis to describe the hydraulic structure of rocks and model the pressure drop therein. Originated from a set of flow-through experiments through soil columns, Darcy derived his famous formula relating the flow through a porous medium to the applied pressure drop, fluid properties, and its permeability. The latter represents an intrinsic property of the medium that averages the resistance to flow over a certain volume. Neuman (1977) has shown that the Darcy equation originates from the Navier-Stokes equation by averaging, considering a symmetric permeability tensor for a homogeneous medium and the assumption of an incompressible, iso-thermal Newtonian fluid flowing in laminar and steady-state conditions. Thus, the Darcy equation represents an averaged version of the Stokes equations, and the transition between direct- and continuum-flow modeling provides the initial step in the upscaling process. There, the goal is to find an effective permeability tensor for a certain local area of a fine grid model to be inserted into a global coarse grid model that is computationally easier to solve (e.g., Zhou et al., 2010). Several methods exist to perform upscaling tasks (Christie and Blunt, 2001; Farmer, 2002), whereas flow-based upscaling techniques with either periodic or linear-gradient pressure boundary conditions are the most accurate compared to averaging techniques (e.g., Renard and De Marsily, 1997; Hauge et al., 2012; Lie, 2019). Yet, the use of the Darcy equation to upscale and predict fluid flow rests on the assumption that the porous medium is more or less homogeneous and the domain is a representative elementary volume (REV, e.g., Bear, 1972), i.e., the variance of the mediums effective properties is low for the current volume. According to Long et al. (1982) and Oda (1985), this behavior is given for fractured-porous media as well, if the rocks are homogeneously and densely fractured. However, the multi-scale character of fracture networks interferes with this assumption if fractures span throughout the whole domain of interest (Long

et al., 1982). Hence, either the size of a potential REV has to be determined for each fractured rock mass individually before finding the appropriate coarse grid scale (Chen et al., 2008; Azizmohammadi and Matthäi, 2017) or large scale features have to be explicitly represented in the upscaling process (Berre et al., 2019). Thus, several numerical methods to obtain effective permeability tensors of fractured-porous media were developed in the past decades (Renard and De Marsily, 1997; Berre et al., 2019). They account for the complex spatial arrangement of fractures by (1) either explicitly representing every single fracture with reduced-order models (2D lines or 3D planes) in the computational mesh (Klimczak et al., 2010; Dreuzy et al., 2012; Hyman et al., 2015; Maillot et al., 2016; Alghalandis, 2017) or (2) generate a grid of so-called equivalent (block) permeability tensors (as defined by Durlofsky, 1991, this is equal to the effective permeability tensor, if an REV exists at the considered scale and otherwise provides an accurate basis for further uspacling) that are derived based on all fractures that intersect each computational cell (Long et al., 1982; Oda, 1985; La Pointe et al., 1995; Jackson et al., 2000; Svensson, 2001; Chen et al., 2015; Sweeney et al., 2020). Leung et al. (2012) and Hadgu et al. (2017) have showed, that both discretization methods deliver comparable results and hence are suitable to provide accurate upscaled hydraulic representations of fractured-porous media for more sophisticated reservoir engineering tools like multi-phase flow or multi-physics coupled solvers (Lemonnier and Bourbiaux, 2010; Kolditz et al., 2016).

1.2 Single fracture permeability

The hydraulic response to pressure changes of individual fractures represents the primary control of the reservoirs' hydraulic properties. Assuming that a fracture consists of two parallel plates separated by a constant aperture, one can analytical solve the Stokes equations (e.g., Bear, 1972) by extending the 1D Poiseuille-flow solution throughout the domain of the idealized fracture. Integrating the resulting velocities and substituting them into Darcy's law yields the well-known cubic law (Lomize, 1951; Snow, 1969; Witherspoon et al., 1980) relating the permeability of the fracture to its aperture. Many experimental and numerical studies have investigated this relationship to provide functional corrections, accounting for the non-planar structure of naturally occurring fractures. Barton and Choubey (1977) experimentally derived standardized profiles with individual joint roughness coefficients (JRC) accounting for hydraulic and mechanical effects of the non-planar fracture morphology. These coefficients can be determined by visually comparing a profile drawn from a fracture surface to the standardized profiles to relate the hydraulic aperture from mechanically measured apertures (Barton et al., 1985; Barton and Quadros, 1997). Numerical fluid flow simulations in synthetic or imaged fractures provide an alternative, more quantitative tool to obtain hydraulic apertures of irregular fractures. Early attempts conducted 2D simulations of the Reynolds equation and derived functional corrections to the cubic law based on the mean and standard deviation of the aperture field (Patir and Cheng, 1978; Brown, 1987; Mourzenko et al., 1995; Zimmerman and Bodvarsson, 1996; Oron and Berkowitz, 1998). While these parametrizations well-captured permeability reductions due to flow channeling induced by increasing closure of the fracture, 3D Navier-Stokes or Lattice Boltzmann simulations (Brush and Thomson, 2003; Jin et al., 2017;

Kling et al., 2017; Kluge et al., 2017) revealed their non-unique behavior for permeability predictions. Fracture surface features protruding into the aperture field accumulate drag force at the fluid-rock interface that impedes fluid flow and consequently reduce fracture permeability (Foroughi et al., 2018; Mourzenko et al., 2018). Thus, incorporating the morphology of the individual fracture surfaces and their degree of mismatch next to its aperture field for fracture permeability predictions (Brown, 1995) is highly important. The surface roughness of fractures is well described by self-affine fractal models (Power et al., 1987; Power and Tullis, 1991; Schmittbuhl et al., 1993; Schmittbuhl et al., 1995; Candela et al., 2009) with scaling (or Hurst) exponents ranging between 0.3 and 0.8 (Boffa et al., 1998; Ponson et al., 2007; Bouchaud, 1997; Candela et al., 2012; Pluymakers et al., 2017), regardless of rock type and opening mode. The aperture between two juxtaposed fracture surfaces follows the same scaling, assuming both surfaces are uncorrelated. In nature, the self-affine scaling is only present up to a certain length scale, above which the aperture tends to be well correlated and independent of observation scale (Brown and Scholz, 1985; Glover et al., 1998b). The presence of this correlation length often depends on the shear displacement during fracturing, assuming two perfectly mated surfaces at nucleation stage (Wang et al., 1988; Brown, 1995; Plouraboué et al., 1995; Méheust and Schmittbuhl, 2000). However, fluid-rock interactions like dissolution/erosion (Durham et al., 2001; Kaufmann et al., 2016; Chen et al., 2019) or mineral growth (Noiriel et al., 2010; Kling et al., 2017) bear the potential to alter the surface properties of fractures significantly and should theoretically modify the correlation length as well. Statistically, the ratio of system size to aperture correlation length affects the variability of the average hydraulic behavior of similar fracture populations (Méheust and Schmittbuhl, 2000; Méheust and Schmittbuhl, 2001; Méheust and Schmittbuhl, 2003) and thus needs to be investigated in real data to be able to parameterize fracture permeability in the upscaling process.

1.3 Fracture network permeability

Fractured reservoirs display pronounced multi-scale characteristics, as fractures scale from the nanometer- to reservoir-scale (Goldscheider et al., 2010; Bertrand et al., 2015; Hardebol et al., 2015; Volatili et al., 2019). Typically, those fractures arrange in 3D networks whose structures result from diverse brittle failure mechanisms (Pollard and Aydin, 1988; Wibberley et al., 2008; Vrolijk et al., 2016). Especially in upper crustal fault zones, intense and complex fracturing occurs in regions of proximity to the fault (Fossen et al., 2007; Faulkner et al., 2010). Hence, assessing the structural heterogeneities of natural fracture networks has been one of the main scientific issues in rock engineering (Priest, 1993). The main properties such as fracture size-, orientation- and aperture-distributions (Dershowitz and Einstein, 1988; Odling et al., 1999; Bonnet et al., 2001), as well as fracture density and spacing (Dershowitz and Herda, 1992; Ortega et al., 2006), are measured from outcrops or borehole studies to quantify the statistics of a fracture network. However, acquiring deterministic knowledge of all fractures in a network is impossible, and a certain amount of extrapolation is necessary to model effective properties such as permeability or porosity of a fractured rock mass in 3D. Thus, the discrete fracture network (DFN) method provides the conceptual basis to generate stochastic realizations of

fracture network models in 2D and 3D (Long et al., 1982; Cacas et al., 1990; Bogdanov et al., 2003; Darcel et al., 2003; Lei et al., 2017). Every fracture in a network is explicitly approximated by a reduced-order model (i.e., lines in 2D or planar object like discs or rectangles in 3D) with a prescribed orientation, size, and location based on field observations. Fracture sizes are randomly sampled from predefined probability density functions, which for natural fracture systems usually follow exponential, log-normal, gamma, or power-law distributions (see Bonnet et al., 2001, and references therein). Fracture orientations in 3D are predominantly modeled with Fisher distributions (Fisher, 1953; Best and Fisher, 1979; Fisher et al., 1987) that assign a mean orientation and a parameter accounting for the spherical dispersion around the mean for a specific fracture set (see Peacock et al., 2018, for details on how to group fractures into sets based on orientation, type and age relations). The location of fractures are defined by center points, which are (1) randomly placed across the whole domain (Cacas et al., 1990; De Dreuzy et al., 2002; Lavoine et al., 2019) or distributed based on (2) mechanical constrains (Davy et al., 2013; Bonneau et al., 2016; Maillot et al., 2016) or (3) fractal models (Darcel et al., 2003; Davy et al., 2006; Akara et al., 2020). Open-source software tools such as FraNEP (Zeeb et al., 2013) or FracPaQ (Healy et al., 2017) help determine most of these properties from digitized 2D fracture-trace maps on outcrop or satellite images to complement analog field measurements. Generating 3D DFN models with open-source software is possible with, for example, FracSim3D (Xu and Dowd, 2010), dfnWorks (Hyman et al., 2015) or ADFNE (Alghalandis, 2017). The DFN method has been extensively utilized in the past to estimate effective or equivalent permeabilities (depending on whether a REV exists or not, respectively) of fracture network (see review papers of Liu et al., 2016; Lei et al., 2017). A crucial requirement to model flow through the DFN is to prescribe average hydraulic apertures of the fractures from which the cubic law relates their permeabilities (see the previous section on fracture permeability). They are most often either randomly sampled from aperture distributions measured in the field (see Gong and Rossen, 2017, and references therein) or correlated to the fracture length in a linear (Pollard and Segall, 1987; Renshaw and Park, 1997) or sub-linear (Olson, 2003; Klimczak et al., 2010) manner. Network-scale flow is then usually simulated with the single-phase Darcy equation in a discretized mesh, explicitly incorporating the structure of the DFN (Berre et al., 2019). They tend to capture anisotropic flow patterns through complex network geometries, especially if no REV exists but tend to have the drawback of high computational loads if the DFN consists of a large number of fractures. However, due to the uncertainty linked to the DFN input properties, many simulations have to be conducted to obtain a statistically valid quantification of the network's permeability. Thus, several studies suggested to mesh given DFN to an equivalent continuum model (ECM), either in 2D (Reeves et al., 2008; Botros et al., 2008; Rutqvist et al., 2013; Chen et al., 2015) or 3D (Hadgu et al., 2017; Sweeney et al., 2020), which requires less computational effort to solve. In this method, the DFN domain is subdivided into a grid of continuum cells with unique equivalent permeability tensors that are analytically derived based on all fractures that intersect the cell (Oda, 1985; Chen et al., 1999). Leung et al. (2012) and Hadgu et al. (2017) have demonstrated, that ECM methods provide similar effective permeability estimates as the DFN method, if resolved sufficiently. However, the resolution

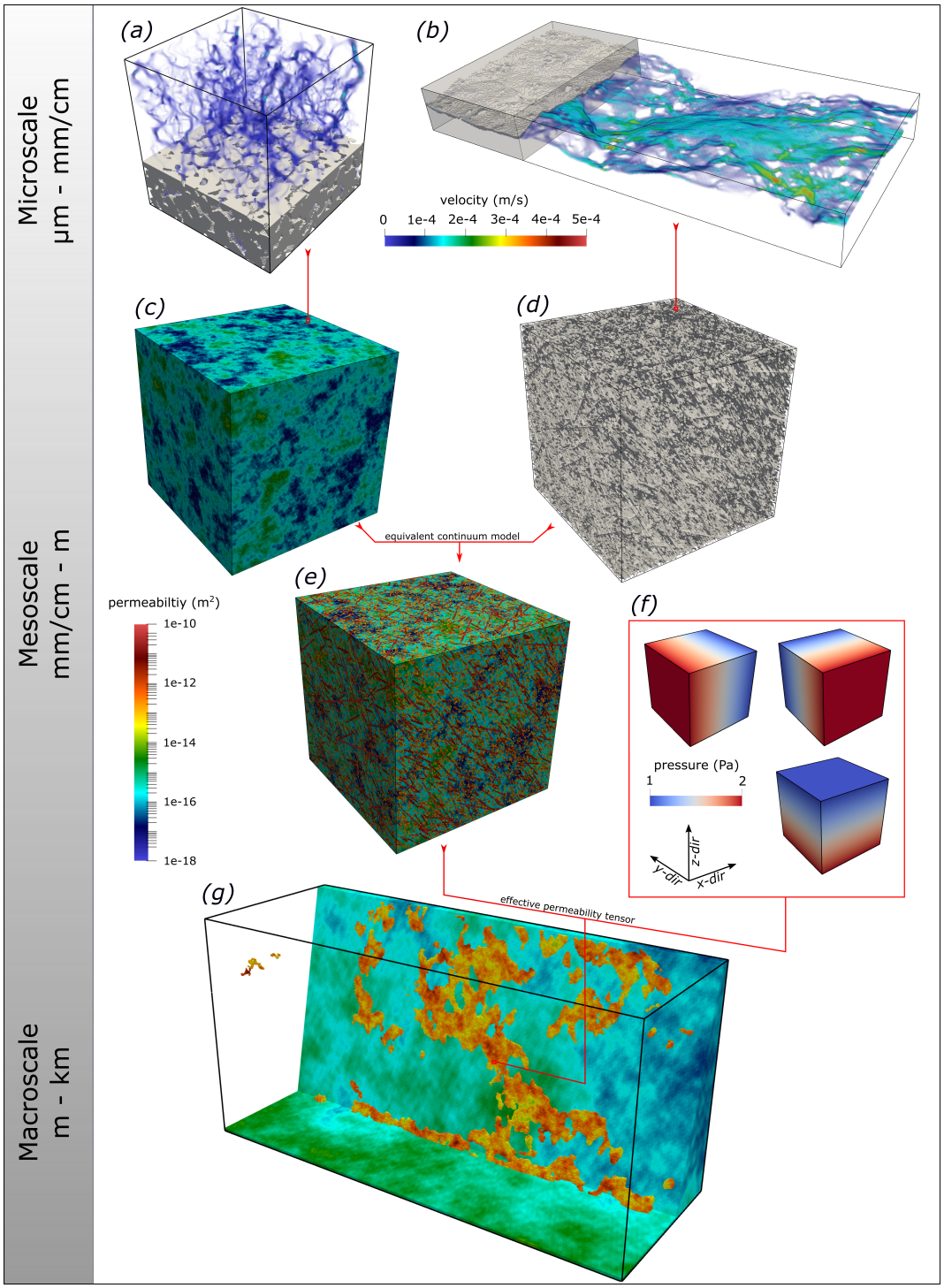

FIGURE 1.1: Sketch demonstrating permeability upscaling in fractured rock masses. Panels *a* and *b* show the velocity distributions (joined color-bar) resulting from direct-flow simulations (Stokes equation) within porespaces of the Fontainebleau sandstone benchmark dataset (e.g. Andrä et al., 2013b; Eichheimer et al., 2019) and a limestone fracture (CT-scan provided by J. Klaver), respectively, from which effective permeabilities are computed. Panel *c* displays a random permeability distribution (generated with the scripts provided by Räss et al., 2019) of a porous medium at the meso-scale (color-bar below shows permeability for *c*, *e* and *g*), whereas panel *d* shows a DFN realization of a fractured medium with 500000 fractures following a power-law size-distribution spanning three orders of magnitude (generated with ADFNE by Alghalandis, 2017). Panel *e* presents the ECM of the models shown in *c* and *d*, demonstrating the multi-scale permeability structure of fractured-porous media. In panel *f*, the linear gradient pressure boundary conditions for three iterations of continuum-flow simulations (Darcy equation) are shown, that are required to compute the effective permeability tensor of *e*. Panel *g* displays a macro-scale model of a normal fault (CT-scan of a sandbox experiment provided by J. Schmatz), that is populated with the upscaled permeability tensors obtained in a similar manner as demonstrated in *e* and *f*.

dependency of this method is still not fully understood. Furthermore, it is still an open question at which scale it is valid to prescribe average flow-behavior in the individual fractures, as Dreuzy et al. (2012) demonstrated that fracture-scale flow heterogeneity affects network flow in small fracture networks. In contrast, Makedonska et al. (2016) concluded fracture-scale flow heterogeneity has negligible effects on network flow for larger fracture networks.

1.4 Motivation

The possibility to advance my academic skills in a scientific topic that finds applications in current societal challenges (long-term resource supply & sustainable utilization and countering climate change) was one of the main reasons for me to engage in this Ph.D. opportunity. Besides this personal interest, addressing existing scientific challenges in the field of fractured reservoir modeling provides additional motivation. Benefiting from *(1)* the massively parallelized finite-difference software LaMEM (Kaus et al., 2016) developed in the geodynamics and geophysics workgroup at Johannes Gutenberg-University (JGU) Mainz, *(2)* the workgroups competency to develop massively parallelized, high-performance computing (HPC) scalable numerical software, *(3)* the computational infrastructure provided by the MOGON II cluster at JGU Mainz (hpc.uni-mainz.de) and *(4)* the remarkable field laboratory installed in the scope of the German federal ministry of education and research (BMBF) funded project PERMEA (grant no. 03G0865A), the following scientific issues provide the rationale for this thesis:

- The vast heterogeneity of fracture morphologies, expressed in varying scaling exponents and mean amplitudes of the surface roughness (e.g., Brodsky et al., 2011) is well-known, but quantifying their control on the permeability of fractures is often a non-unique problem. In addition, the coupled effects of hydraulic history (e.g., Pyrak-Nolte and Nolte, 2016) and mechanical interaction (Azizmohammadi and Matthäi, 2017) shape the aperture field of fractures and thus modify fluid flow as well. Furthermore, direct modeling approaches to predict permeabilities of imaged rocks numerically are prone to resolution dependency (Eichheimer et al., 2019) and require a certain amount of accuracy to yield valid results. Thus, analyzing the non-unique predictive behavior in high-resolution numerical simulations and providing a universal, more accurate prediction of fracture permeability while accounting for the vast heterogeneity of fracture morphologies represents a crucial requirement to model fluid flow at larger scales. Optimally, the applicability of such predictive equations, usually based on synthetic fracture models, must be confirmed with flow simulations in 3D imaged natural discontinuities.

- Diverse techniques to model fluid flow in fractured porous media have been established and verified in the past (e.g., Berre et al., 2019; Berre et al., 2020). From a technical perspective, the future challenges are focused on discretizing multi-phase flow extensions and multi-physics (thermal-hydraulic-mechanical-chemical, THMC) coupling (e.g., Kolditz et al., 2016). Yet, an accurate and upscaled initial representation of the hydraulic structure of the fractured-porous medium is a crucial requirement for these modeling approaches. However, fractured and faulted rocks display a strong multi-scale character,

e.g., fracture sizes span across several orders of magnitude (Bertrand et al., 2015), and these effects on the upscaling are not fully understood. The computational limitations of the DFN method for large multi-scale networks (Hadgu et al., 2017), the inability of some flow-solver to handle fully anisotropic permeability tensors (Sweeney et al., 2020) and the resolution dependency of equivalent continuum methods (Jackson et al., 2000; Svensson, 2001) represent unresolved issues that have to be addressed to provide accurate and statistically valid upscaled hydraulic representations of fractured reservoirs.

- The hydraulic properties of fault zones represent a crucial asset in the field of subsurface resource utilization. According to a general model, damage zones in proximity to the fault plane are often intensely fractured and thus highly conductive areas, whereas the fault core, on the contrary, is usually inhibiting flow due to the presence of gouge layers (e.g., Faulkner et al., 2010). However, these structures can get utterly complex due to multiple faulting events with potentially changing tectonic settings, leading to highly heterogeneous hydraulic properties, both spatially and temporally. Hence, combining mapping, field tests, and sampling campaigns with laboratory experiments and numerical simulations of fluid flow provides an integrative approach to accumulate multi-scale data for a hydraulic reservoir assessment and advance the understanding of flow processes through fault zones. Furthermore, direct comparisons of numerical and experimental evaluations of hydraulic properties from fracture to reservoir scale are rare but explicitly required from an engineering perspective (Thacker et al., 2004), as validating numerical methods to predict fluid flow in fractured porous media has been an everlasting topic (e.g., Cacas et al., 1990; Dershowitz et al., 1991) and crucial to proof the methodological applicability.

1.5 Thesis outline

The first chapter of this thesis summarizes the theoretical background and recent advances in multi-scale fluid flow modeling in fractured rocks and outlines the scientific rationale of this thesis. The second chapter addresses the vast diversity of natural fracture morphologies and their effects on permeability. Numerical permeability estimations of an extensive data set of synthetically generated fractures with prescribed geometries help derive a new correction factor for the cubic-law parametrization for fracture permeability that reduces the non-unique behavior of existing permeabilities. In the third chapter, this refined parametrization gets tested and confirmed on a data set of 3D imaged, naturally occurring discontinuities. Furthermore, the fractures are analyzed concerning long-range correlations in their aperture field to shed light on an often ignored but significant statistical property of fractures, as it primarily controls the non-unique behavior of predictive equations. The fourth chapter addresses flow patterns in simplified fracture intersections and provides a parametrization concept to upscale those effects to larger scales. This parametrization and the refined one for fracture permeability are integrated into a continuum method to predict effective permeability tensors of fracture networks based on numerical simulations of the 3D Darcy equation. Moreover, this method's resolution dependency is analyzed to provide discretization guidelines for obtaining the most

accurate and efficient permeability tensors that reflect the hydraulic structure of the network. The fifth and last chapter of this thesis summarizes the results of this thesis and draws some general conclusions. It follows a brief outlook that addresses how the methods developed in this thesis can be applied and validated with data obtained from a naturally occurring fractured reservoir.

1.6 Further notes

Chapters 2-4 are written such that they represent individual studies, whereas, from a thematic point of view, they are closely related. Hence, there may be some overlap in content concerning the used methodologies and introductory literature researches.
The auxiliaries used in this thesis which are not directly indicated in the text are summed up in the following. This thesis was written in *TexStudio* using the template "Masters/Doctoral Thesis" retrieved from "www.latextemplates.com". Data pre- and post-processing as well as analysis and fitting were carried out in *Matlab* and *Python*, similar as the 2D plotting (all scripts are available upon request). 3D visualizations were generated with *ParaView*, whereas all final plots where edited in *Inkscape*. English grammar was corrected with *Grammarly*.

Chapter 2

The hydraulic efficiency of single fractures: Correcting the cubic law parameterization for self-affine surface roughness and fracture closure [1]

2.1 Abstract

Quantifying the hydraulic properties of single fractures is a fundamental requirement to understand fluid flow in fractured reservoirs. For an ideal planar fracture, the effective flow is proportional to the cube of the fracture aperture. In contrast, real fractures are rarely planar, and correcting the cubic law in terms of fracture roughness has therefore been a subject of numerous studies in the past. Several empirical relationships between hydraulic and mechanical aperture have been proposed, based upon statistical variations of the aperture field. However, often they exhibit non-unique solutions, attributed to the geometrical variety of naturally occurring fractures. In this study, a non-dimensional fracture roughness quantification-scheme is acquired, opposing effective surface area against relative fracture closure. This is used to capture deviations from the cubic law as a function of quantified fracture roughness, here termed hydraulic efficiencies. For that, we combine existing methods to generate synthetic 3D fracture voxel models. Each fracture consists of two random, $25cm^2$ wide self-affine surfaces with prescribed roughness amplitude, scaling exponent, and correlation length, which are separated by varying distances to form fracture configurations that are broadly spread in the newly formed two-parameter space (mean apertures in sub-millimeter range). First, we performed a percolation analysis on 600'000 synthetic fractures to narrow down the parameter space on which to conduct fluid flow simulations. This revealed that the fractional amount of contact and the percolation probability solely depends on the relative fracture closure. Next, Stokes flow calculations are performed, using a 3D finite differences code on 6400 fracture models to compute directional permeabilities. The deviations from the cubic law prediction and their statistical variability for equal roughness configurations were quantified. The resulting 2D solution fields reveal decreasing cubic-law accordance's down to 1 % for extreme roughness

[1] This chapter was published in Solid Earth (Kottwitz, M. O., Popov, A. A., Baumann, T. S., and Kaus, B. J. P., https://doi.org/10.5194/se-11-947-2020)

configurations. We show that the non-uniqueness of the results significantly reduces if the correlation length of the aperture field is much smaller than the spatial extent of the fracture. An equation was provided that predicts the average behavior of hydraulic efficiencies and respective fracture permeabilities as a function of their statistical properties. A model to capture fluctuations around that average behavior with respect to their correlation lengths has been proposed. Numerical inaccuracies were quantified with a resolution test, revealing an error of 7 %. By this, we propose a revised parametrization for the permeability of rough single fractures, which takes numerical inaccuracies of the flow calculations into account. We show that this approach is more accurate compared to existing formulations. It can be employed to estimate the permeability of fractures if a measure of fracture roughness is available, and it can readily be incorporated in discrete fracture network modeling approaches.

2.2 Introduction

The geometrical inhomogeneities of single fractures and their effect on fluid flow remain a crucial parameter for understanding the hydraulic properties of fractured reservoirs, such as crystalline or tight carbonate rocks with nearly impermeable matrices. Hence, it has wide-ranging industrial applicability in the fields of petroleum and gas production, geothermal energy recovery, CO_2 sequestration, nuclear waste disposal, and groundwater management. Fluid flow in fractured reservoirs is commonly modeled by the discrete-fracture-network (DFN) approach (Bogdanov et al., 2003; Klimczak et al., 2010; Leung et al., 2012; Dreuzy et al., 2012), which relies on knowing the permeability of single fractures. The permeability of a single fracture is often approximated by the well-known cubic law (Snow, 1969; Witherspoon et al., 1980), assuming that a fracture is composed of two parallel plates separated by a constant aperture. However, natural fracture walls show deviations from planarity, i.e., roughness, resulting in varying apertures within the fracture plane. On top of that, fluid-rock interactions like dissolution (Durham et al., 2001), erosion (Pyrak-Nolte and Nolte, 2016) and mineral growth (Kling et al., 2017) as well as the surrounding stress field (Zimmerman and Main, 2004; Azizmohammadi and Matthäi, 2017) further modify the geometry of a fracture, causing deviations of the parallel plate assumption.

Considerable effort has been made to study the effect of fracture surface roughness on flow and reactive transport behavior. Early attempts (Patir and Cheng, 1978; Brown, 1987; Zimmerman and Bodvarsson, 1996; Oron and Berkowitz, 1998) employed the 2D Reynolds equation, a simplification of the Navier-Stokes equations, which assumes that the cubic law holds locally with the aperture varying in the $x - y$ along-fracture plane. They derived semi-empirical functions that describe the deviations from the cubic law in terms of the mean and standard deviation of the aperture field. Increasing computational power led to numerical improvements, with 3D Lattice Boltzmann (Jin et al., 2017; Foroughi et al., 2018) or Navier-Stokes (Mourzenko et al., 1995; Brush and Thomson, 2003) simulations revealing the non-uniqueness of previous functional approximations of fracture permeability. Factors such as shear displacement (Kluge et al., 2017), tortuosity, and the degree of mismatch between the opposing fracture surfaces

(Mourzenko et al., 2018) were demonstrated to affect fluid flow paths and permeabilities. Detailed analyses of exposed fracture surfaces have shown that self-affine fractal models are capable of quantifying surface roughness properties from thin-section- to outcrop-scale. Thereby, the dependence of surface roughness as a function of the observation scale is captured by their scaling exponent (the so-called Hurst exponent H). For example, mode I fractures in a porous sandstone showed H of $0.4 - 0.5$ (Boffa et al., 1998; Ponson et al., 2007). Micro-fractures in Pomeranian shale featured H of 0.3 and 0.5 (Pluymakers et al., 2017), depending on the opening mode. In other studies, H of fault surfaces (mode II fractures) tends to fall in the range of $0.6 - 0.8$ with respect to slip orientation (Power and Tullis, 1991; Schmittbuhl et al., 1995; Bouchaud, 1997; Renard et al., 2006; Candela et al., 2012), regardless of rock type. Based on this, it is commonly assumed that a fracture consists of two opposing self-affine surfaces, and the resulting aperture field follows the same scaling relationship, assuming both surfaces are uncorrelated (Plouraboué et al., 1995). However, observations of opposing fracture walls (Brown, 1995) have demonstrated that the two surfaces tend to be well correlated above a specific length scale and non-correlated below it, which poses an upper limit to the self-affine scaling in nature. Following Méheust and Schmittbuhl (2001) and Méheust and Schmittbuhl (2003), the ratio between system size L and the correlation length l_c defines whether the fracture has an intrinsic permeability or not. Their statistical approach suggested that permeabilities of uncorrelated fractures (i.e., $l_c/L = 1$) are strongly fluctuating and anisotropic for the same roughness configurations, revealing the importance of considering low l_c/L ratios to be able to quantify an intrinsic fracture permeability.
Although extensively studied, no clear mathematical relationship between fracture roughness and permeability has been derived so far, leaving the cubic law as standardized parametrization in DFN modeling approaches. Thus, an applicable refinement is desired to promote their realism to help better understanding fluid flow on a reservoir scale. In this paper, existing algorithms are used to generate a large data set of synthetic fractures covering all possible kinds of roughness configurations. Single-phase 3D Stokes flow calculations are then performed with a finite difference code, utilizing a high-performance-computing (HPC) cluster to handle the associated computational effort. By interpreting the statistical variations of the results, a refined parametrization of single fracture permeability is proposed, which is demonstrated to provide accurate predictions for the permeability of rough fractures.

2.3 Method & Data

2.3.1 Fluid flow in self-affine fractures

Generally, the flow of an incompressible Newtonian fluid is most accurately described by the Navier-Stokes equations (NSE). Assuming, that the flow is solely laminar (Reynolds numbers below unity according to Zimmerman and Bodvarsson, 1996), the fluid viscosity is constant and gravity is negligible at the system size, they reduce to the simpler Stokes equations, i.e., momentum balance (2.1) and continuity (2.2) equations, which for steady-state flow conditions

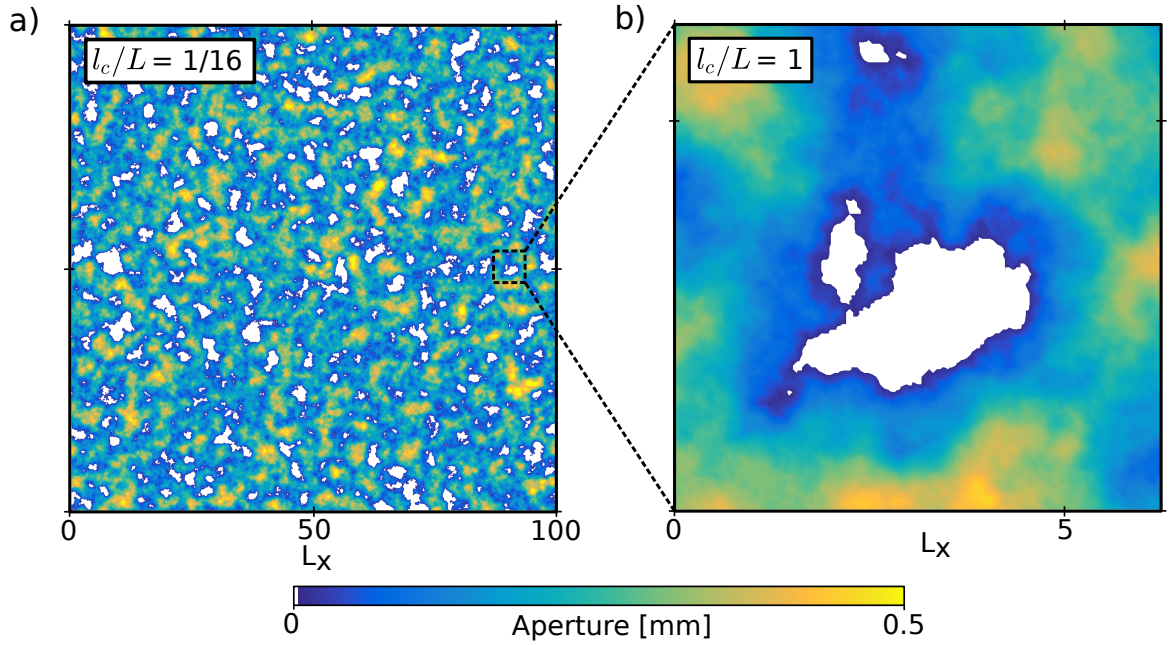

FIGURE 2.1: a) Aperture field of a synthetically generated fracture ($d = 1\ mm$, $\sigma_s = 0.5\ mm$, $H = 0.9$) with a l_c/L ratio of 1/16. b) Zoom-in showing the uncorrelated part of the aperture field. Units of L_x are in mm.

are given in compact form by:

$$\mu \nabla^2 v = \nabla P, \tag{2.1}$$

$$\nabla \cdot v = 0, \tag{2.2}$$

with the fluid's dynamic viscosity μ, pressure P and velocity vector $v = (v_x, v_y, v_z)$, ∇, $\nabla\cdot$, and ∇^2 denote the gradient, divergence, and Laplace operator for 3D Cartesian coordinates, respectively.

These equations can be solved analytically for an idealized fracture, consisting of two parallel plates, vertically separated by a constant aperture a. Volumetric integration of the horizontally extended Poiseuille-flow solution yields the well known cubic law:

$$Q = -\frac{w a^3 \Delta P}{12\mu}, \tag{2.3}$$

with total volumetric flow rate Q, fracture width w and pressure gradient along the fracture ΔP (see Zimmerman and Bodvarsson (1996) for a more detailed derivation). Combining equation 2.3 with Darcy's law for flow through porous media:

$$Q = -\frac{kA\Delta P}{\mu}, \tag{2.4}$$

with cross-sectional area A, leaves the intrinsic permeability k of an idealized fracture proportional to its aperture by $k \propto a^2/12$. For a rough walled fracture, the aperture is no longer constant but rather varying across the fracture plane. The mean planes of an upper and lower

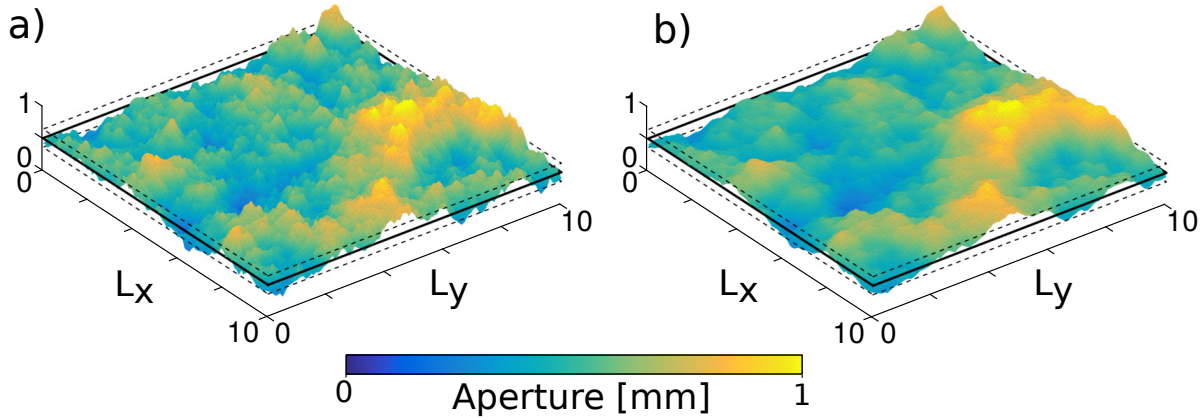

FIGURE 2.2: Two aperture fields constructed from synthetic fractures. Both aperture fields are based on the same sets of random numbers with varying Hurst exponents H, which is a) 0.4 and b) 0.8. The two statistical parameters $\bar{a}$ and σ_a are indicated by black solid and dashed lines, respectively. Axis units are in mm, while the vertical axis (indicating aperture) is exaggerated by a factor of two for clarity. Note that $\bar{a}$ and σ_a are identical for a) and b). Increasing height fluctuations at smaller scales, caused by a lower Hurst exponent results in a larger effective surface area S for fracture a) compared to b).

rough surface $s_u(x,y)$ and $s_l(x,y)$ are separated by a constant distance d to form $a(x,y)$ according to:

$$a(x,y) = \left[s_u(x,y) + \frac{d}{2}\right] - \left[s_l(x,y) - \frac{d}{2}\right]. \tag{2.5}$$

Depending on d, the surfaces may overlap at certain points and form contact areas, such that $a_0(x,y)$ is zero at these locations:

$$a_0(x,y) = \begin{cases} a & \text{if } a(x,y) > 0 \\ 0 & \text{if } a(x,y) \leq 0. \end{cases} \tag{2.6}$$

Assuming, that s_u and s_l are self-affine, the standard deviation σ of the aperture field computed at system size l scales as (Brown, 1995; Schmittbuhl et al., 1995):

$$\sigma = \begin{cases} \beta l^H & \text{if } 0 \leq l \leq l_c \\ \beta l_c^H & \text{if } l_c \leq l \leq L, \end{cases} \tag{2.7}$$

with the maximal system size L and the correlation length l_c. Below l_c, the fracture is uncorrelated, and it is well correlated above it (see Fig. 2.1 for a visual explanation). The prefactor β delivers information about the overall amplitude of the surface roughness. H typically denotes the scaling or Hurst exponent with $0 < H \leq 1$, whereas $H = 1$ corresponds to self-similar and $H < 1$ to self-affine scaling (e.g., Mandelbrot, 1982). Physically, self-affinity is expressed by higher height fluctuations at smaller scales, leaving H as a measure for the ratio of large scale versus small scale roughness intensity.

Here, we use the following two non-dimensional quantities to quantify the geometry of a

rough fracture: (i) the relative closure R and (ii) the effective surface area S. We compute the relative closure by dividing the standard deviation of the aperture field at the maximal system size σ_a by the average aperture field $\bar{a}$:

$$R = \frac{\sigma_a}{\bar{a}}, \tag{2.8}$$

with $\bar{a}$ defined by:

$$\bar{a} = \frac{1}{L_x L_y} \int_{x=0}^{L_x} \int_{y=0}^{L_y} a_0(x,y) dx dy. \tag{2.9}$$

This quantity or its reciprocal is commonly used to infer the amount of contact between the opposing fracture walls (Patir and Cheng, 1978; Brown, 1987; Zimmerman and Bodvarsson, 1996; Méheust and Schmittbuhl, 2000). Theoretically, it falls in the range $0 < R \leq \infty$, whereas $R = 0$ shows perfect accordance with parallel plates and the surfaces are in contact if $R \geq (3\sqrt{2})^{-1}$ (see Brown, 1987).

Furthermore, one requires a parameter that quantifies the effective surface roughness of a fracture since fractures with different H can have equal R values (see Fig. 2.2 for a visualization of the non-uniqueness of R). We, therefore, introduce a new quantity, the "effective surface area S". This parameter uniquely combines varying amplitudes and scaling exponents, because an increase in fracture surface area is the direct consequence of increasing roughness. For that, we calculate the ratio of the surface area of the fracture sa_f to twice the area of its projection on the fracture plane (i.e., two times the base area perpendicular to the flow direction) sa_c and normalize it with the fractional amount of the aperture field that has opened, i.e.:

$$S = \left(\frac{sa_f}{sa_c}\right)\left(\frac{1}{1-c}\right), \tag{2.10}$$

with c being the contact fraction of the aperture field (i.e. where $a_0(x,y) = 0$), which leaves $1 \leq S \leq \infty$, with $S = 1$, showing perfect accordance with parallel plates. To finally quantify the influence of fracture roughness on its intrinsic permeability, the proportionality resulting from the cubic law needs to be corrected (e.g., Witherspoon et al., 1980) by applying a correction factor according to:

$$k \propto \chi \frac{a^2}{12}. \tag{2.11}$$

The approximation of χ in terms of quantified fracture roughness, i.e., $\chi(R,S)$, is the main subject of this study.

2.3.2 Numerical permeability estimation

To simulate the laminar flow of an incompressible, iso-thermal, and iso-viscous fluid, we use a 3D binary voxel model input. We solve the linearized momentum balance (eq. 2.1) and continuity (eq. 2.2) equation in 3D, using velocity and pressure as primary variables. The coupled system is implemented in the open-source software package LaMEM (Kaus et al., 2016). LaMEM is a 3D staggered grid finite-difference code, which is based upon PETSc (Balay et al., 2018). The software is massively parallel and thus optimized for the use of high-performance computing (HPC) clusters to enable the computation of high-resolution models in a reasonable

amount of time. Here, the matrix is considered impermeable and constrained to no-flow conditions by forcing all three velocity components to be zero at the matrix-void-boundary. Besides, the staggered grid discretization scheme is rescaled at the fluid-matrix interface to provide higher accuracy (Eichheimer et al., 2019). Different pressures are applied on two opposing boundaries ($\Delta P = 0.01$ Pa for all models), while the remaining boundaries are set to no-slip. This fixes the principal direction of fluid movement (here it is in y-direction, e.g. Fig. 2.3). After ensuring that the numerically converged solution is obtained (see appendix A in Eichheimer et al., 2019), the velocity component parallel to the principal flow direction is integrated over the volume to compute the volume average velocity $\bar{v}$ according to:

$$\bar{v} = \frac{1}{V} \int_V |v_y| \, dy, \tag{2.12}$$

with the domain volume V. To finally obtain the intrinsic permeability k_i, $\bar{v}$ is substituted into Darcy's law for flow through porous media, similar to the approach of Osorno et al. (2015):

$$k_i = \frac{\mu \bar{v}}{\Delta P}, \tag{2.13}$$

with the fluid's dynamic viscosity μ.

2.3.3 Synthetic fracture data set

As in-situ data of fractures are rarely accessible and limited to the size of drill cores, numerical studies commonly rely on a stochastic generation approach for synthetic fractures (e.g., Brown, 1995; Candela et al., 2009). Here, we numerically generate isotropic self-affine surfaces

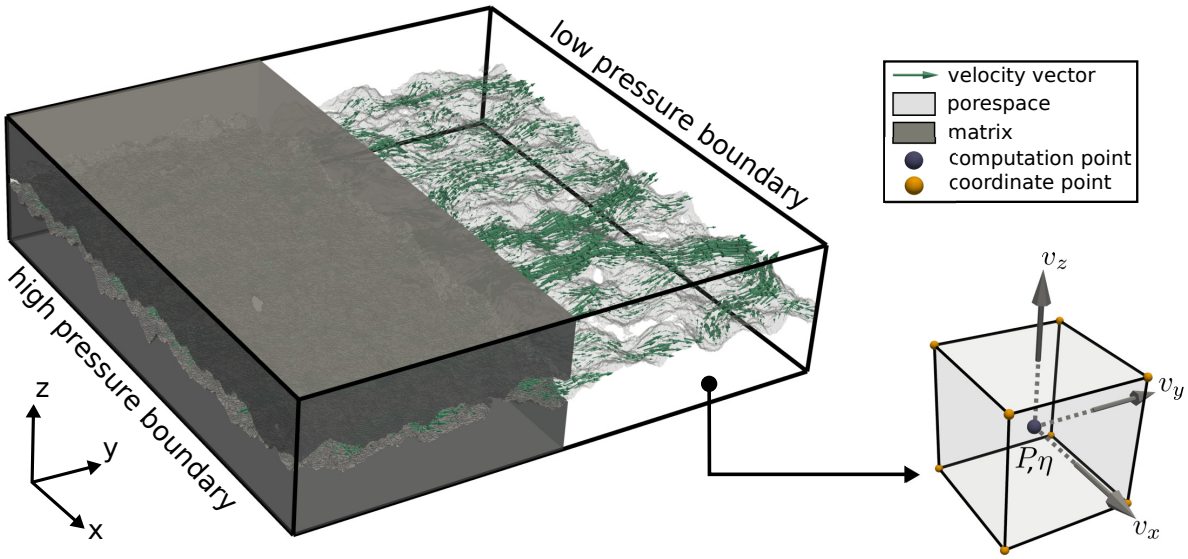

FIGURE 2.3: Model setup employed in the numerical simulations. The two boundaries where the pressure gradient is applied are indicated. The green velocity vectors are used for the computation of $\bar{v}$ and scaled according to their magnitude. The sub-figure illustrates the staggered-grid discretization-scheme of a single voxel.

with a MATLAB script (Kanafi, 2016), which makes use of random theory and fractal modeling techniques (Persson et al., 2004). It uses the standard deviation of surface heights σ_s, the Hurst exponent H, the cutoff length l_c, and the system size L in x and y direction as input parameters to obtain $s_u(x,y)$ and $s_l(x,y)$, which are built from two independent Gaussian random number fields. The code is slightly modified, such that the seeds for the random number generator are prescribed to produce reproducible results. The mean planes ($x-y$ coordinate plane in both cases) of s_u and s_l are separated by varying values of d according to equation 2.5 to simulate different closure stages of the fracture. Since ignoring mechanical deformation is a common practice (Brown, 1987; Méheust and Schmittbuhl, 2000; Méheust and Schmittbuhl, 2003; Mourzenko et al., 2018), we also assume that both surfaces are in contact at the locations where they overlap. Finally, the data is transferred into a 3D voxel space of $512 \times 512 \times 128$ voxels with a fixed physical voxel size of 0.1 mm, resulting in a model domain of $51.2 \times 51.2 \times 12.8$ mm. The relative closure and the effective surface area are computed according to equations 2.8 and 2.10, respectively. It is important to note that both quantities are computed only within the effective pore space of the fracture parallel to the direction of the applied pressure gradient because only this contributes to the overall flow. For some configurations, it might be possible to have small amounts of trapped pore space within the fracture that must be excluded before further numerical treatment. We separate the data sets generated in this study into two groups, each which specific sets of input-parameter combinations and a certain number of realizations (input values are listed in table 2.1). The first group is used to analyze the percolation probabilities and determining the parameter boundaries for geometries of group 2, which are later used for numerical flow simulations. To check, whether each fracture configuration in group 1 is able to transmit fluids, i.e., if it is percolating or not, we apply a recursive flood-filling MATLAB routine (e.g., Torbert, 2016). Then, the percolation probability p represents the mean value of n fracture realizations built from one specific input parameter combination, such that:

$$p = \frac{1}{n}\sum_{i=1}^{n} p_i \,, \text{ with } p_i = \begin{cases} 1 & \text{if percolating} \\ 0 & \text{if non-percolating.} \end{cases} \tag{2.14}$$

TABLE 2.1: Minimal and maximal input values for parameters d, σ_s, H and l_c/L. n denotes the total number of increments, including minimum and maximum. Subscripts $g1$ and $g2$ indicate data for group 1 or 2, respectively. Thus, multiplying the n values of each parameter gives the total number of parameter combinations (6000 for group 1, 320 for group 2). The number of realizations for a set (i.e. the number of different random number seeds used to generate the surfaces with one peculiar parameter combination) are given in the footnotes, resulting in a total of 600000 and 6400 fracture configurations for group 1 and 2, respectively.

Parameter	Dimension	$\min_{g1}$	$\max_{g1}$	n_{g1}	$\min_{g2}$	$\max_{g2}$	n_{g2}
d	mm	0.01	1	20	0.2	5	4
σ_s	mm	0.1	0.6	6	0.2	0.5	4
H	-	0.1	1.0	10	0.1	1.0	4
l_c/L	-	1/16	1	5	1/16	1	5

$r_{g1} = 100$, $r_{g2} = 20$

Figure 2.4 shows the percolation probability as a function of relative closure R, as there was no notable variation with respect to their effective surface areas. Generally, the percolation probability starts reducing from 1 at $R \approx 1$ and converges to zero at $R \approx 5$. Higher l_c/L ratios show earlier convergences to their percolation limit, as visible from the two fitted lines for l_c/L 1 and 1/16. From the inset plot, it is evident that the contact fraction of all models only depends on the relative closure R, first contact between both walls occurs at $R \geq 3\sqrt{2}\sigma_a$, which is in good accordance with Brown (1987). Following this, we have chosen to limit the fracture geometries for the fluid flow simulations to configurations with $R \leq 1$ to (i) exclude non-percolation systems and (ii) limit the effect of the above-mentioned "melting" hypothesis, which intensifies with increasing R. To ensure applicability to nature, the input values for group 2 (see table 2.1) are chosen, such that the resulting fracture geometries are classified from "closed" to "open" joints according to Bieniawski (1989). The resulting parameter-ranges for fractures in group 2 can be found in table 2.2. For the numerical fluid flow simulations, we implemented the following workflow: First, we apply a flood-filling algorithm on the initial 3D model along x-direction. R and S are calculated on the resulting effective pore space, followed by a numerical permeability estimation, as explained above, in the same direction. Then, we rotate the initial model by 90° in the $x-y$ plane, and the procedure explained above is repeated. In this manner, two-directional permeability values for every fracture are obtained, resulting in a total sum of 12800 fluid-flow simulations.

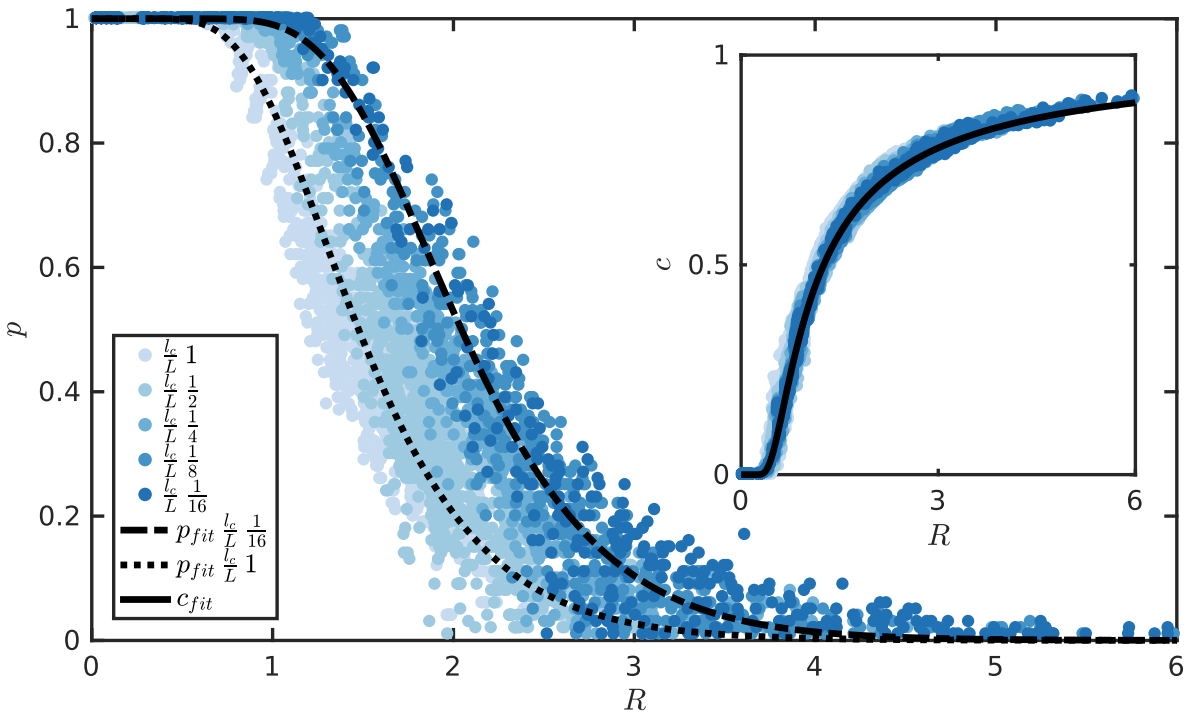

FIGURE 2.4: Percolation probability p (eq. 2.14) and the mean fractional amount of contact c as a function of relative closure R for all fracture realization sets of group 1 and 2. Different shades of blue indicate different l_c/L ratios as given in the legend, whereas black lines show best fits to the data.

TABLE 2.2: Resulting minimal and maximal values for mean aperture ($\bar{a}$), standard deviation of the aperture field (σ_a), contact fraction (c), relative fracture closure (R), effective surface area (S) and numerical fracture permeability (k_m) for the fracture geometries in group 2.

Parameter	$\bar{a}$	σ_a	c	R	S	k_m
Dimension	m	m	-	-	-	m^2
min	1.91×10^{-4}	1.16×10^{-4}	0	0.03	1.04	6.78×10^{-14}
max	4.96×10^{-3}	8.51×10^{-4}	0.44	0.99	2.49	7.94×10^{-7}

2.4 Results

2.4.1 Hydraulic efficiency

In the following section, we present the results of the numerical fluid flow experiments within the geometries of group 2. For this, we normalize the numerically computed permeabilities (k_m) by the permeability predicted by the cubic law (k_{cl}) with equivalent mean aperture $\bar{a}$ of the associated effective pore space:

$$\chi = \frac{k_m}{k_{cl}}. \tag{2.15}$$

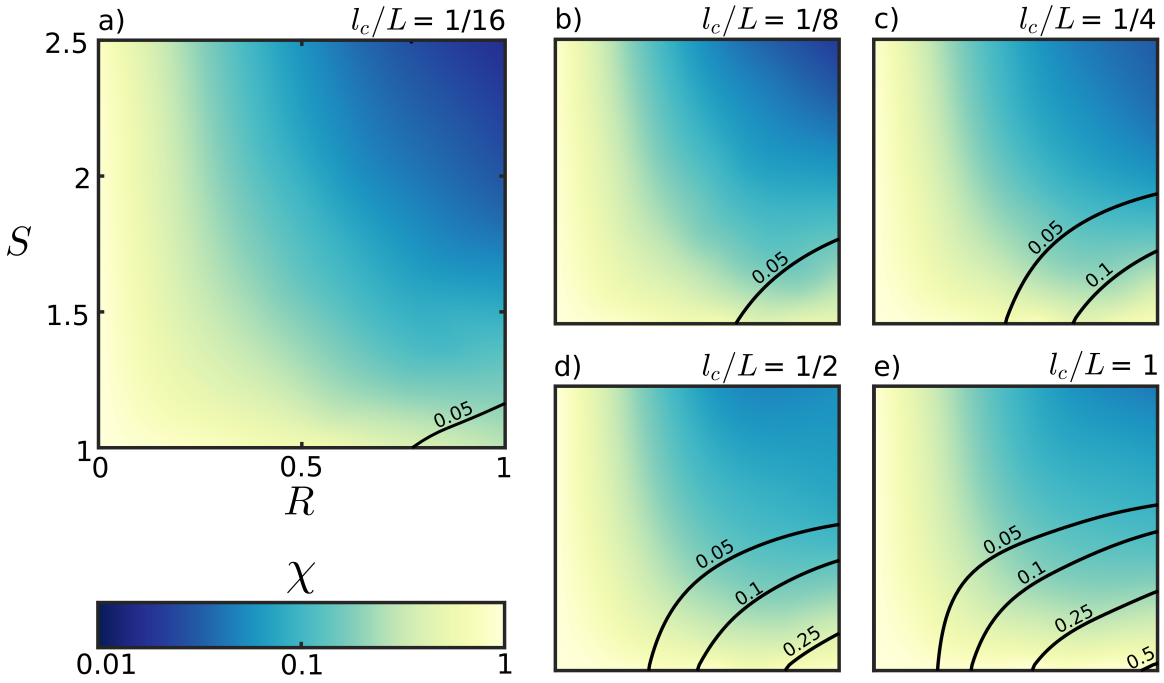

FIGURE 2.5: The distribution of the hydraulic efficiency χ for different l_c/L ratios as a function of R and S. Both axes limits in *a* correspond with *b-e*. Dark blue color indicates poor hydraulic efficiency, whereas lighter color shows increasing accordance with the cubic law. The black contour lines indicate the absolute residuals to the fitted surface (Compare with Fig. 2.6).

Consequently, one can use the hydraulic efficiency χ as the correction factor in eq. 2.11 to apply the cubic law to rough fractures. In that way, a fracture whose configuration is close to

the parallel plate geometry shows excellent hydraulic efficiency with χ close to one. In the R-S-space, the parallel plate fracture configuration exclusively corresponds to a single point with coordinates $(0, 1)$. Perfect hydraulic efficiencies ($\chi = 1$) were validated by flow simulations in parallel-plate fractures.

The key result of this study, a model that corrects the cubic law in terms of quantified fracture roughness, is proposed in Fig. 2.5. Due to the complexity of the results, we fitted a regularized surface with a MATLAB function called "gridfit" (DErrico, 2006) to approximate the solution in R-S space. The function can interpolate scattered data within a prescribed bounding box and a certain amount of smoothing, resulting in a clearer solution image compared to conventional interpolation techniques. Furthermore, to enable an adequate basis for the fitting, the data was cropped above $R = 1.0$ and $S = 2.5$ to provide sufficient data density in R-S-space, which reduces the total amount of simulations used for the fitting from 12800 to 10292.

The results display significant deviations from the cubic law approximation, even for fractures where both surfaces are not in contact (i.e., $R \leq 0.23$). We obtain the lowest χ values in regions of high R and S, with a general trend of increasing χ for larger l_c/L ratios.

The absolute residuals of the fitted surface from Fig. 2.5 to the simulated data are computed to investigate the hydraulic efficiency fluctuations for similar fracture configurations. As before, we fit a regularized surface through the scattered points from which we extract the displayed contour lines (Fig. 2.5). They indicate that the goodness of the fit reduces with increasing l_c/L ratios, especially in the lower right corner. Hence, the non-uniqueness of the data reduces for

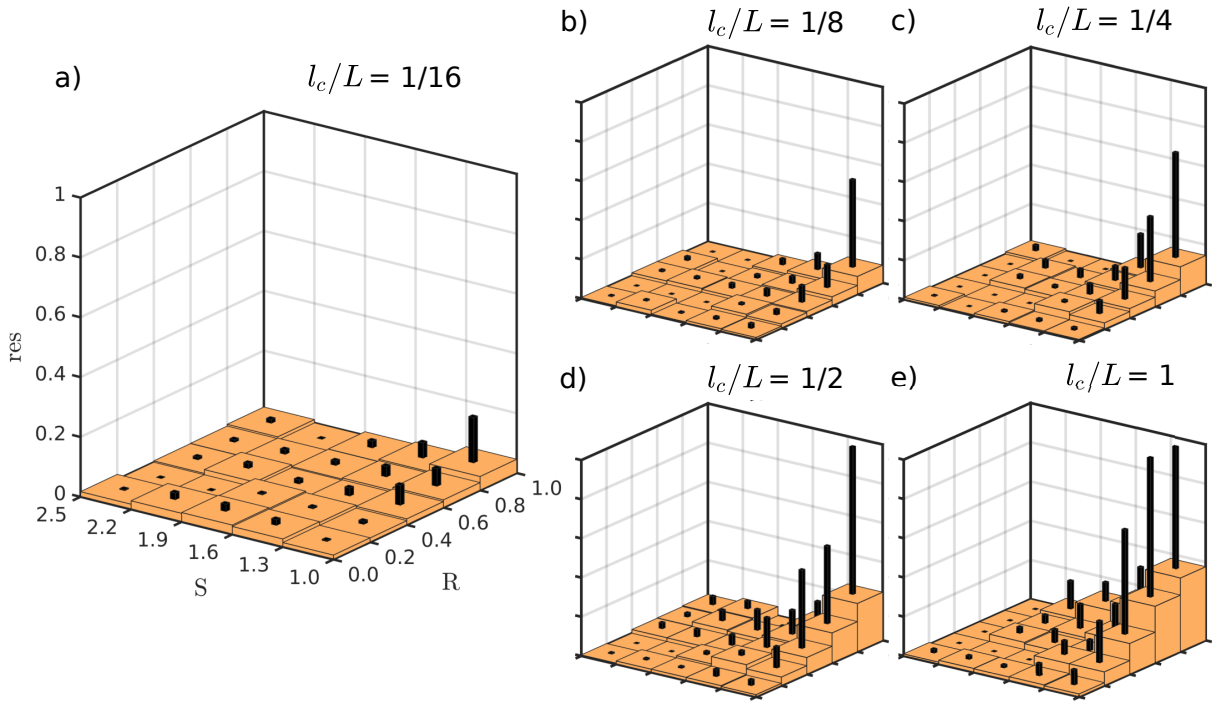

FIGURE 2.6: Absolute residual values of the fitted surfaces in Fig. 2.5 for different l_c/L ratios as a function of R and S, binned into equally sized boxes. All axes limits in *a* correspond to the ones in *b-e*. Orange boxes indicate the mean absolute residual value of the specific bin, whereas the smaller black boxes on top give the maximum absolute residual.

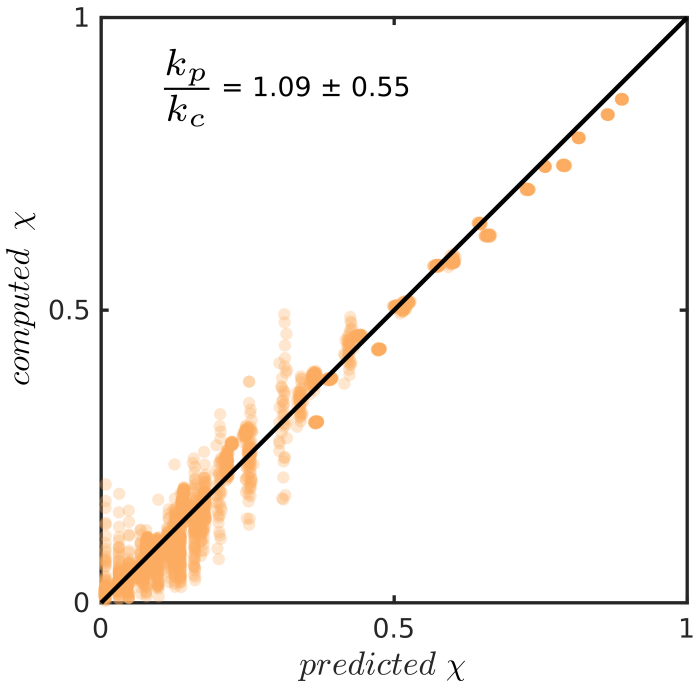

FIGURE 2.7: Parity plot of predicted versus computed hydraulic efficiency χ for a total of 2554 fractures with an l_c/L ratio of 1/16. The black line indicates the location of perfect parity. Inlet data gives the mean and standard deviation of predicted (k_p) over computed (k_c) permeabilities that correspond to all data points in the plot.

lower l_c/L ratios, which can be even better seen in Fig. 2.6. A regional, maximum residual of about 0.2 for fractures with a l_c/L ratio of 1/16 enables a more or less unique parametrization refinement, which is not the case for higher l_c/L ratios. Our finding that low l_c/L ratios show lower reduced variability is consistent with the results of Méheust and Schmittbuhl (2003).

An easy integration of this parametrization refinement into a DFN framework requires a mathematical approximation of the fitted surface shown in Fig. 2.5 a), which was found by the following equation:

$$\chi = 1 - (0.4809 \tanh(0.5139S) + 0.5408) \tanh\left(\frac{R}{39.28 \tanh(-2.451S) + 39.47}\right) \tag{2.16}$$

To predict single fracture permeability, it is only necessary to know the mean and standard deviation of the aperture field ($\bar{a}$ and σ_a), the fractional amount of surface contact (c) and the surface area protruding into the void space (sa_f). From these values, R and S are computed to infer the hydraulic efficiency χ with eq. 2.16, which is then multiplied by the permeability predicted by the cubic law with aperture $\bar{a}$ (see eq. 2.11). Fig. 2.7 demonstrates the accuracy of eq. 2.16 to predict hydraulic efficiencies and accompanying permeabilities for fractures with l_c/L ratios of 1/16. To quantify the hydraulic efficiency fluctuations (σ_χ) with respect to its

TABLE 2.3: Coefficients a, b, c and d for equation 2.17, determined by least-square fitting for fractures with varying l_c/L ratios.

l_c/L	a	b	c	d
1/16	0.0428	0.1652	-0.8226	0.8822
1/8	0.6517	-0.3135	-0.6751	0.6625
1/4	0.9509	-0.7343	-0.7852	0.7672
1/2	1.0491	-0.9632	-1.2065	1.1752
1	1.3267	-1.3174	-1.6613	1.6178

correlation length, we provide a model of the form:

$$\sigma_\chi = (a \times e^R + b)(c \times tanh(S) + d) \tag{2.17}$$

with corresponding parameter values given by table 2.3.

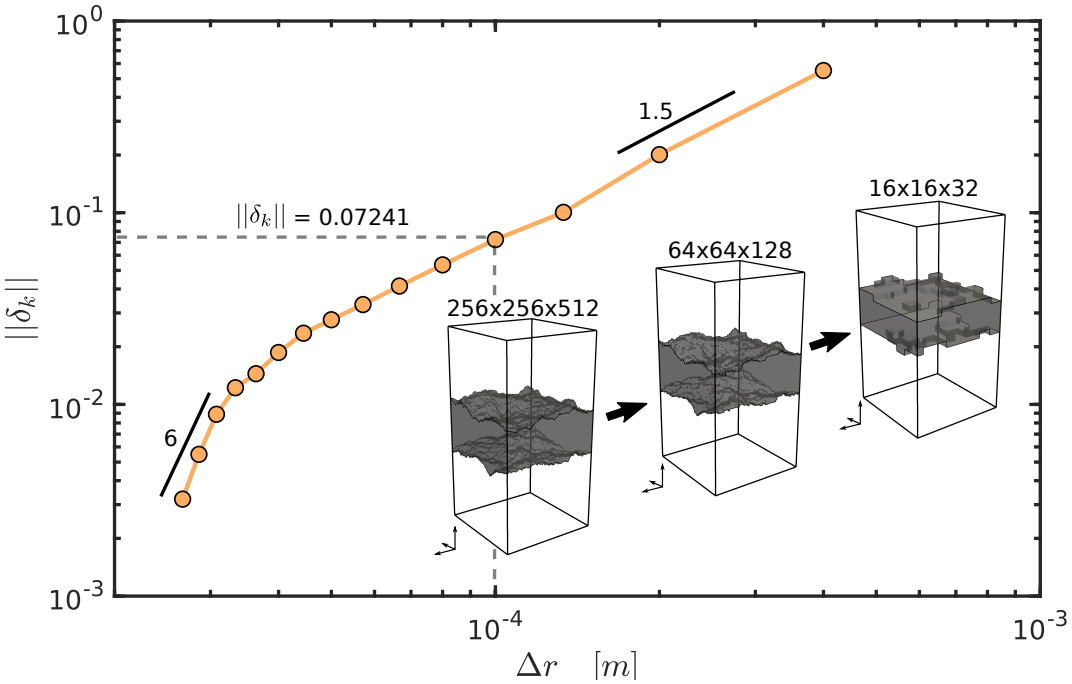

FIGURE 2.8: Error norm computed by eq. 2.18 as a function numerical voxel size Δr. The orange line depicts the mean error of 128 different fracture subsets discretized with decreasing resolutions. The figure inlay sketches the downsampling procedure is sketched: The maximal resolution is consecutively decreased by 16 in horizontal and 32 voxels in the vertical direction (displayed is the maximal, intermediate and minimal reduction stage). Dashed gray lines indicate the voxel size and associated error norm of the numerical simulations used to provide the refined single fracture permeability parametrization. Black lines highlight the convergence rate by showing local slopes as indicated by the attached values.

2.4.2 Accuracy of the numerical solution

Numerical inaccuracies in solving the Stokes flow equations related to the resolution of the numerical models potentially have an important impact on the results shown here. For numerical permeability estimations of single fractures, the resolution perpendicular to the aperture field is the most crucial part. As the most relevant roughness features are expressed within the uncorrelated region of a fracture (i.e., where $l_c = L$), it is necessary to examine the numerical error introduced due to resolution loss therein. For that, eight fractures with the size of 4096x4096x512 voxels and a l_c/L ratio of 1/16 are generated in the same manner as explained in section 2.3. For each fracture, 16 subsets are drawn that focus uncorrelated regions of the fracture, resulting in subsets of $256 \times 256 \times 512$ voxels. By this, the fracture part oriented perpendicular to the applied pressure gradient is over-resolved by a factor of two. The resolution of these initial models is then consecutively reduced down to $16 \times 16 \times 32$ voxels (see inlay of Fig. 2.8 for a workflow sketch) while maintaining a constant dimensional aspect ratio. The resulting permeability at every stage (k_r) is then compared to the result at maximal resolution (k_{max}), assuming that this represents the most accurate solution. Finally, we compute the error norm according to:

$$||\delta_k|| = \left| \frac{k_r - k_{max}}{k_{max}} \right| \tag{2.18}$$

Ideally, the error norm should get negligible at the highest resolution. Fig. 2.8 shows the mean error norm of a total of 128 uncorrelated fracture subsets as a function of voxel size Δr. A mean error of about 0.01 % at maximal resolution indicates optimal convergence to the most accurate solution, which validates the numerical procedure. The voxel size of the numerical models used in this study (0.1 mm) results in an acceptable mean error of 7.2 %, as indicated in Fig. 2.8.

2.5 Discussion

Many studies report that the cubic law deviates with increasing relative fracture closure (Patir and Cheng, 1978; Brown, 1987; Zimmerman and Bodvarsson, 1996), which is usually attributed to the flow channeling around the contact spots within the fracture, introducing an in-plane tortuosity that reduces the permeability. We quantified the deviations from the cubic law due to vertical roughness features (i.e., amplitudes or Hurst exponents, see Fig. 2.5). The results suggest that with increasing fracture surface area protruding into the fluid phase, more drag force accumulates at the fluid-matrix interface, which resists the flow and leads to reduced permeabilities. It is not possible to capture these vertical variations in the flow field with previous 2D modeling approaches (e.g., Patir and Cheng, 1978; Brown, 1987; Renshaw, 1995; Zimmerman and Bodvarsson, 1996), which then results in a biased prediction and the need for more parameters to ensure an adequate quantification. Fig. 2.9 highlights this issue by computing the norm $||\delta_k||$ between measured and predicted permeabilities for all fractures in this study. With a mean error of 26.7 % eq. 2.16 delivers a better prediction compared to the mentioned studies.

As already shown by Méheust and Schmittbuhl (2003), the uncertainty for predicting fracture flow is a function of its l_c/L ratio. Considering flow predictions for uncorrelated fractures (i.e. $l_c/L \geq 1$) is problematic. Blocked pathways connected to the early appearance of the

percolation limit (see Fig. 2.4) or flow enhancing configurations ($\chi > 1$) as also observed by Méheust and Schmittbuhl (2000) are producing substantial variations in their hydraulic efficiencies. With decreasing l_c/L ratios, the impact of vertical flow tortuosity on its permeability increases relative to the impact of in-plane tortuosity, as both start to act at comparable scales and generally, the fractures exhibit larger portions of flow inhibiting regions compared to flow enhancing ones (see Méheust and Schmittbuhl, 2000). On the contrary, the fluctuations in the average flow behavior decrease significantly with decreasing l_c/L ratios. This suggests that predicting hydraulic properties is constrained to fractures, whose sizes are significantly greater than their correlation lengths. Theoretically, the correlation length is mainly controlled by shear offset and respective gouge generation (Brown, 1995; Méheust and Schmittbuhl, 2000). With the assumption of a perfectly matched fracture ($l_c = 0$) at its nucleation stage, it is tempting to propose that most natural fractures actually meet the conditions of low l_c/L ratios and subsequently enable the prediction of their hydraulic properties. However, so far, little is known about naturally existing correlation lengths in fractures, as the imaging of in-situ fractures is limited to the size of drill cores. Only Brown (1995) report measurements of l_c by analyzing the power spectral densities of composite topographies for two matched profiles on opposing joint surfaces, shedding some light into their natural ranges. From a mechanical perspective, correlation lengths that are equal to the size of the fracture seem rather unrealistic, considering that the shear displacement d_s of fractures scales with their length L_f according to $d_s = \alpha {L_f}^{0.5}$ (Schultz et al., 2008). Using α values between 0.01 and 0.001, which is about the range for

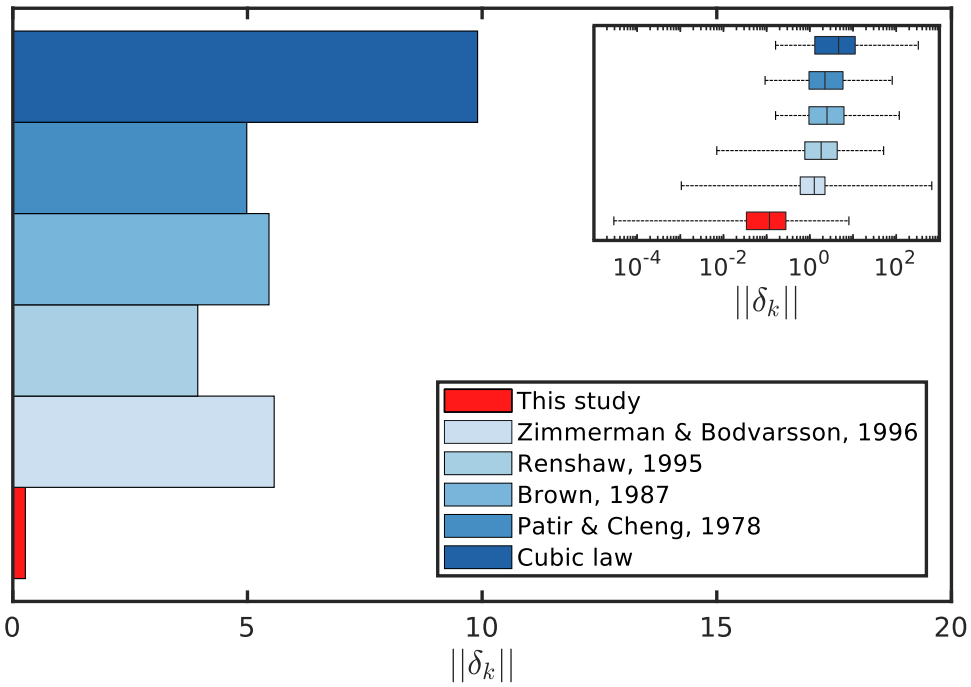

FIGURE 2.9: Mean error norm δ_k (see eq. 2.18) of all fractures considered in this study for different prediction models. The mean error norm recorded for this study is 0.267. Inlet plot shows box and whisker plots incorporating all outliers, i.e. representing minimum and maximum recorded values.

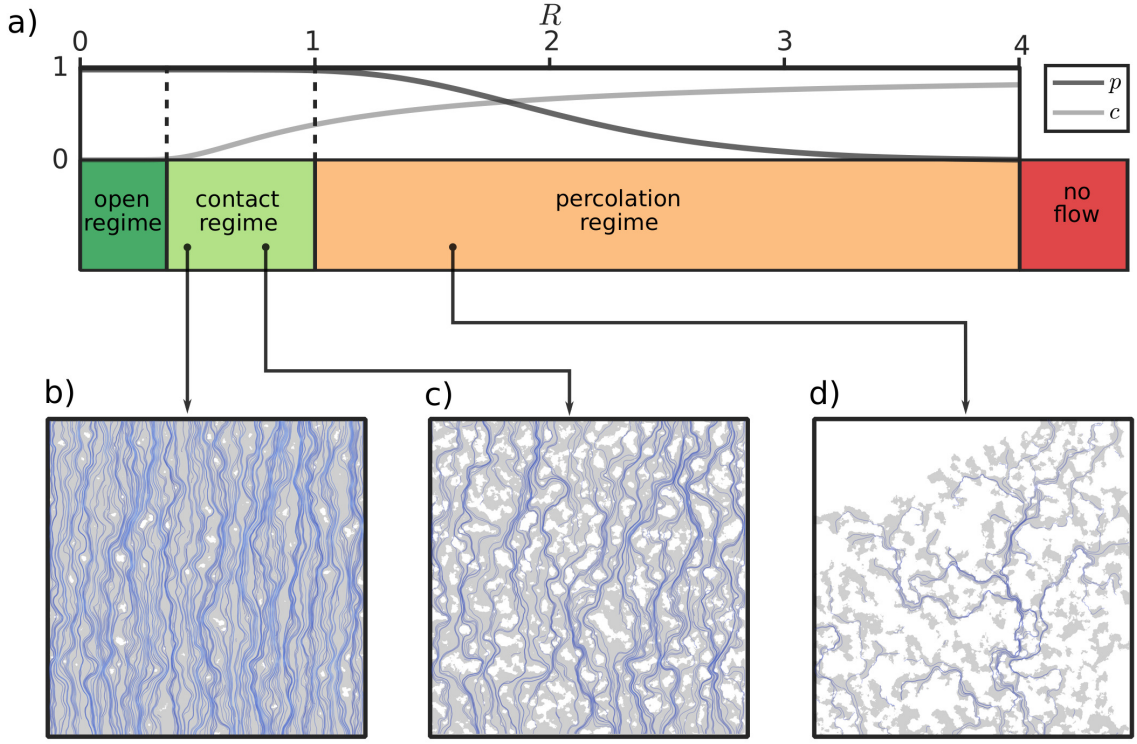

FIGURE 2.10: A sketch of the three different closure regimes, indicated as a function of R with corresponding p and c. The lower part of the figure shows three examples of fluid flow simulations from the indicated regimes. Grey shaded area is fracture void space, whereas white regions indicate contact between both surfaces. Blue lines depict chosen streamlines, approximated from the resulting Stokes velocity vectors.

Moros' joints in Schultz et al. (2008), results in a maximal l_c/L_f ratio of 0.01. All of that illustrates that further research on fractures correlation lengths is required because the presence of it is omnipresent in most relevant studies (Brown, 1995; Mourzenko et al., 1996; Méheust and Schmittbuhl, 2003; Dreuzy et al., 2012; Pyrak-Nolte and Nolte, 2016; Mourzenko et al., 2018).

2.6 Conclusion

To understand the effects of fracture surface roughness on fluid flow, we performed numerical simulations of high-resolution 3D Stokes-flow within fractures for a large synthetic data set By consolidating varying asperity amplitudes and roughness scaling within a new quantity, that accounts for the effective increase of surface roughness compared to its parallel plate equivalent, we were able to provide a new way to characterize fracture roughness. By combining the effective surface area with the relative fracture closure, we established a two-parameter characterization scheme that reads similar to a phase diagram. It is utilized to quantify the hydraulic efficiency of single fractures empirically, i.e., the correction factor applied to the current state-of-the-art fracture permeability parametrization (cubic law). Our findings confirm the results of Méheust and Schmittbuhl (2003) and highlight that predicting fracture flow is constrained

to scales of at least 16 times larger than the correlation length. The hydraulic efficiency as a function of effective surface area and fracture closure is given by eq. 2.16, its variability with respect to the correlation length is given by eq. 2.17 and table 2.3, whereas an overall numerical error of 7.2 % has to be considered. Ultimately, we used the percolation probability and contact fractions to classify three different closure regimes that differ in terms of their hydraulic interpretation:

(i) The open regime defines fractures whose surface walls are not in contact with each other (e.g., unconfined dilatant or karstified fractures). In this regime, we generally observe a good agreement of the cubic law with hydraulic efficiency between $70 - 100\%$ and only extreme roughness configurations (e.g., needle-shaped mineral coatings) result in larger deviations.

(ii) The contact regime is characterized by fractures exhibiting a rapidly decreasing hydraulic efficiency from $70 - 10\%$ up to 1 % in extreme cases, which is caused by strong three-dimensional channeling due to surface roughness and increasing fracture closure. Likely, this regime is most suitable for subsurface conditions, as a certain amount of contact between both fracture surfaces is required to withstand confining pressures.

(iii) The percolation regime incorporates fracture configurations that do not percolate at all due to blocked fluid pathways. Here, we do not incorporate fluid flow data, but it is plausible that the hydraulic efficiency is very poor with a maximum of 25%, which will quickly converge to 0% due to the effect of decreasing percolation probability with further closure. We observe the no-flow boundary at $R \approx 6$.

Our results generally help to understand the hydraulic response induced by different types of fracture geometries and refine the parametrization of single fracture permeability given by the cubic law. Moreover, the developed quantification scheme allows monitoring and parameterizing the hydraulic and geometric evolution of fractures during aperture field-shaping processes. This parametrization can easily be incorporated in a DFN modeling framework to investigate the hydraulic responses at reservoir scales, assuming that the minimal correlation length is no longer than $1/16$ of the reservoir size. If DFN's of scales close to the correlation length are considered, fluctuations in the average flow behavior are expected. This can modify network scale flow connectivity and thus requires additional concepts to compute permeabilities (e.g., Dreuzy et al., 2012).

Chapter 3

The correlation lengths and permeabilities of natural rock discontinuities [1]

3.1 Introduction

Naturally occurring reservoirs with fracture-dominant flow behavior play a key role in hydrocarbon production, geothermal energy systems, and CO_2-sequestration (March et al., 2018; Ghosh et al., 2020; Patterson et al., 2020). As their host rock porosity is relatively low (e. g., crystalline basement or tight carbonate rocks), the flow through open discontinuities primarily controls bulk hydraulic properties. Typically referred to as fractures, they can have various lengths, apertures, and orientations in nature (Gudmundsson, 2011). Thus, prescribing their permeabilities is a crucial requirement to model fluid flow at the network- or reservoir scale (e. g., Cacas et al., 1990; Bogdanov et al., 2003; Darcel et al., 2003). This is typically done with a parallel plate analogous, for which an analytical solution to the Stokes equations exists (Lomize, 1951; Snow, 1969; Witherspoon et al., 1980). In combination with Darcy's law for flow through porous media, one can relate the permeability of a fracture by the separation of the two parallel plates, i.e., its aperture. Surface roughness and contacting asperities cause deviations from the idealized model, and their impacts on fracture permeability have been quantified from numerical flow simulations by numerous studies (e. g., Patir and Cheng, 1978; Brown, 1987; Renshaw, 1995; Zimmerman and Bodvarsson, 1996; Mourzenko et al., 1995; Brush and Thomson, 2003; Jin et al., 2017; Foroughi et al., 2018; Mourzenko et al., 2018). Not seldom, these functional approximations are non-unique, arising from the fact that aperture field of fractures show long-range correlations (Brown and Scholz, 1985; Glover et al., 1998b). Above certain length scales, the two fracture surfaces tend to be well-matched, while below these scales, the aperture follows self-affine models (Brown, 1995). There, large fluctuations in the average flow behavior are expected, which causes non-uniqueness of predictive functions. Considering fractures at scales larger than their apertures correlation length significantly reduces these fluctuations (Méheust and Schmittbuhl, 2003) which allows predicting average flow behaviors for fracture populations with similar geometries (e. g., Kottwitz et al., 2020).

[1] This chapter is currently in preparation for publication (Kottwitz, M. O., Klaver, J., Schmatz, J., Reinhardt, M., Enzmann, F., Popov, A. A., and Kaus, B. J. P.)

More specifically, the ratio between the correlation length and observation scale determines whether a modified parallel plate model adequately represents the fracture's hydraulic properties. Dreuzy et al. (2012) were the first to analyze the coupled effects of fracture scale heterogeneity and network topology on the permeability of fracture networks from numerical simulations of fluid flow. By setting a constant correlation length for all fractures and varying the fracture-size and -density distributions, they could demonstrate a strong effect of fracture scale heterogeneity on network scale flow and subsequently on the network's permeability that a modified parallel plate assumption cannot compensate. Notably, this effect is only severe if the correlation length is close to the overall system size and that it is weak if the system size is much larger than the correlation length. For large-scale fracture networks, it is valid to model the permeabilities of fractures with a modified parallel plate model as shown by Makedonska et al., 2016. They studied the effects of aperture variability up to a certain correlation length on flow and transport in kilometer-scale fracture network models. While prescribing the correlation length as fractions of the size of the fracture, they demonstrated that for low in-fracture variability (small correlation length fractions and low aperture variance), no significant effect on flow and transport behavior occurs. Only for sufficiently large in-fracture variabilities, effects on the network-scale transport behavior are noticeable. It highlights that an analysis of the correlation length in naturally occurring fractures is required to determine the scale at which a modified parallel plate assumption is valid for use in network flow models. Unfortunately, no general model exists that predicts the correlation length of fractures, as measurements on natural fractures are seldom reported. Brown (1995) provided a technique to estimate minimal and maximal correlation lengths from profilometer measurements of separated fracture surfaces and reported metrics for several discontinuities. This technique was adopted by Glover et al. (1998a), extended by Ogilvie et al. (2006) and applied by Zambrano et al. (2019) to present further estimates of correlation lengths, all based on measurements of synthetically mated fracture surfaces for aperture computations. However, analyzing correlation lengths in fractures has not benefited from recent progress in the field of digital rock physics (DRP, e. g., Andrä et al., 2013b; Schepp et al., 2020), which allows for non-destructive imaging of fractures in 3D (e. g., Tokan-Lawal et al., 2017) by using X-ray computed tomography (CT) (Andrä et al., 2013a; Cnudde and Boone, 2013). As this better reflects in-situ conditions and avoids artificial mating of fracture surfaces, analyzing CT-scanned fractures presents a valuable option to gain further knowledge on correlation lengths in naturally occurring fractures. For this study, we compile a data-set of 18 CT-scanned fractures and pre-process them to perform correlation length analysis according to the method of Ogilvie et al. (2006) to derive a model that predicts the correlation length of fractures. This should help determine the scale at which the utilization of a modified parallel plate assumption in network flow models (e. g., Davy et al., 2013; Bonneau et al., 2016; Maillot et al., 2016; Alghalandis, 2017; Lavoine et al., 2019) is valid. Additionally, we utilize the data-set for numerical fluid flow simulations to obtain their permeabilities (e. g., Eichheimer et al., 2019; Eichheimer et al., 2020). By comparing those to several fracture permeability prediction functions based on synthetic fracture data-sets (e. g., Patir and Cheng, 1978; Brown, 1987; Renshaw, 1995; Zimmerman and Bodvarsson, 1996; Kottwitz et al., 2020), we assess their accuracy and applicability to natural data.

3.2 Methods & Data

3.2.1 Obtaining surface and aperture data from binarized voxel models of discontinuities

In the following, we describe the pre-processing routine to obtain single fracture data that applies to any 3D binarized (two phases: void space and the solid matrix) voxel-data-set containing a single isolated fracture penetrating the whole scan volume. As the fracture might be scanned in arbitrary orientation, the first step is to align the fracture horizontally, i. e., in the x-y plane in a regular Cartesian coordinate system. For that, we generate a 3D point cloud of all voxel vertices that represent the pore space phase by fixing the left lowermost corner of the model to $(0|0|0)$ and using the voxel resolution as constant grid spacing. Principal component analysis (PCA) is applied to the 3D point cloud to obtain its covariance matrix, whereas the columns (eigenvectors) are in descending order with respect to their eigenvalues. Multiplying the 3D point cloud with the ordered covariance matrix rotates the point cloud such that the principal component with the smallest eigenvalue is aligned with the z-direction. After alignment, we transfer the point cloud back into voxel format by (1) generating a voxel grid with spatial extents of the new point cloud and the same spacing as before, (2) fixing the left lowermost corner of the model to $(0|0|0)$ (this may require shifting the points) and (3) dividing the point coordinates with the voxel spacing, rounding the results to obtain the grid-indices of the rotated voxel representing the fractures pore space. We construct the aperture field and both individual fracture surfaces by probing vertical columns of the aligned voxel model to produce 2D surfaces. The index of the first column voxel representing pore space multiplied with the grid spacing marks the height of the lower surface for the respective x- and y-location of the vertical column. The last entry denotes the height of the upper surface, and the total sum of pore space voxels per column indicates the local aperture. Contact between both surfaces is present if the probed vertical column contains no voxels representing the pore space. The aperture field at that location is zero, whereas the individual fracture surfaces are left empty. For spectral analysis routines, this requires interpolation of the empty patches, which according to (Candela et al., 2009) has a minor effect on the result. Another limitation of this technique are rarely observed but yet present local overhangs in voxel data-sets, which impede surface analysis algorithms as well (Brown and Scholz, 1985; Schmittbuhl et al., 1995; Shepard et al., 1995). If possible, regions of substantial overlap should be cropped out from the initial voxel model.

We follow the method described in Kottwitz et al., 2020 to compute the two necessary parameters from the constructed upper and lower surface as well as the aperture field to quantify the fractures deviation from the parallel plate equivalent, i. e., the relative closure R and the effective surface area S. The relative closure is computed by dividing the standard deviation of the aperture field σ_a by its average $\bar{a}$:

$$R = \frac{\sigma_a}{\bar{a}}, \tag{3.1}$$

with $\bar{a}$ defined by:

$$\bar{a} = \frac{1}{L_x L_y} \int_{x=0}^{L_x} \int_{y=0}^{L_y} a(x,y) dx dy, \tag{3.2}$$

whereas $a(x,y)$ is the 2D aperture field, L_x and L_y denote the spatial extends of the fracture plane. The effective surface area is computed according to:

$$S = \left(\frac{sa_f}{sa_c}\right)\left(\frac{1}{1-c}\right). \tag{3.3}$$

Here, sa_f denotes the summed area of the upper and lower fracture surfaces, and sa_c the surface area of the fractures parallel plate equivalent and the fractional amount of contact in the aperture field is given by c.

3.2.2 Estimating the correlation length in fracture aperture fields

A crucial requirement for the applicability of fracture permeability parametrization concepts (e. g., Patir and Cheng, 1978; Brown, 1987; Renshaw, 1995; Zimmerman and Bodvarsson, 1996; Kottwitz et al., 2020) is that the scale at which permeability is prescribed must be much larger than the correlation length of the fractures aperture field (Méheust and Schmittbuhl, 2003; Kottwitz et al., 2020).
Thus, correlation length analysis is obligatory to validate the use of parametrization concepts. A common technique to obtain it is by comparing scaling characteristics of the fractures individual surfaces to the ones of its aperture field. For fracture surfaces, the scaling is well described by self-affine fractal models (Brown and Scholz, 1985; Power et al., 1987; Schmittbuhl et al., 1995), i. e., the standard deviation of their surface heights σ_s along a profile drawn from the surface at observation scale l follows a power law according to:

$$\sigma_s(l) = \beta l^H, \tag{3.4}$$

whereas H denotes the Hurst exponent ($0 \leq H < 1$) characterising the self-affine property and β a proportionality constant that defines a characteristic scale (Mandelbrot, 1985; Candela et al., 2009). Equivalently, the power spectrum $P(k)$ of the same profile follows a power law of the form:

$$P(k) = Ck^{-\alpha}, \tag{3.5}$$

where k is the wavenumber that relates to the observation scale l according to $k = 2\pi/l$, α is the power law exponent that relates to the Hurst exponent by $\alpha = 1 - 2H$ (Brown, 1995; Candela et al., 2012) and C denotes the proportionality constant.

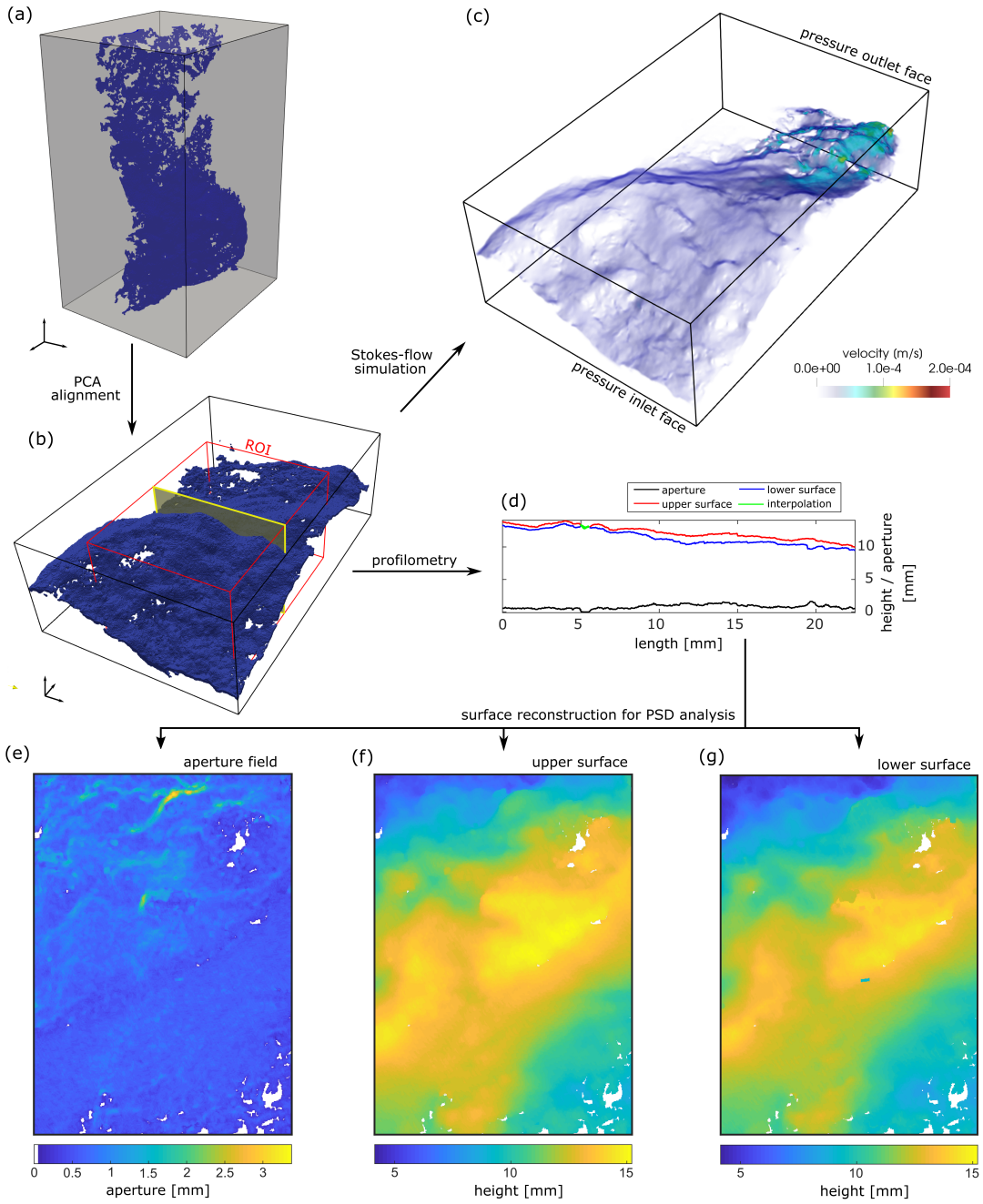

FIGURE 3.1: The pre-processing workflow of arbitrarily oriented fracture voxel models is delineated in this figure. Panel *a* shows the raw segmented voxel model of sample D_{03} obtained after thresholding and segmenting the CT data. Panel *b* displays the fracture void space of *a* after the PCA alignment process described in the text. The red rectangle denotes the region of interest (ROI) that avoids substantial regions of overlap in the voxel model, which would otherwise impede PSD analysis functionality. Panel *c* shows the steady-state velocity field resulting after the Stokes-flow simulations with LaMEM (conducted on the full aligned voxel model, not the ROI), which is then used to compute the directional permeability. Panel *d* displays an exemplary slice drawn from the ROI as indicated in *b* (yellow slice) to obtain 1D profiles of the upper and lower surface, from which the aperture is calculated. Repeating this procedure along the full length of the ROI allows to reconstruct the aperture field (shown in panel *e*) as well as upper (shown in panel *f*) and lower (shown in panel *g*) surfaces used for PSD analysis to estimate their correlation length.

However, the aperture field between two self-affine surfaces follows the same power law only to some extend. Above a certain length scale, both surfaces tend to be well-matched and can be interpreted as parallel planes. This correlation length l_c poses a limit to the self-affine scaling of aperture field standard deviation σ_a according to:

$$\sigma_a(l) = \begin{cases} \beta l^H & \text{if } 0 \leq l \leq l_c \\ \beta l_c^H & \text{if } l \geq l_c. \end{cases} \tag{3.6}$$

In practice, the scaling function levels off to constant values at scales above the correlation length (or below the wavenumber corresponding to it) (Brown, 1995). Here, we employ the spectral approach suggested by (Brown, 1995), extended by (Ogilvie et al., 2006) and applied by (Zambrano et al., 2019) to obtain estimates of aperture field correlation length. It involves computing the average power spectral densities (PSD) of multiple parallel 1D profiles drawn from a surface (panels *b* and *d* demonstrate this profilometry-procedure for slices drawn from a 3D voxel model, the same procedure is repetitively applied here on 2D surfaces) after removing the mean and linear trend from the profiles an applying a 10 % cosine taper to obtain respective scaling functions. In natural data, the transition from self-affine scaling to perfect correlation does not occur as abruptly as demonstrated in (Brown, 1995), but rather smoothly within a range of length scales. Thus, the method of (Ogilvie et al., 2006) suggests computing the mismatch ratio rm_{PSD} of the PSD of the aperture field (PSD_a) and the sum of the PSD's of the lower (PSD_l) and upper (PSD_u) surface according to:

$$rm_{PSD} = \frac{PSD_a}{PSD_l + PSD_u}. \tag{3.7}$$

While plotting the mismatch ratio as a function of scale, one can determine the minimal correlation length when the curve starts to decrease from unity and a maximal correlation length if the ratio converges to 0. The latter is often difficult to determine due to the scale limitations of imaging techniques. Thus the minimal correlation length is considered the reliable approximation of the correlation length (e. g., Zambrano et al., 2019).

3.2.3 Fluid flow modelling

Direct flow modelling of a single phase fluid in a digital representation of the rocks pore space is based on the Navier-Stokes equations (e. g., Bear, 1972). For most subsurface flow conditions, it is common to assume laminar flow conditions, i. e. Reynolds numbers below 1 - 10 (Bear, 1972). Then, the Stokes equations approximate the motion of an iso-viscous, iso-thermal and incompressible fluid at steady-state conditions by:

$$\mu \nabla^2 v = \nabla P, \tag{3.8}$$

$$\nabla \cdot v = 0, \tag{3.9}$$

with the fluid's dynamic viscosity μ, pressure P and velocity vector $v = (v_x, v_y, v_z)$, ∇, $\nabla\cdot$, and ∇^2 denote the gradient, divergence, and Laplace operator for 3D Cartesian coordinates,

respectively. We use the methodology described and benchmarked in (Eichheimer et al., 2019; Eichheimer et al., 2020) and already applied in Kottwitz et al. (2020) and Kottwitz et al. (2021) to obtain intrinsic permeabilities of fractured-porous media voxel data-sets. There, the 3D staggered grid finite difference code LaMEM (Kaus et al., 2016) is employed to solve equations 3.8 and 3.9, utilizing the PETSc framework (Balay et al., 2018) for high-performance-computing (HPC) optimized parallelisation. The volume average of the resulting velocities (e. g., Osorno et al., 2015) is substituted into Darcy's law to yield an intrinsic permeability value for the direction that corresponds to the direction of the applied pressure gradient.

3.2.4 Fracture dataset

For this study, we compiled a data-set of 18 CT-scanned fractures of various sources described in the following. The first three selected discontinuity models (D_{01}, D_{02} and D_{03}) were sampled in the scope of the German federal ministry of education and research (BMBF) funded project PERMEA (grant no. 03G0865A) from a tight carbonate quarry near Ittling in the Franconian Alb (Germany) featuring the Upper Jurassic (Malm) formation, a frequent targeted for geothermal energy production in the southern German Molasse Basin area (Cacace et al., 2013; Homuth et al., 2014; Przybycin et al., 2017). The three samples were scanned by the CoreTom scanner of XRE located in Ghent, Belgium, with a resolution of 14.5 μm (D_{01}) and 45 μm (D_{02} and D_{03}) and processed with ImageJ (Schneider et al., 2012). While D_{01} was identified as "classical" open fracture, microstructural analysis of D_{02} and D_{03} suggested a pressure solution-driven origin which therefore were classified as dissolution seam and open stylolite, respectively. The following five fracture models were obtained from Digital Rocks Portal (Prodanovic et al., 2015) (DRP). Sample N_{01} is retrieved from the published data set by Prodanovic et al. (2016) and represents a calcite coated open fracture within a micritic limestone from the Niobara formation, collected near Lyons, Colorado. It was imaged with a resolution of 26.69 μm at the University of Texas High-Resolution X-ray Micro-tomography Facility and already featured in publications by Tokan-Lawal et al. (2014) and Tokan-Lawal et al. (2017). Samples B_{01}, B_{02}, B_{03} and B_{04} represent subsets of a single fracture in a Bentheimer sandstone that was artificially cracked with a triaxial test. Both sides were brought together with an offset of 1mm and wrapped with Teflon for scanning and flow-through experiments (see Karpyn et al., 2007, for further details). The original scanned image was rescaled to produce a 3D binary data set with cubic voxels of 27.433 μm side length, which was featured in several publications already (Karpyn et al., 2007; Karpyn and Piri, 2007; Piri and Karpyn, 2007; Prodanovic et al., 2009; Crandall et al., 2010; Zhang et al., 2019) and cropped to four subsets before being published at Karpyn et al. (2016).

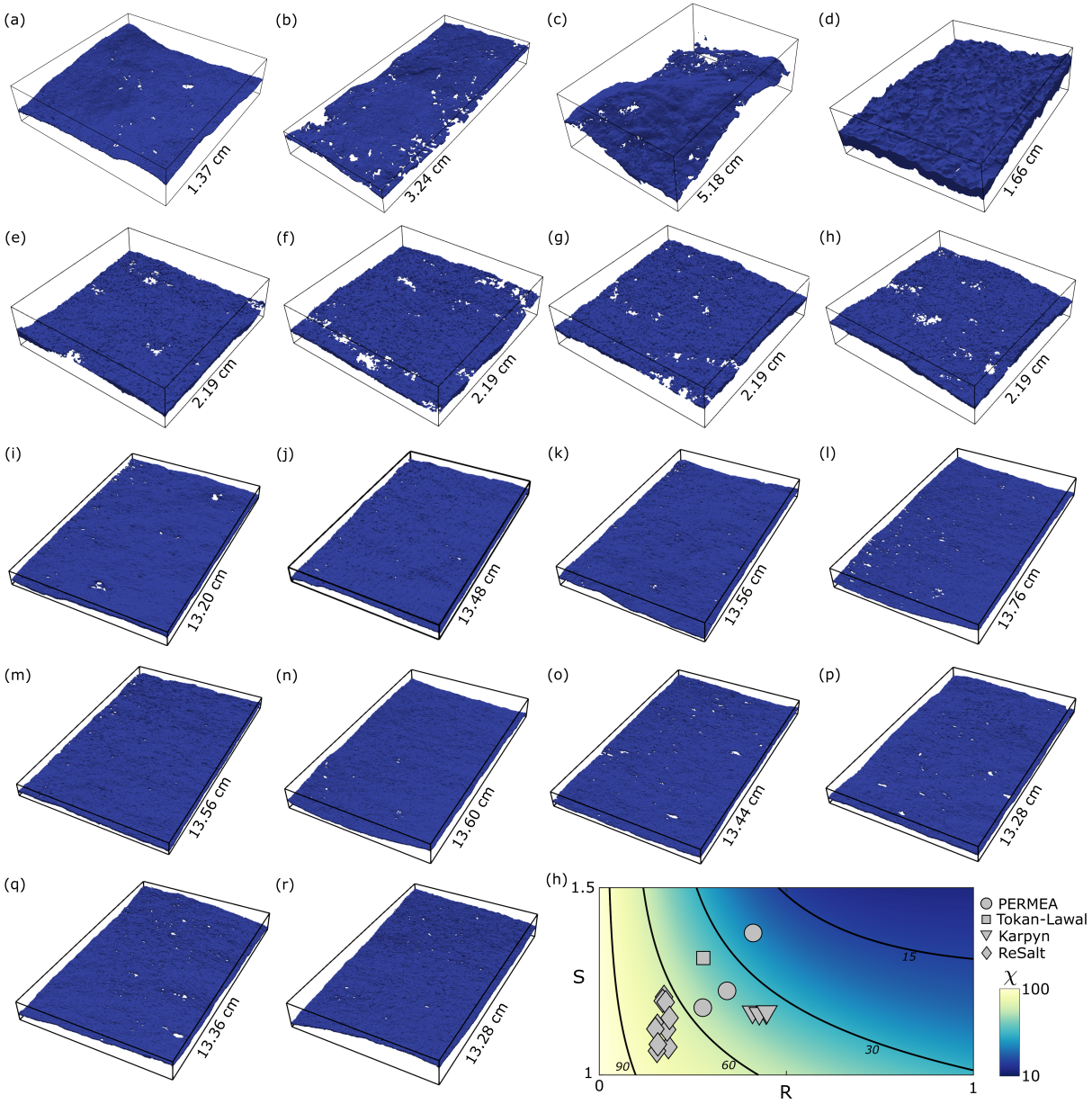

FIGURE 3.2: The void spaces for all 18 fracture voxel models after the PCA alignment process are displayed in this figure. The same voxel models were used to numerically estimate their permeabilities with LaMEM. In the following, panel indices are linked to sample names as indicated in the text: $a = D_{01}$, $b = D_{02}$, $c = D_{03}$, $d = N_{01}$, $e = B_{01}$, $f = B_{02}$, $g = B_{03}$, $h = B_{04}$, $i = R_{01}$, $j = R_{02}$, $k = R_{03}$, $l = R_{04}$, $m = R_{05}$, $n = R_{06}$, $o = R_{07}$, $p = R_{08}$, $q = R_{09}$, $r = R_{10}$. The physical length of the longest side of the model is indicated on the right for each sample. Panel h shows the geometrical configuration of each sample (grouped in four categories based on their origin) in terms of relative closure R and effective surface area S as defined in the text. The background color indicates the expected hydraulic efficiency χ in percent as defined by equation 16 in Kottwitz et al. (2020), the black lines depict chosen contours of χ with annotated values in percent.

TABLE 3.1: Summary table for fracture quantitative data. The voxel size of the aligned CT-model (v_s), the fractures mean aperture ($\bar{a}$), its standard deviation (σ_a), the fractures effective surface area(sa_f), its contact fraction (c), its relative closure (R) and effective surface area (S) are given in the columns for each of the 18 samples.

sample	v_s $[m]$	$\bar{a}$ $[m]$	σ_a $[m]$	sa_f $[m^2]$	c [ ]	R [ ]	S [ ]
D_{01}	13.5×10^{-6}	1.01×10^{-4}	2.82×10^{-5}	4.39×10^{-4}	0.0095	0.28	1.19
D_{02}	45×10^{-6}	2.46×10^{-4}	8.44×10^{-5}	1.10×10^{-3}	0.049	0.34	1.22
D_{03}	45×10^{-6}	6.75×10^{-4}	2.15×10^{-4}	4.20×10^{-3}	0.011	0.31	1.37
N_{01}	26.69×10^{-6}	1.37×10^{-3}	3.81×10^{-4}	5.70×10^{-4}	0.0003	0.28	1.31
B_{01}	27.433×10^{-6}	5.68×10^{-4}	2.32×10^{-4}	1.10×10^{-3}	0.013	0.40	1.17
B_{02}	27.433×10^{-6}	4.59×10^{-4}	2.05×10^{-4}	1.08×10^{-3}	0.030	0.45	1.16
B_{03}	27.433×10^{-6}	4.82×10^{-4}	2.06×10^{-4}	1.09×10^{-3}	0.015	0.42	1.16
B_{04}	27.433×10^{-6}	5.45×10^{-4}	2.44×10^{-4}	1.10×10^{-3}	0.016	0.45	1.17
R_{01}	200×10^{-6}	1.42×10^{-3}	2.64×10^{-4}	2.52×10^{-2}	0.0095	0.18	1.07
R_{02}	200×10^{-6}	1.16×10^{-3}	1.79×10^{-4}	2.71×10^{-2}	0.0060	0.15	1.06
R_{03}	200×10^{-6}	1.28×10^{-3}	1.99×10^{-4}	2.63×10^{-2}	0.0061	0.15	1.13
R_{04}	200×10^{-6}	9.69×10^{-4}	1.75×10^{-4}	2.61×10^{-2}	0.0052	0.18	1.12
R_{05}	200×10^{-6}	1.48×10^{-3}	2.59×10^{-4}	2.90×10^{-2}	0.0070	0.17	1.20
R_{06}	200×10^{-6}	1.10×10^{-3}	1.65×10^{-4}	2.55×10^{-2}	0.0007	0.14	1.12
R_{07}	200×10^{-6}	1.10×10^{-3}	1.82×10^{-4}	2.70×10^{-2}	0.0062	0.17	1.20
R_{08}	200×10^{-6}	1.12×10^{-3}	1.86×10^{-4}	2.42×10^{-2}	0.0075	0.16	1.08
R_{09}	200×10^{-6}	1.11×10^{-3}	2.05×10^{-4}	2.78×10^{-2}	0.0052	0.18	1.19
R_{10}	200×10^{-6}	1.13×10^{-3}	2.35×10^{-4}	2.58×10^{-2}	0.0027	0.18	1.15

The remaining 10 samples (R_{01} - R_{10}) were acquired in the scope of the German federal ministry of economy and energy (BMWi) funded project ReSalt (grant no. 032444A-D) in a quarry near Bebertal, Germany, featuring Permian sandstones (Flechtinger formation) and a quarry near Würzburg, Germany, featuring Upper Triassic sandstones (Remlinger formation). The samples were synthetically cracked with a Brazilian test, brought together and wrapped for scanning and further experiments, similar to the samples of Karpyn et al. (2007). For more details on sample preparation and experimentally determined effective properties, the reader is referred to Frank et al. (2020b) and Frank et al. (2020a), respectively, who feature these samples in their publications. All samples were scanned by a Medical CT-scanner (SOMATOM Definition AS VA48A) located at the Petroleum Engineering Department Montanuniversität Leoben with a resolution 200 μm. Pre-processing (rescaling, resampling and masking) was performed in Avizo (https://www.fei.com/software/amira-avizo/) while the segmentation was carried out with the random forest approach (e.g., Geurts et al., 2009) implemented in the Ilastik software package (Berg et al., 2019). The void space of every model after the alignment process described above is displayed in figure 3.2 and the corresponding metrics are given in table 3.1.

3.3 Results & Discussion

3.3.1 Correlation length estimation

The results of the correlation length analysis and fluid flow simulations for all 18 CT-scanned samples are presented and discussed in the following. The raw data sets have been pre-processed following the above-mentioned methodology to obtain an aligned voxel model, the aperture field, and both individual surfaces. PCA-based rotation were only required for samples D_{01-03} and R_{01-10}. PSD analysis was performed on the individual surfaces of each fracture and its aperture field to compute corresponding mismatch ratios. The minimal correlation length was estimated by manually picking the x-axis value of the plot, at which the curve starts to deviate significantly from unity. All resulting PSD and mismatch ratio plots are displayed in figure 3.3 and 3.4, whereas the final metrics are given in table 3.2. Generally, it was possible to determine a minimal mismatch ratio for every fracture sample. However, for samples N_{01} and B_{01-04}, the decrease from unity of the mismatch ratio was not as pronounced as in the other samples with final mismatch ratios between 0.2 and 0.4. Despite this, the long-wavelength tails in these plots (panels d_2, e_2, f_2, g_2 and h_2) significantly differ from the previous parts of the curves, which enabled to determine the minimum correlation length which for these fractures is close to the model lengths. Off-leveling of the power spectral density curves at short wavelengths is observed for the medical CT-scanned fractures (samples R_{01-10}) and the data provided from DRP (samples N_{01} and B_{01-04}). Usually, this is attributed to resolution effects (Jacobs et al., 2017), especially for the medical CT-scanned ones, but could also be induced by Thresholding algorithms in the segmentation process. Consequently, the mismatch ratio curves of the DRP samples level off from unity at shorter wavelengths. Since the correlation length estimate is conducted at larger scales, the result remains unbiased of this effect. However, the quantification of a fractal scaling trend across the full length-scale of the model is impeded. For large scales, the curves are not biased by resolution effects, and fractal behavior can be observed in the PSD data of the individual surfaces. However, due to the limited scaling range and resolution effects, we refrain from fitting scaling exponents to the data. Samples D_{01-03} and R_{01-10} display randomly occurring peaks with arbitrary amplitudes in the PSD curves. They seem to be caused by a sampling bias in the PCA alignment algorithm (induced by converting voxels to points and vice versa), as these effects are not observed in samples that didn't require an initial alignment (samples N_{01} and B_{01-04}).

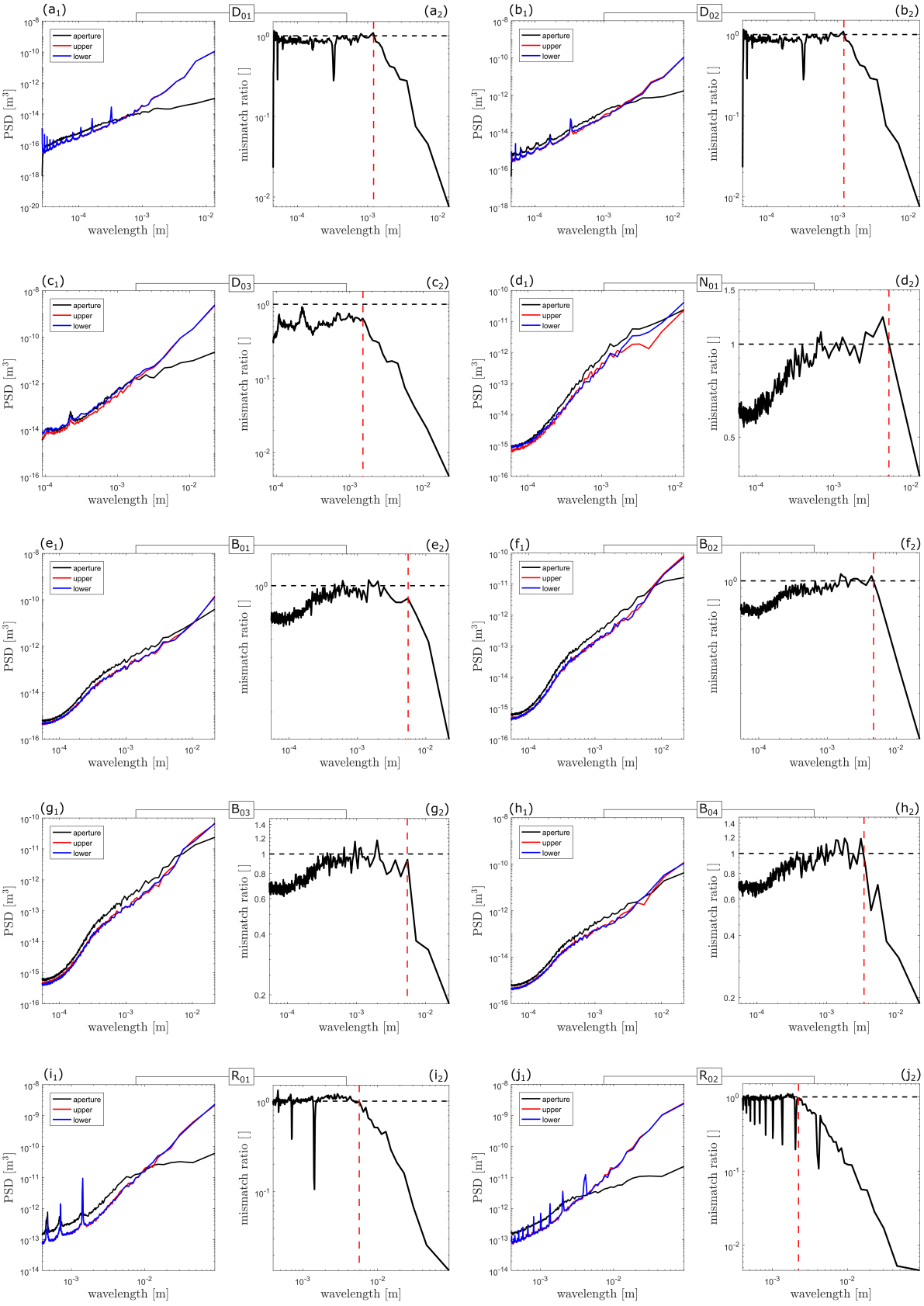

FIGURE 3.3: This figure expands to the next page. Refer to the caption of figure 3.4.

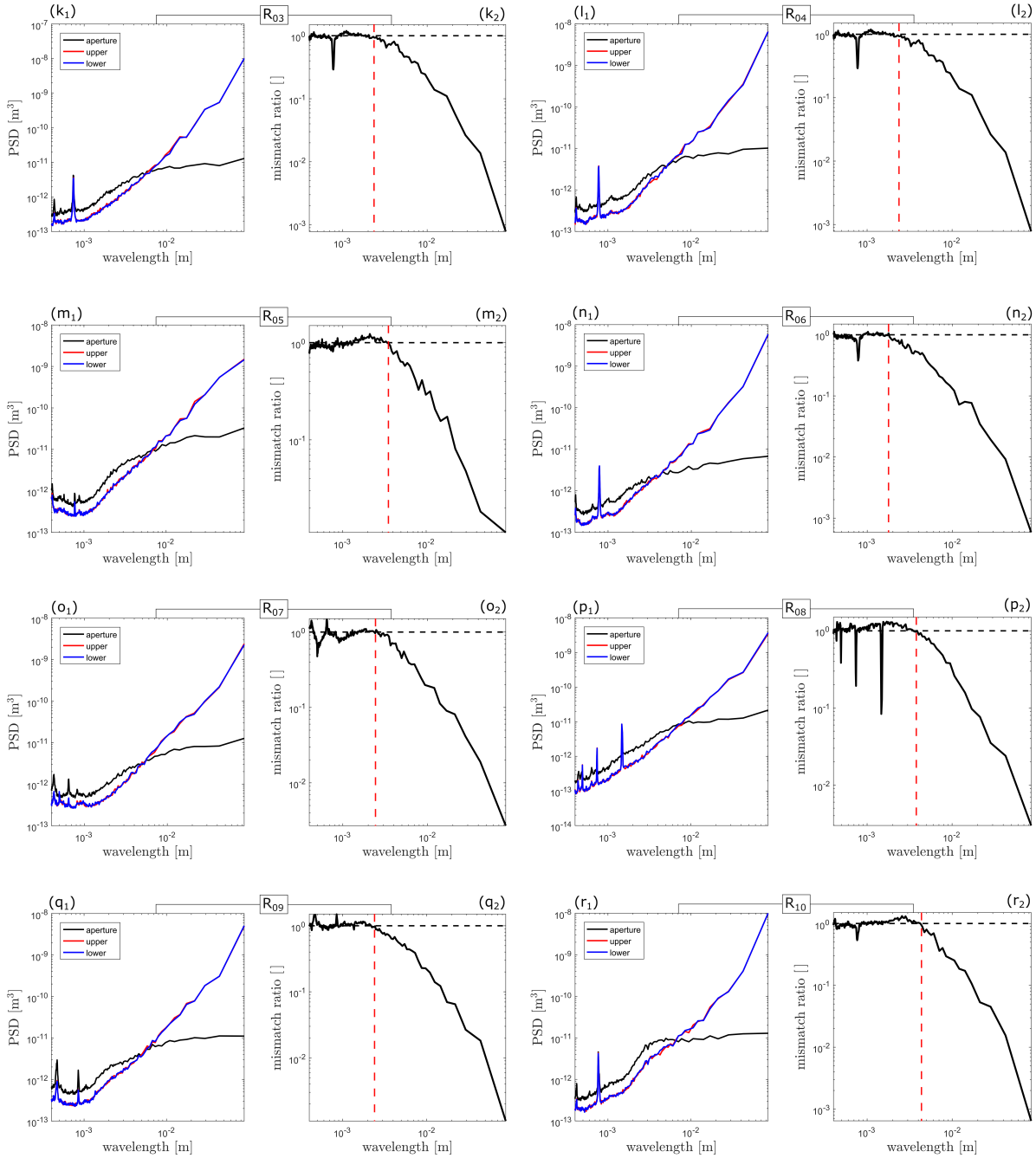

FIGURE 3.4: Results of the correlation length estimation analysis. Panel alphabetic indices are linked to sample names by: $a = D_{01}$, $b = D_{02}$, $c = D_{03}$, $d = N_{01}$, $e = B_{01}$, $f = B_{02}$, $g = B_{03}$, $h = B_{04}$, $i = R_{01}$, $j = R_{02}$, $k = R_{03}$, $l = R_{04}$, $m = R_{05}$, $n = R_{06}$, $o = R_{07}$, $p = R_{08}$, $q = R_{09}$, $r = R_{10}$. Subscript 1 for each panel index shows the power spectral densities of the aperture field and both fracture surfaces, subscript 2 displays the mismatch ratio plot from which the minimal correlation length is obtained by data-picking. There, the black dashed line indicates a mismatch ratio of 1 (i. e., non-matching and uncorrelated surfaces and aperture) and the red dashed line highlights the picked wavelength, at which the mismatch ratio starts to deviate from unity (i. e., the minimal mismatch or correlation length.

TABLE 3.2: Summary table for fracture analysis results. The first column indicates the hand-picked minimal correlation length l_c from the mismatch ratio plots (panel subscript 2 in figures 3.3 and 3.4), and the second column its ratio to the physical length L of each individual model. The third column displays the numerically predicted fracture permeability k_m from LaMEM. The next 6 columns indicate the L_2 error norm of the computed permeability to the one predicted by the parametrizations of Patir and Cheng, 1978 (e_{pc}), Brown, 1987 (e_b), Renshaw, 1995 (e_r), Zimmerman and Bodvarsson, 1996 (e_{zb}), Kottwitz et al., 2020 (e_k) and the cubic-law (e_{cl}) (e. g., Witherspoon et al., 1980; Long et al., 1982).

sample	l_c $[m]$	l_c/L	k_m $[m^2]$	e_{pc} [%]	e_b [%]	e_r [%]	e_{zb} [%]	e_k [%]	e_{cl} [%]
D_{01}	2.36×10^{-4}	0.017	1.32×10^{-11}	68.1	65.6	70.9	65.6	1.18	91.1
D_{02}	1.20×10^{-3}	0.037	1.63×10^{-10}	77.7	75.8	82.5	59.9	13.1	115
D_{03}	4.10×10^{-4}	0.047	1.45×10^{-10}	255	254	265	141	3.33	363
N_{01}	4.43×10^{-3}	0.26	2.64×10^{-8}	51.1	48.9	53.6	51.8	31.7	71.8
B_{01}	2.43×10^{-3}	0.11	1.29×10^{-9}	51.7	51.3	55.9	43.3	21.6	96.8
B_{02}	4.48×10^{-3}	0.19	5.76×10^{-10}	73.9	74.4	78.2	54.2	13.4	134
B_{03}	5.47×10^{-3}	0.25	5.56×10^{-10}	111	112	117	96.6	8.31	179
B_{04}	8.74×10^{-3}	0.16	8.74×10^{-10}	90.0	90.1	94.8	73.3	6.29	156
R_{01}	5.65×10^{-3}	0.043	1.90×10^{-8}	27.1	25.5	26.4	23.7	0.39	32.9
R_{02}	2.17×10^{-3}	0.015	9.06×10^{-9}	31.0	29.7	29.6	27.9	7.51	34.2
R_{03}	2.98×10^{-3}	0.021	8.61×10^{-9}	47.0	45.5	45.4	43.5	13.1	50.1
R_{04}	2.25×10^{-3}	0.018	3.63×10^{-9}	47.3	45.4	46.3	44.4	10.7	53.5
R_{05}	3.43×10^{-3}	0.025	2.05×10^{-8}	52.6	50.8	51.4	48.9	4.31	58.2
R_{06}	1.78×10^{-3}	0.013	5.45×10^{-9}	47.8	46.4	46.0	45.7	15.5	51.0
R_{07}	2.91×10^{-3}	0.021	6.64×10^{-9}	50.8	49.0	49.5	47.3	5.11	55.9
R_{08}	3.87×10^{-3}	0.029	9.29×10^{-9}	42.9	41.5	41.4	39.1	15.2	46.6
R_{09}	2.31×10^{-3}	0.017	2.99×10^{-9}	53.4	51.5	52.3	50.4	5.89	59.5
R_{10}	4.04×10^{-3}	0.030	5.94×10^{-9}	61.2	59.1	60.4	59.2	15.6	68.9

This results in sometimes stronger (sample R_{02}) or weaker (sample R_{04}) pronounced local peaks in the mismatch ratio curves as well. Providentially, these locally occurring sampling biases don't impede the manual picking of the correlation length, as the global trends of the curve are still clearly visible. Exceptional behavior in the mismatch ratio curve is evident in panel c_2 in figure 3.3 showing the data for sample D_{03}. There, the short-wavelength mismatch ratios range at a slightly lower level than unity. This could indicate that the aperture field of opened stylolites exhibits other approximations than being the sum of the upper and lower surface, as assumed for classical fractures (Ogilvie et al., 2006). Alternatively, this could be attributed to the still present slight overhangs in the CT data, although the model has been cropped to a region where substantial amounts of overlap were avoided. Yet, these effects didn't interfere with the procedure to determine the minimal correlation length, as the onset of long-range deviations from the mismatch ratio at short wavelengths was clearly definable.

3.3.2 Fracture permeability prediction

The numerically estimated permeabilities for all 18 fracture samples are given in table 3.2. To evaluate the applicability of functional parametrizations for fracture permeability, we compute the error norm of the numerically measured permeability k_m to predicted permeabilities k_p

TABLE 3.3: All parametrization models considered to predict fracture permeability k_p in this study. A prerequisite for all prediction models is the permeability predicted with the cubic law (k_{cl}), which is multiplied with a custom factor for each model for permeability predictions. The mean aperture is given by $\bar{a}$ as defined in eq. 3.2. L_z gives the width of the voxel model in the perpendicular direction to the fracture plane, which is needed to calculate the rescaling factor for the cubic law to account for the whole model, not only the fracture void. The standard deviation of the aperture field is given by σ_a and the fractional amount of contact by c. The relative closure is given by R as defined by eq. 3.1 and the effective surface area by S as defined in eq. 3.3. The formula to predict the permeabilities of Kottwitz et al. (2020) could be used as presented in the paper while the rest was reformulated from the hydraulic to mechanical aperture relations presented in each paper.

Parametrization model	Formula to compute k_p
Cubic law (k_{cl})	$\frac{1}{12}\bar{a}^2\frac{\bar{a}}{L_z}$
Patir & Cheng (1978)	$k_{cl}\left(1-0.9e^{-0.56\frac{\bar{a}}{\sigma_a}}\right)$
Brown (1987)	$k_{cl}\left(1-0.743e^{-0.478\frac{\bar{a}}{\sigma_a}}\right)$
Renshaw (1995)	$k_{cl}\left(\frac{\sigma_a^2}{\bar{a}^2}\right)^{-1.5}$
Zimmermann & Bodvarsson (1996)	$k_{cl}\left(1-1.5\frac{\sigma_a^2}{\bar{a}^2}\right)\left(1-2c\right)$
Kottwitz et al. (2020)	$k_{cl}\left(1-\left(0.48\tanh\left(0.51S\right)+0.54\right)\tanh\left(\frac{R}{39.28\tanh\left(-2.45S\right)+39.47}\right)\right)$

according to:

$$e_p = \left|\frac{k_m - k_p}{k_p}\right|. \tag{3.10}$$

The formulas to compute the predicted permeabilities of the most cited models in the literature and the recently proposed model by Kottwitz et al. (2020) are given in table 3.3. The resulting prediction errors (eq. 3.10) for each considered model are displayed in table 3.2. Figure 3.5 shows a box plot of the prediction errors, indicating that with a median error of 9.5 % the parametrization of Kottwitz et al. (2020) gives the best approximation of the numerically estimated permeabilities of all fractures. There, the largest error was recorded for the fracture model N_{01}, which has the largest l_c/L ratio of the whole data set. In contrast, the highest error for all other models was recorded for sample D_{03}, showing the largest effective surface area. These results confirm the findings of Kottwitz et al. (2020) that incorporating a statistical measure accounting for the geometrical properties of both individual fracture surfaces into a parametrization model improves the accuracy of numerical permeability predictions. Furthermore, the applicability of this model for real data has been proven by the comparatively low median prediction error. Panel *a* in figure 3.6 presents the error of the Kottwitz et al. (2020) model as a function of the ratio between correlation length and fracture size (l_c/L) which according to Méheust and Schmittbuhl (2003) is the primary control on the non-unique behavior of fracture permeability predictions. There, the largest prediction error is recorded for the highest l_c/L ratio, and a global trend of increasing errors for larger l_c/L ratios was determined by linear regression ($e_p \propto 0.68 l_c/L$). This confirms that the variance of predicting an average flow

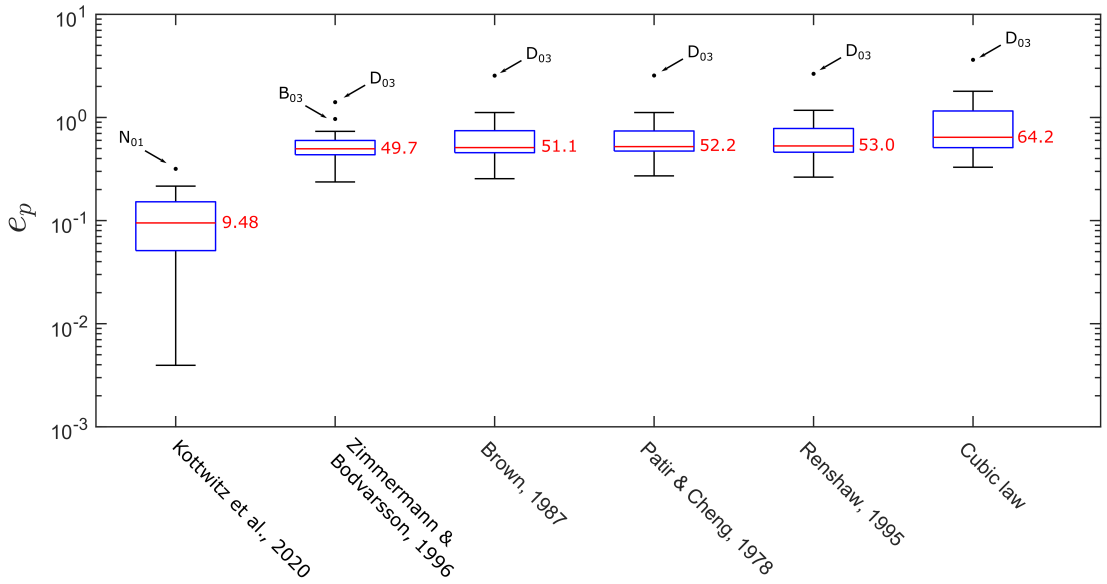

FIGURE 3.5: Box plot of the absolute prediction errors e_p calculated according to eq. 3.10 for various predicted permeabilities k_p by the models indicated in table 3.3, ordered in ascending order with respect to their median values. The whiskers of each box plot have a length of 1.5 times their interquartile range, such that every point falling outside of that range is considered as an outlier, denoted with a black point with annotations for respective sample names. The median values in percent for each box plot are indicated in red next to the box.

behavior for fracture populations with equal statistics increases for fractures with correlation lengths closer to the size of the flow system (Méheust and Schmittbuhl, 2003). Theoretically, the models with l_c/L ratios below 1/16 (samples D_{01-03} and R_{01-10}) should show the lowest prediction errors. However, we observe scattering of the errors up to 15 % for these models, which is most likely attributed to method intrinsic error induced by low numerical resolutions. As reported by Kottwitz et al. (2020), the resolution perpendicular to the applied flow direction is the most crucial to determine the accuracy of numerical fracture permeability predictions. They estimated the method intrinsic error of their parametrization model to be about 7.2 % for their chosen numerical resolutions with a classical resolution test. To obtain a rough estimate of a general method intrinsic error for this study, we produced an error curve based on the cubic law parametrization shown in the inlet plot of panel *b* in figure 3.6. It is based on several numerical simulations with parallel plate fracture geometries discretized with n_c cells (starting from 1 to 50). For each model, we then numerically simulate the permeability and compute the absolute error to the analytical solution of the cubic law by eq. 3.10. The maximum error of 66 % for a fracture with 1 cell discretization width (i. e., the numerical resolution of the fractures aperture) quickly converges to zero. The outer plot in panel *b* of figure 3.6 displays the flow-perpendicular discretization width (i. e., aperture divided by cell size) for representative samples of each data set. Thus, samples of the ReSalt group (R_{01-10}) are assumed to show the largest method intrinsic errors while numerically predicting their permeabilities, as their mean discretization width is about 7 cells on average. Based on the error curve of the inlet plot, this

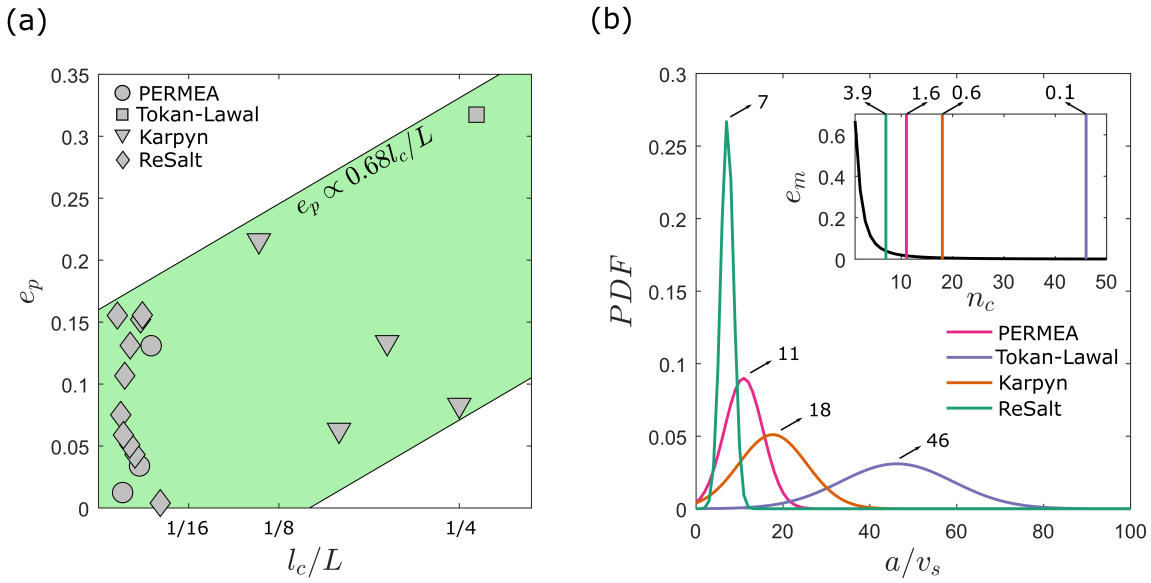

FIGURE 3.6: Panel *a* shows the permeability prediction error of Kottwitz et al. (2020) (e_p) as a function of the correlation length to size ratio (l_c/L) for each fracture sample of the data set Grey symbols indicate the origin group of the fracture samples. The green band indicates the interpreted trend of error increase with its proportionality (approximated by linear regression) indicated below the top edge. Panel *b* displays the fitted probability distribution functions (PDF) of the aperture (a) to voxel-size (v_S) ratio, i. e., the discretization width, of representative samples for each group (D_{01}, N_{01}, B_{01}, R_{01}). The indicated values at the peaks of each normal distribution function indicate the mean discretization width. The inlet plot of panel *b* shows the error curve to approximate the method intrinsic error of the numerical permeability predictions used in this study. The error e_m is computed from the resulting permeabilities of numerical simulations in parallel-plate fractures of n_c cells discretization width and the analytical solution of the cubic law. The colored vertical lines indicate the number of cells (n_c) of the annotated average discretization widths from the outer plot for the respective groups, while their error percentages are given above.

corresponds to an error of 3.9 %. The increasing mean discretization widths (indicated in *b*, figure 3.6) for the other groups (11, 18 and 46) correspond to lower errors (1.6, 0.6 and 0.1 %). Thus a scatter of 15 % in the permeability prediction model for l_c/L ratios below 1/16 could be induced by their lower discretization widths combined with a propagated method intrinsic error during the fitting of the Kottwitz et al. (2020) model. Theoretically, the results of the numerical flow simulations within the fracture samples, especially for the ones with low discretization widths, could be improved by doubling the numerical resolutions while maintaining the original CT-derived structure, similar as done for the resolution tests in Eichheimer et al. (2019) or Eichheimer et al. (2020). Yet, this would result in computationally unfeasible numerical resolutions in the dimensions of the fracture plane (x- and y-direction in this case), as cropping these to lower, computationally more feasible sizes would reduce the models l_c/L ratio and hence, by theory, increase the prediction error e_p. Thus, we accept the scatter of prediction errors for the fractures with l_c/L ratios below 1/16, as it does not severely bias identifying the global trend of increasing errors for larger l_c/L ratios, although it could potentially clarify this trend.

3.3.3 Aperture-correlation-length model

The correlation length in single fractures has already been identified as the main control on predicting their average flow behavior (Méheust and Schmittbuhl, 2003; Kottwitz et al., 2020). Its effect on network scale flow was, to our knowledge, are only addressed by two studies. Small-scale fracture networks with system sizes close to a constant prescribed correlation length for all fractures, Dreuzy et al. (2012) have shown that local aperture variations affect network scale flow. For kilometer-scale networks, Makedonska et al. (2016) have shown that aperture variations correlated up to certain fractions of the fracture length affect network flow and transport properties only if aperture variability and correlation length fractions are sufficiently high. Thus, both studies indicate that in-fracture variabilities induced by the correlation length in single fractures affect network flow behavior only under the condition that the maximum fracture scale correlations range close to system sizes. Both have used simple assumptions for prescribing the correlation length of each fracture in their network due to the absence of a physical model that relates the correlation length. Dreuzy et al. (2012) provided constant correlation length values for all fractures in the network, regardless of their length, and Makedonska et al. (2016) used a simple relation to the fracture length. Alternatively, with the results provided in this study and some data from the literature, it is possible to derive a simple model based on real data as a first-order approximation for the application in fracture network flow models. For this, we argue that this form of correlation should be based on firm measurements that are anyway required for a hydraulic description of a fracture. The actual fracture length is often difficult to measure in the field due to censoring or truncation effects (e. g., Bonnet et al., 2001; Lu et al., 2017) and usually not reported in combination correlation length measurements, the most straightforward quantity to find correlations with is the mean aperture ($\bar{a}$, eq. 3.2). Indeed, compiling the data of this study with the results of Ogilvie et al. (2006) (estimated mismatch length and arithmetic mean aperture) and Glover et al. (1998a) (mean mismatch length, computed from their upper (λ^1) and lower (λ^2) estimates as well as arithmetic mean aperture) in figure 3.7 suggest that the correlation length is decently approximated with a linear relationship to the fractures mean aperture in the form of:

$$l_c = \beta \bar{a}. \tag{3.11}$$

Here, β ranges between 1 and 13 to incorporate all data points, whereas linear regression suggests $\beta = 2.93$. Unfortunately, the data-set of the pioneering study of Brown (1995) could not be included in this graph, as they dont report measures for average apertures.

3.4 Summary & Conclusion

For this study, a data set of 18 CT-imaged fractures was compiled to (1) measure the correlation length of their aperture fields and to (2) numerically assess their permeabilities for an evaluation of the accuracy of several parametrization models from the literature. We provided some pre-processing guidelines applicable to any single fracture CT-data set with arbitrary orientation to reconstruct individual surfaces and aperture fields from binarized voxel models.

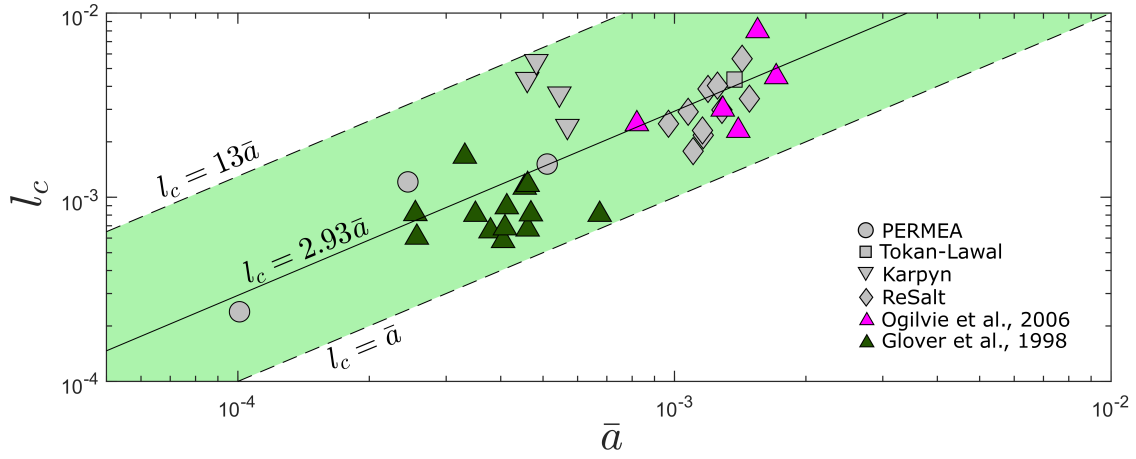

FIGURE 3.7: The correlation length l_c as a function of the mean aperture $\bar{a}$ for all measurements from this study as well as Glover et al. (1998a) and Ogilvie et al. (2006). The light green area indicates the range incorporating all measurements of the interpreted linear relationship, the black line gives the result of a linear regression to the data with annotated functional relations.

Next, we applied PSD analysis to this reconstructed data to derive mismatch ratio plots as suggested by Ogilvie et al. (2006), to determine the minimal correlation length of each sample. Additionally, we computed the directional permeability of each sample from finite-difference Stokes-flow simulations (e. g., Eichheimer et al., 2019; Eichheimer et al., 2020; Kottwitz et al., 2020) and compared to the permeabilities predicted according to Patir and Cheng (1978), Brown (1987), Renshaw (1995), Zimmerman and Bodvarsson (1996), and Kottwitz et al. (2020). This lead to the following main results:

(i) An adequate prediction of fracture permeability requires statistical measures accounting for the properties of the individual surfaces, not only the aperture field. This was already expected due to the findings of Kottwitz et al. (2020). Now it has been proven its applicability by a median permeability prediction error of only 9.48 % for their model on a large data set of natural fractures.

(ii) The error of the functional permeability prediction increases with respect to the ratio of the fractures correlation length to its size. This confirms the theoretical findings of Méheust and Schmittbuhl (2003) and Kottwitz et al. (2020), that uniquely predicting an average flow behavior of fractures is constrained to low correlation-length-to-size ratios.

(iii) Synthesizing the estimates of the minimal correlation length of this study with additional measurements from the literature demonstrated that the onset of correlation within the aperture field tends to range in the same order of magnitude as the average aperture. Thus, a simple linear relationship between the correlation length and the mean aperture serves as parametrization for network-scale models.

Prescribing constant fracture permeabilities with a modified parallel plate model is still common practice in network-scale models, especially for discrete fracture network (DFN) models (e. g., Lei et al., 2017; Berre et al., 2019; Lavoine et al., 2019; Sweeney et al., 2020). However,

based on the results of Dreuzy et al. (2012) and Makedonska et al. (2016), the validity of that assumption is put at risk for network models that show fracture scale correlations close to the size of the studied system. Considering that correlation lengths of fractures seem to range in similar orders of magnitude as their mean apertures, it is questionable if this condition is achievable for fractures in classical applications of network-scale flow models. Since several studies proposed that fracture aperture correlates to its length, either linearly (Pollard and Segall, 1987; Renshaw and Park, 1997) or sub-linearly (Olson, 2003; Klimczak et al., 2010), fracture apertures will always be several orders of magnitude lower (1 to 3 for dikes, more than 3 for joints according to the aforementioned sources) than their sizes and thus should be their correlation lengths. Hence, if network-scale flow in systems of size close to the maximum considered fracture aperture are modeled, either the methods of Dreuzy et al. (2012) and Makedonska et al. (2016) to prescribe in-fracture flow heterogeneity or direct-flow simulations within resolved geometries of fracture networks should be favored against the classical DFN approach. As long as the systems maximum aperture is about two orders of magnitude lower than the system size (rough approximation arising from a minimal required l_c/L ratio of $1/16$ for a unique permeability prediction within a fracture and a linear correlation length model with moderate β of 6), utilizing a modified parallel plate model for prescribing fracture-scale flow should be valid. It is important to note that this conclusion only holds for fractures with a slight amount of slip, as the results of Zambrano et al. (2019), for example, suggest that the correlation length increases as a function of slip. If faults, i. e., fractures with severe shear displacements, are considered in network-scale flow models, long-range flow correlations within the fault might well be of similar size as the whole system. They thus require individual treatment for prescribing their hydraulics in larger-scale flow simulations, which poses an exciting challenge for a follow-up study. Additionally, the origin of the correlation length, either physically or stochastically, is still not understood so far and will hopefully be addressed in future studies, next to the question if or how fluid-rock-interactions like dissolution or mineral growth as well as particle transport-induced clogging and overhangs in the voxel-model modify long-range correlations within fracture flow.

Chapter 4

Equivalent continuum-based upscaling of flow in discrete fracture networks: The fracture-and-pipe model [1]

4.1 Abstract

Predicting effective permeabilities of fractured rock masses is a crucial component of reservoir modeling. This is often realized with the discrete fracture network (DFN) method, where single-phase incompressible fluid flow is modeled in discrete representations of individual fractures in a network. Depending on the overall number of fractures, this can result in high computational costs. Equivalent continuum models (ECM) provide an alternative approach by subdividing the fracture network into a grid of continuous medium cells, over which hydraulic properties are averaged for fluid flow simulations. While this has the advantage of lower computational costs and the possibility to include matrix properties, choosing the right cell size for discretizing the fracture network into an ECM is crucial to provide accurate flow results and conserve anisotropic flow properties. Whereas several techniques exist to map a fracture network onto a grid of continuum cells, the complexity related to flow in fracture intersections is often ignored. Here, we utilize numerical simulations of Stokes-flow in simple fracture intersections to analyze their effect on permeability. We demonstrate that intersection lineaments oriented parallel to the principal direction of flow increase permeability in a process termed intersection flow localization (IFL). We propose a new method to generate ECM's that includes this effect with a directional pipe flow parametrization: the fracture-and-pipe model. Our approach is tested by conducting resolution tests with a massively parallelized Darcy-flow solver, capable of representing the full permeability anisotropy for individual grid cells. The results suggest that as long as the cell size is smaller than the minimal fracture length and larger than the maximal hydraulic aperture of the considered fracture network, the resulting effective permeabilities and anisotropies are resolution-independent. Within that range, ECM's apply to upscale flow in fracture networks, which reduces computational expenses for numerical permeability predictions of fractured rock masses. Furthermore, incorporating the off-diagonal

[1] This chapter was submitted to Solid Earth (Kottwitz, M. O., Popov, A. A., Abe, S., and Kaus, B. J. P., IN REVIEW, https://doi.org/10.5194/se-2020-208)

terms of the individual permeability tensors into numerical simulations results in an improved representation of anisotropy in ECM's, previously reserved for the DFN method.

4.2 Introduction

Discontinuities in rocks provide major pathways for subsurface fluid migration. Thus, fractured reservoirs are frequent targets for oil, gas, or water production, geothermal energy recovery, and CO_2 sequestration. In addition, both the safety of nuclear waste disposals and subsurface contaminant transport crucially depend on the presence of fractures. Characterizing natural fracture networks across scales and predicting their permeabilities to model fluid flow therein has thus been a long-standing topic of research (e.g., Long et al., 1982; Dershowitz and Einstein, 1988; Cacas et al., 1990; Neuman, 2005; Dreuzy et al., 2012).
Since the acquisition of fracture data is usually limited to borehole logs, or outcrop scans (Lei et al., 2017), the discrete fracture network (DFN) model is commonly used as a conceptual framework to provide statistically-based approximations of real fracture networks (Darcel et al., 2003; Xu and Dowd, 2010; Davy et al., 2013; Maillot et al., 2016). Measured structural properties like size- and orientation-distributions (Odling et al., 1999; Healy et al., 2017) as well as fracture density and spacing (Ortega et al., 2006) serve as quantitative basis to generate synthetic DFN realizations for further analysis (e.g., Hyman et al., 2015; Alghalandis, 2017). The hydraulic response to pressure changes of each fracture is then parametrized with the cubic law (Snow, 1969; Witherspoon et al., 1980), relating the fracture's effective permeability to its aperture. In reality, surface roughness, fracture closure, and fluid-rock interactions (e.g., erosion or crystal growth) cause deviations from the parallel-plate assumption (Brown, 1995; Oron and Berkowitz, 1998; Méheust and Schmittbuhl, 2000). Semi-empirical functions derived from numerical simulations in rough-walled fractures with quantified statistics of the aperture field (e.g., Patir and Cheng, 1978; Brown, 1987; Renshaw, 1995; Zimmerman and Bodvarsson, 1996; Mourzenko et al., 2018) serve as corrections to the cubic-law, if the fractures internal correlation length-scale is significantly smaller than the size of the considered fracture (e.g., Méheust and Schmittbuhl, 2003; Kottwitz et al., 2020).
A large number of numerical methods to compute effective permeabilities of fractured media have been developed (see reviews of Jing, 2003; Berre et al., 2019), all relying on (modified) cubic-law assumptions. Improved discretization techniques with individual fracture treatment like the DFN method come at the cost of high computational expenses, making it difficult to employ it for reservoir scale simulations. Discretizing the fractured media as equivalent continuum blocks significantly reduces the computational effort at comparable numerical accuracy (Hadgu et al., 2017).
According to Long et al. (1982) and Oda (1985), fractured rocks behave similar to porous media. They can be represented by a positive definite permeability tensor (Chen et al., 1999) as long as the considered system behaves like a representative elementary volume (REV) (Bear, 1972), i.e., its effective properties (permeability or porosity, for example) are more or less homogenous at the reference scale of the system. Due to the multi-scale character of fracture systems (e.g.,

Bonnet et al., 2001; Davy et al., 2006), determining the required homogenization scale is difficult, as distinct larger features may dominate overall flow. Thus, a discrete representation of all fractures in a network given by the DFN method is essential to capture that multi-scale character adequately. La Pointe et al. (1995), Jackson et al. (2000), Svensson (2001), Leung et al. (2012) and Hadgu et al. (2017), among others, have however showed, that representing a DFN with a grid of equivalent continuum blocks of sizes lower than the REV yields similar flow results, if resolved sufficiently, and thus reproduces the overall flow-behaviour of the DFN method. This highlights that the use of continuum methods for flow modeling in fractured rocks is not restricted to REV scales and can thus be used equivalently to the DFN method.

Several techniques to generate equivalent continuum models (ECM) of DFN's have been developed in 2D (Reeves et al., 2008; Botros et al., 2008; Rutqvist et al., 2013; Chen et al., 2015) and 3D (Hadgu et al., 2017; Sweeney et al., 2020), whereby the so-called Oda method (see Oda, 1985) is used to formulate permeability tensors of grid cells that intersect fractures. There, the permeability tensor aligns with the orientation of the intersecting fracture, and the permeabilities of the individual fractures are summarized if multiple fractures intersect one cell, yielding a positive definite, fully anisotropic tensor (e.g., Chen et al., 1999). The groundwater-flow equations for porous media (Bear, 1972), i.e., Darcy's law (Darcy, 1856), are then used to simulate laminar, steady-state, single-phase flow to compute effective permeabilities of the medium. However, commonly used 3D flow solvers like PFLOTRAN (Lichtner et al., 2015) or MODFLOW (McDonald and Harbaugh, 1988) have numerical difficulties treating fully anisotropic permeability tensors and rather use their principal components or maximum values for flow simulations. So-called stair-case patterns are the direct consequence of these simplifications, which introduce artificially prolonged flow paths, especially in transport simulations, which have to be compensated for (e.g., Reeves et al., 2008; Botros et al., 2008; Sweeney et al., 2020) when predicting effective permeabilities of fractured media.

This study focuses on an often ignored but important aspect in fracture network modeling given by the complexity of fracture intersection flow. To our knowledge, only a few studies have presented 3D flow simulations within fracture intersections (Zou et al., 2017; Li et al., 2020), revealing the fact that flow velocities will increase within the fracture intersections compared to the fractures itself (shown by increasing Péclet numbers within the intersections). Theoretically, this effect should increase if the direction of the applied pressure gradient aligns with the orientation of the intersection. As a consequence, the effective permeability should increase by a certain amount within the intersection. To demonstrate that, we systematically conduct 3D numerical simulations of Stokes flow within differently oriented, planar fracture crossings to analyze the permeability increase caused by intersection flow localization (IFL). Using these results, we extend the current state-of-the-art methodology for equivalent continuum representations of DFN's to account for IFL in a quantitative manner and analyze its impact on effective permeability computations. There, it is still unclear at which level of detail the ECM has to be discretized to conserve the structural complexity of the DFN, as aforementioned stair-case patterns and artificial connectivity cause resolution dependencies. Subsequently, resolution tests are performed on two DFN test cases with a newly developed, massively parallelized high-performance-computing (HPC) optimized finite element Darcy-flow solver that is capable of

handling fully anisotropic permeability tensor cells. By that, we consistently investigate the upscaling capabilities of the ECM method, which is frequently used for effective permeability predictions in fractured porous media.

4.3 Methods

4.3.1 Fracture intersection flow modelling

Fluid flow in porous and fractured media is described by the well-known Navier-Stokes equations (Bear, 1972). It is commonly assumed that sub-surface flow in fractures ranges in the laminar regime, i.e. Reynolds numbers below unity (Zimmerman and Bodvarsson, 1996). Assuming the flowing fluid to be incompressible, isoviscous and the impact of gravity to be negligible, steady-state flow at constant temperature is defined by Stokes momentum balance (eq. 4.1) and continuity (eq. 4.2) equations (Bear, 1972):

$$\mu \nabla^2 v = \nabla P, \tag{4.1}$$

$$\nabla \cdot v = 0, \tag{4.2}$$

with the fluid's dynamic viscosity μ, pressure P and velocity vector $v = (v_x, v_y, v_z)$. ∇, $\nabla\cdot$, and ∇^2 denote the gradient, divergence, and Laplace operator for 3D Cartesian coordinates, respectively.
Here, the 3D staggered grid, finite-difference code LaMEM (Kaus et al., 2016) is used to solve the coupled system of equations 4.1 and 4.2, utilizing PETSc (Balay et al., 2018) for HPC optimisation. Applying different absolute pressures on two opposing sides of a 3D voxel model representing the fractured or porous medium (e.g., a) or d) in figure 4.1) while setting the other boundaries to no-slip (velocity component normal to the boundary is zero) enables the prediction of the mediums directional permeability. After obtaining the steady-state solution, the volume integral of the pressure-gradient aligned velocity component v_z (e.g., Osorno et al., 2015) is computed according to:

$$\bar{v} = \frac{1}{V} \int_V |v_z| \, dz, \tag{4.3}$$

with domain volume V. Using Darcy's law for flow through porous media (Darcy, 1856), that relates the specific discharge Q according to:

$$Q = -\frac{kA\Delta P}{\mu}, \tag{4.4}$$

with intrinsic permeability k and cross-sectional area A in combination with the fact that $Q = \bar{v}A$, the directional permeability k_z is calculated by:

$$k_z = \frac{\mu \bar{v}}{\Delta P}. \tag{4.5}$$

As demonstrated by Eichheimer et al. (2019), Kottwitz et al. (2020), and Eichheimer et al. (2020),

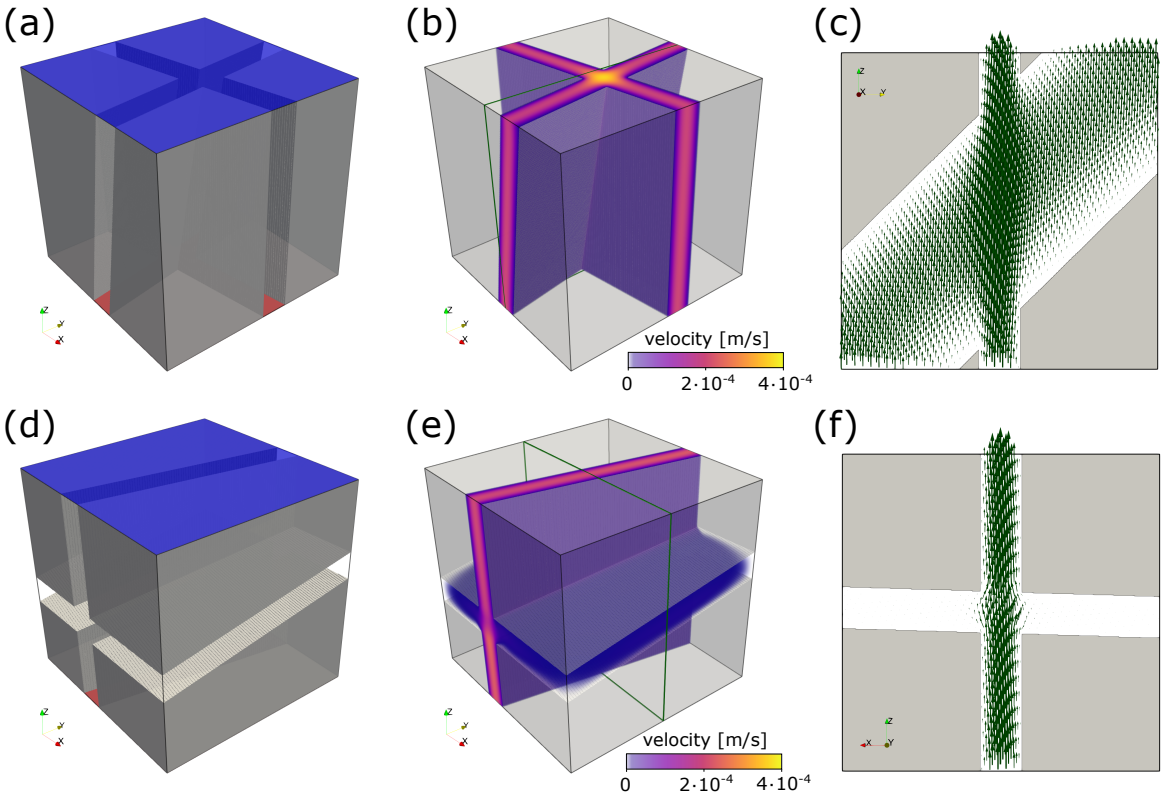

FIGURE 4.1: Panels *a* and *d* show the binary voxel-models (impermeable matrix in transparent gray) for a fracture intersection that is orientated along and transverse to the flow direction, respectively. The red bottom faces is the high pressure boundary (0.02 *Pa*), the blue top faces the low pressure boundary (0.01 *Pa*) forcing the fluid to flow in *z*-direction. The orientations (arranged as dip-direction/dip) for the fracture pair in *a* are $f_1 = 100/90$, $f_2 = 190/80$, and $f_1 = 170/90$, $f_2 = 260/10$ for the fractures in *d*. The length of both cubes is 1 *cm* and all fracture apertures are constant (1.25 *mm*). Panels *b* and *e* visualize flow velocity distribution in the void space. Panels *e* and *f* highlight velocity vectors within the intersections at slices indicated with green rectangles in *b* and *e*, respectively.

the numerical resolution has to be sufficiently high to produce a converged result. Generating every model at different levels of detail (e.g. 128^3, 256^3 , 512^3 and 1024^3 voxels), ensures that the most accurate solution is obtained (see comparison of errors to the result at largest resolution in plot b, figure 4.7). Figure 4.1 presents Stokes-flow in simple fracture intersections and highlights the IFL effect. If the fracture intersection is aligned with the principal flow direction (plot *a* - *c* in figure 4.1), the velocity significantly increases within the intersection, resulting in higher directional permeabilities. In the opposite case, when the fracture intersection connects no-pressure boundaries (plot *d* - *f* in figure 4.1) and is thus oriented oblique to the flow direction, the flow velocity slightly disperses around the intersection and the overall impact on the directional permeability is minor.

4.3.2 Permeability parametrization concepts

As the two main structural features (fractures and intersections) composing a fracture network differ significantly in terms of their hydraulics (figure 4.1), they require independent concepts to parametrize their permeabilities for formulating their effective grid block permeability tensor. For fractures, it is usual practice to use the cubic-law parametrization Snow (e.g., 1969) and Long et al. (1982), relating the specific discharge Q through a void system between two parallel plates according to:

$$Q = -\frac{w a_m^3 \Delta P}{12\mu}, \tag{4.6}$$

with the fractures width w and distance between the two plates, i.e. mechanical aperture a_m. Comparing this analytical solution with Darcy's law (eq. 4.4, cross-sectional area $A = w a_m$) leaves the intrinsic permeability of a fracture k_f defined by:

$$k_f = \frac{a_m^2}{12}. \tag{4.7}$$

Natural fractures deviate from the assumptions of parallel plates, which is why a_m in eq. 4.7 is commonly replaced with a hydraulic aperture a_h that corrects the parametrization for fracture closure and surface roughness (e.g., Patir and Cheng, 1978; Brown, 1987; Renshaw, 1995; Zimmerman and Bodvarsson, 1996; Kottwitz et al., 2020). Yet, there is no ready to use parametrization concept tailored for fracture intersections. The simulations shown on figure 4.1 suggest that the flow in the intersection is approximately pipe-like. Then, the specific discharge Q through a tube of radius r_t and length l_t is related by the Hagen-Poiseuille flow solution through a pipe (e.g., Batchelor, 1967) according to:

$$Q = -\frac{\pi r_t^4 \Delta P}{8 l_t \mu}. \tag{4.8}$$

Again, combining this equation with Darcy's law (eq. 4.4, cross-sectional area $A = \pi r^2$) results in the following expression for the intrinsic permeability of a pipe k_i:

$$k_i = \frac{r^2}{8}. \tag{4.9}$$

The apparent pipe radius should then be modified based on the intersection shape to calculate an equivalent hydraulic radius r_h to compensate for the structural difference. As a first-order approximation, we use half the size of the hypotenuse in a right-angled triangle whose legs are the two intersecting apertures (called half-hypotenuse assumption in the following, see figure 4.2 for details). This delivers sufficiently good results, as demonstrated later (figure 4.8).

4.3.3 Equivalent continuum representation of DFN's

The use of the ECM approach instead of the DFN method to predict the effective permeabilities of fractured media crucially depends on the capability to reflect the anisotropic flow properties at the scale of the continuum cells. Therefore, it is essential to integrate the geometry of a DFN

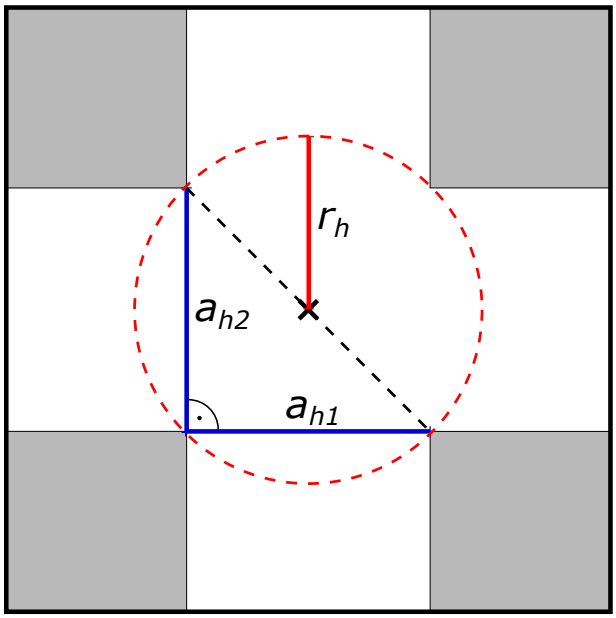

FIGURE 4.2: 2D Sketch of the half-hypotenuse assumption in an idealized rectangular fracture crossing (grey regions indicate rock matrix, white regions fracture pore space). The hydraulic apertures (a_{h1} and a_{h2}) of both intersecting fractures are indicated with solid blue lines. The hypotenuse of the right-angled triangle with the two hydraulic apertures as legs is given by the black dashed line. The hydraulic radius r_h (indicated by the solid red line) to approximate the radius of the pipe model is defined as half of the length of the hypotenuse.

into the generation procedure of the ECM instead of generating the grid cell conductivities in a stochastic manner (Hadgu et al., 2017). The accuracy of the ECM permeability prediction then depends on the resolution of the DFN-mapped continuum grid. Jackson et al. (2000) and Svensson (2001) already demonstrated that using cell sizes larger than the average fracture spacing of the network introduces artificial connectivity and hence overestimates effective permeabilities. Sufficient resolution of the continuum grid is therefore required to obtain comparable results with the DFN method (e.g., Botros et al., 2008; Leung et al., 2012).

To our knowledge, there is no approach to generate an ECM of a DFN that takes the effect of IFL (figure 4.1) into account. Thus, we will explain our new approach to generate continuum representations based on DFN structures - the fracture-and-pipe model.

Generally, the DFN approach offers a straightforward way to characterize structurally complex fracture networks. Most commonly, every fracture is modeled as a geometric primitive (here a disc) with a prescribed length l, center coordinate p_0 and unit normal vector $\bar{n}$ defining its orientation. Based on this, fracture intersections can be calculated to define the backbone of the network. Here, fracture intersections are approximated with a line defined by two points i_0 and i_1, whereas the unit vector $\bar{i}$ between the two points defines its orientation. The goal of the ECM method is to generate a 3D regular grid with constant x-y-z spacing δx, whereas every grid cell contains a symmetric, positive definite permeability tensor that is based on the fractures and their intersections.

To map each individual fracture to its corresponding grid cells, we first assume a horizontal

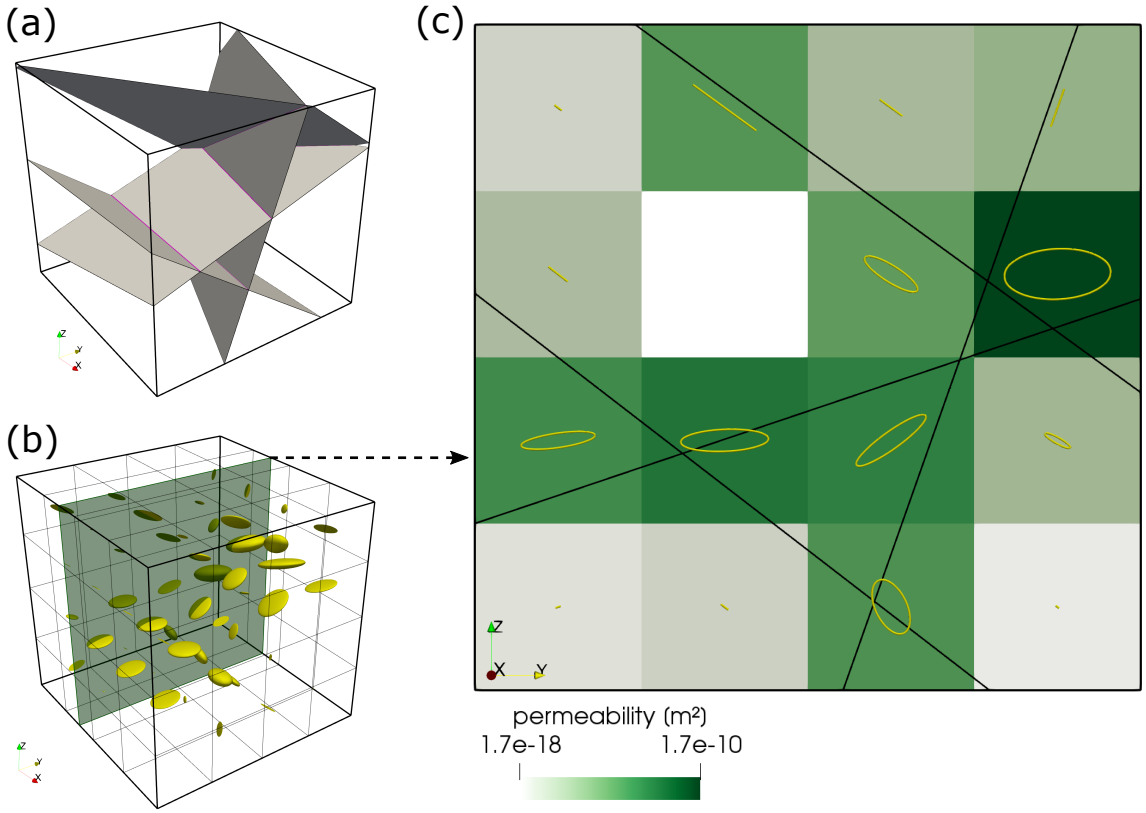

FIGURE 4.3: Workflow for generating an equivalent continuum model of a DFN. Panel *a* shows the input fracture network of 4 arbitrarily oriented fractures (gray) and their intersections (magenta). Panel *b* displays a grid of ellipsoids, each reflecting the shape of the permeability tensor in the equivalent continuum model of *a* with a resolution of 4^3 voxels. The size of the ellipses is scaled to the norm of the permeability tensor of the cell, such that larger ellipsoids denote higher permeabilities. The green plane in *b* indicates the location of the 2D slice displayed in *c*. There, different green-intensities present the norm of the permeability tensor of each cell. Black lines denote fractures in 2D and yellow ellipses the x- and y-shape of the permeability tensor of each cell. Note, how the shape of the ellipse changes from being planar, if multiple fractures cross a cell.

disc (normal vector $\bar{g} = [0,0,1]$) at center point $p_g = (0,0,0)$ with corresponding fracture radius r ($r = l/2$) and represent it with an equally spaced set of points in the x-y plane P_g, with the condition $||P_g - p_g)|| \leq r$. By that, we obtain a constantly spaced grid of points representing the fracture in horizontal orientation, provided that the initial equal spacing of the points δp is a small fraction of the cell size δx to prevent gaps in the mapped 3D grid. Next, we seek the rotation matrix R_f that aligns the current normal vector of the x-y plane $\bar{g} = [0,0,1]$ with the actual normal vector of the fracture $\bar{n}$. Utilizing Rodrigues's rotation formula (Rodrigues, 1840) around the rotation axis $w = (\bar{g} \times \bar{n})/||(\bar{g} \times \bar{n})||$ (unit vector orthogonal to $\bar{g}$ and $\bar{n}$) yields the rotation matrix R_f according to:

$$R_f = I + ||\bar{g} \times \bar{n}||\, C + (1 - \bar{g} \cdot \bar{n})\, C^2, \tag{4.10}$$

with $\times$, $\cdot$, and $||x||$ denoting the cross-product, dot-product and vector norm of x, respectively. I represents the 3-by-3 identity matrix and C the cross-product matrix of the rotation axis $w =$

$[w_x, w_y, w_z]$:

$$C = \begin{bmatrix} 0 & w_z & w_y \\ w_z & 0 & -w_x \\ -w_y & w_x & 0 \end{bmatrix}. \tag{4.11}$$

Following this, R_f is used to rotate the $3 \times n$ array of points representing the fracture plane P_g (n is the number of 3D points in P_g) around p_g and translate all points to the actual center point p_0 to produce a rotated set of points P_r representing the fracture in its actual 3D position:

$$P_r = P_g * R_f + p_0, \tag{4.12}$$

where $*$ denotes matrix-matrix multiplication. By ensuring that the lower left corner coordinate of the rectangular grids bounding box is initially located at $(0,0,0)$ (this may require a translation of all center points to incorporate all fractures), we obtain the grid-indices (i,j and k in x,y and z-direction, respectively) of the fracture by dividing P_r with the cell size δx and rounding the results. Finally, we compute the individual anisotropic permeability tensor K_{ijk} for the cells by using a parametrized fracture permeability value (eq. 4.7) and the rotation matrix R_f according to:

$$K_{ijk} = \frac{V_f}{V_c} k_f \left(R_f \begin{bmatrix} 1 & 0 & 0 \\ 0 & 1 & 0 \\ 0 & 0 & 0 \end{bmatrix} R_f' \right). \tag{4.13}$$

V_c denotes the cell volume (δx^3) and V_f the fracture volume per cell, which is approximated by counting the number of P_r points per individual cell, multiplying it with the squared initial point spacing δp and the hydraulic aperture a_h of the fracture. Obviously, the accuracy of V_f crucially depends on the initial point spacing of P_g - the finer the spacing, the better the approximation of V_f. Plot c in figure 4.4 shows that the condition $\delta p / \delta x \geq 16$ delivers sufficiently constant permeability values. In case multiple fractures transect the same cell, the permeability tensors are summed, similar to Chen et al. (1999) or Hadgu et al. (2017). However, these cells need additional treatment as they incorporate fracture intersections. To map all previously found intersections to the grid cells and formulate their permeability tensors, we follow the same workflow as presented for individual fractures. A horizontal line of the same length as the intersection ($||i_1 - i_0||$), parallel to the x-axis is represented by a constantly spaced set of points (similar spacing as in the case of a fracture, i.e. δp), whereas the mean point of the line is again located at $(0,0,0)$. We then calculate the rotation matrix R_i (eq. 4.10) by using $\bar{g} = [1,0,0]$ and $\bar{n} = (i_1 - i_0)/||i_1 - i_0||$. After identifying the corresponding grid i,j and k indices as described above, their permeability tensors are increased by using a parametrized interesection permeability (eq. 4.9):

$$K_{ijk} = K_{ijk} + \frac{V_i}{V_c} k_i \left(R_i \begin{bmatrix} 1 & 0 & 0 \\ 0 & 0 & 0 \\ 0 & 0 & 0 \end{bmatrix} R_i' \right). \tag{4.14}$$

V_i represents the intersection volume per cell, which we again approximate by counting the number of P_r points per cell and multiplying it with point spacing δp and the term πr_h^2, whereas

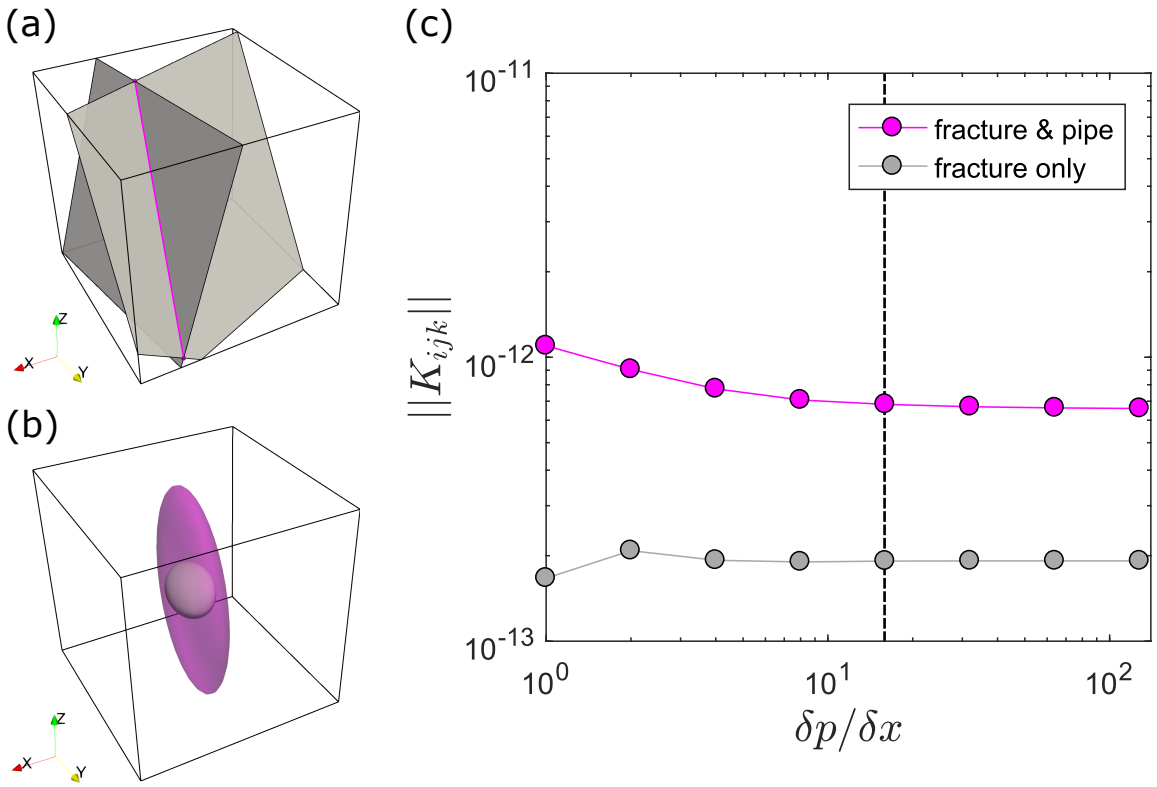

FIGURE 4.4: Fracture intersection caused changes of permeability tensor characteristics. Panel *a* shows a simple DFN structure of two arbitrary oriented fractures (grey) intersecting at a line (magenta). The cube length is set to 1 m and the system origin is at $(0, 0, 0)$. The center point of the first fracture is located at $(0.4899|0.5685|0.5110)$ and its normal vector is given as $(-0.3195, 0.7894, 0.524)$. The second fractures center point is located at $(0.7604|0.5000|0.5000)$, whereas its normal vector is given by $(-0.9461, 0.1715, 0.2747)$. Both fractures have the same hydraulic aperture of $1 \cdot 10^{-3}$ m and both fully penetrate the system. The resulting intersection ranges from point $(0.6499|0.3086|1.000)$ to $(0.8003|1.000|0.0505)$ and its orientation is given by the unit vector $(0.1270, 0.5839, -0.8018)$. The hydraulic pipe radius resulting from the half-hypotenuse assumption is $7.0711 \cdot 10^{-4}$. Panel *b* visualizes the shape of the permeability tensor for an ECM model that considers only fracture permeability (grey, inside) and for the presented fracture-and-pipe model (transparent magenta, outside). The size of both ellipses is scaled with the norm of the resulting permeability tensor to provide comparability. Panel *c* presents the norm of the permeability tensor K_{ijk} as a function of the ratio between initial point spacing δp and ECM grid spacing δx (see text for explanations). The dashed black line denotes the condition $\delta p/\delta x \geq 16$, that is used to provide an correct approximation of the fracture and intersection volume per cell.

r_h denotes the hydraulic radius of the pipe approximating the intersection. Figure 4.3 shows the resulting ECM structure with 4^3 cells of an arbitrary complex DFN, generated with the presented approach. For certain fracture systems (ideally no more than two fractures that fully penetrate the system, e.g., plot a) in figure 4.4), the presented approach derives an analytical solution for permeability by setting δx equal to the system size, resulting in a single permeability tensor for the whole system. Figure 4.4 demonstrates that incorporating the intersection as a pipe has a significant effect on the shape and absolute value of the permeability tensor at

intersections, which could cause an overall permeability increase by almost one order of magnitude. However, the exact amount of permeability increase depends on the chosen hydraulic pipe radius. The impact on the overall permeability at the network needs to be evaluated.

4.3.4 Continuum flow modelling

In the following, we will explain our method to obtain the effective permeability tensor of continuum cell representations for fractured-porous media. The governing equations for steady-state single-phase flow equations for an incompressible, isothermal and isoviscous fluid without sources and sinks are given im compact form by the following system of mass (eq. 4.15) and momentum (eq. 4.16) conservation equations:

$$\nabla \cdot q = 0, \tag{4.15}$$

$$q = -K\nabla P, \tag{4.16}$$

whereas ∇ and $\nabla\cdot$ denote the gradient and divergence operator for global 3D Cartesian coordinates, respectively. The specific discharge (flux) is given by q, pressure by P and the positive definite and symmetric hydraulic conductivity tensor by K according to:

$$K = \begin{bmatrix} k_{xx} & k_{yx} & k_{zx} \\ k_{yx} & k_{yy} & k_{zy} \\ k_{zx} & k_{zy} & k_{zz} \end{bmatrix} \frac{\rho g}{\mu}, \tag{4.17}$$

with the principal permeability tensor components k_{xx}, k_{yy} and k_{zz}, the off-diagonal components k_{yx}, k_{zx} and k_{zy} as well as fluid density ρ, gravitational acceleration g and fluid dynamic viscosity μ. We employ a 3D finite-element discretization scheme (e.g., Hughes, 1987; Zienkiewicz and Taylor, 2000; Belytschko et al., 2000; Lin et al., 2014) for equations 4.16 and 4.15 to simulate boundary driven pressure diffusion through any input grid consisting of unique permeability tensors. Using the Galerkin method (e.g., Belytschko et al., 2000; Lin et al., 2014), we transform equation 4.15 into an expression for the nodal residual R according to:

$$R = \int_V \nabla N^T K \nabla N dV P = 0. \tag{4.18}$$

V denotes the domain volume, N the nodal shape function matrix and P the nodal pressure. We use 8-node rectangular elements (voxels) with linear interpolation functions (e.g., Zienkiewicz and Taylor, 2000) for volume integral approximation, whereas element integrals are evaluated by Gauss-Legendre quadrature rule (e.g., Belytschko et al., 2000) over 8 integration points with parametric coordinates. Within each element, standard coordinate transformation is employed to compute shape function derivatives with respect to global coordinates ∇N:

$$\nabla N = J^{-1}\nabla_L N, \quad J = \nabla_L N x, \tag{4.19}$$

where ∇_L denotes gradient operator for local 3D element coordinates, J the Jacobian matrix and x the 3D global element coordinates. After imposing initial pressure conditions at the

boundary nodes, the global residual vector R_g is assembled from elemental contributions (e.g., Hughes, 1987) according to eq. 4.18 to solve the linear system of equations:

$$C_g P^{new} = R_g, \tag{4.20}$$

for the unknown pressure P^{new}. C_g denotes the global coefficient matrix, which is assembled from the nodal coefficient matrix C given by:

$$C = \int_V \nabla N^T K \nabla N dV. \tag{4.21}$$

Following this, we evaluate the nodal Darcy velocities u based on the newly solved nodal pressures by:

$$u = K \nabla N P^{new}, \tag{4.22}$$

whereas the velocity vectors on the nodes are averaged from the neighbouring integration points.

Three principal directions of the applied pressure gradient have to be considered to predict the full tensor of permeability. Thus, the flow simulation procedure repeats three times such that each principal flow direction (x-, y- and z-direction in a Cartesian coordinate system) is covered. For each iteration, we apply two constant pressure values at two opposing boundary

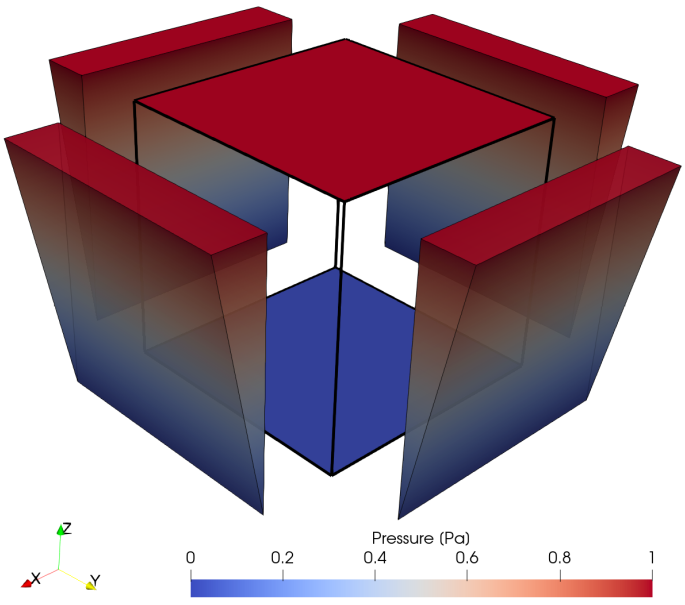

FIGURE 4.5: Pressure boundary conditions for an applied gradient in z-direction. Here, top and bottom faces experience constant pressures of 1 and 0 Pa, respectively. A linearly interpolated pressure distribution is applied at the remaining four boundary faces, as indicated by the colored wedges next to the side-faces of the model. Thus, the principal direction of flow is in z-direction, allowing to calculate the z-component related terms of the permeability tensor according to eq. 4.23

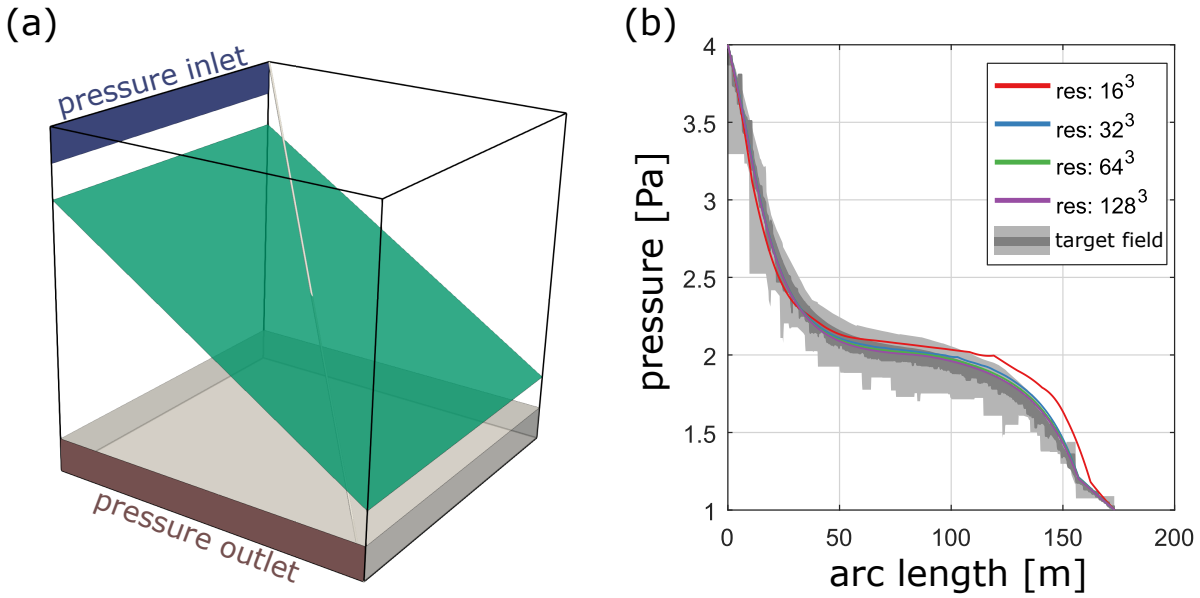

FIGURE 4.6: Benchmark case 1 from Berre et al. (2020). Panel *a* shows the benchmark geometry of an embedded fracture (aperture of 10^{-2} *m*) in a matrix with a hydraulic conductivity of 10^{-6}. The hydraulic conductivity in the grey band at the bottom is increased to 10^{-6}. Constant pressures of 4 *Pa* and 1 *Pa* are applied at the inlet band (blue) and outlet band (red), respectively. The diagonal light grey line through the model indicates the sampling line for the pressures shown plot in *b*. The pressure distribution is plotted as a function of arc length of the gray line in *a* and the results of different resolutions are compared to the benchmark target field obtained from 17 different numerical methods. The dark grey region illustrates the area between the 10th and 90th percentiles for the highest refinement level of the benchmarked methods, whereas the light grey region illustrates the same area for their lowest refinement level.

faces (e.g., lower and upper face in a cube for principal flow in z-direction) and the same linear interpolation between those two values at the remaining four boundary faces (see figure 4.5 for an example). This ensures to capture both, the diagonal and off-diagonal terms of the permeability tensor properly, which are computed by substituting the volume average $\bar{u}$ of all nodal velocity vectors u_I (see eq. 4.3) into Darcy's law for flow through porous media in the form of eq. 4.4. Figure 4.5 displays the situation of a vertically aligned pressure gradient ($\Delta P_z = \frac{\delta P}{\delta z}$). We compute the corresponding entries in the permeability tensor according to:

$$\begin{bmatrix} k_{zx} \\ k_{zy} \\ k_{zz} \end{bmatrix} = \frac{\mu}{\Delta P_z} \begin{bmatrix} \bar{u}_x \\ \bar{u}_y \\ \bar{u}_z \end{bmatrix}, \tag{4.23}$$

and vice versa for the iterations with pressure gradients in x- and y- direction to obtain the permeability tensor as shown in eq. 4.17.

The used single-continuum discretization scheme might appear simplistic compared to more sophisticated mesh-representations (see Berre et al., 2019). However, the merits of our approach rather lay (1) on a fully anisotropic permeability representation of the individual continuum cells and (2) massive parallelization and HPC optimization. Utilizing the parallelization

framework of PETSc (Balay et al., 2018) and their multigrid preconditioned solvers reduces the computational cost, allowing simulations routinely with 10^9 individual grid cells. An increase in grid resolution compensates the benefits of using conforming meshes or multi-continuum formulations Berre et al. (e.g., 2019). To test this, we compare our modeling procedure against benchmark case 1 from Berre et al. (2020), which compares 17 different methods of simulating single-phase flow in fractured porous media. The initial setup (displayed in a) in figure 4.6) consists of an inclined fracture with a hydraulic aperture of 10^{-2} m embedded in a cube of 100 m length with a matrix hydraulic conductivity of 10^{-6} m^2. The hydraulic conductivity of a small band of 10 m width at the bottom is increased to 10^{-5} m^2. We prescribe these two values as background permeabilities and use the methodology described in section 3.3.2 to incorporate fracture permeability accordingly. The boundary conditions are given by small pressure inlet (4 Pa) and outlet (1 Pa) bands as indicated in plot a in figure 4.6. The comparison of the pressure distribution (plot b in figure 4.6) highlights that already with a resolution of 32^3 voxels, and we obtain a good fit with the benchmark target field. This thus suggests that our modeling procedure is sufficiently correct for effective permeability predictions.

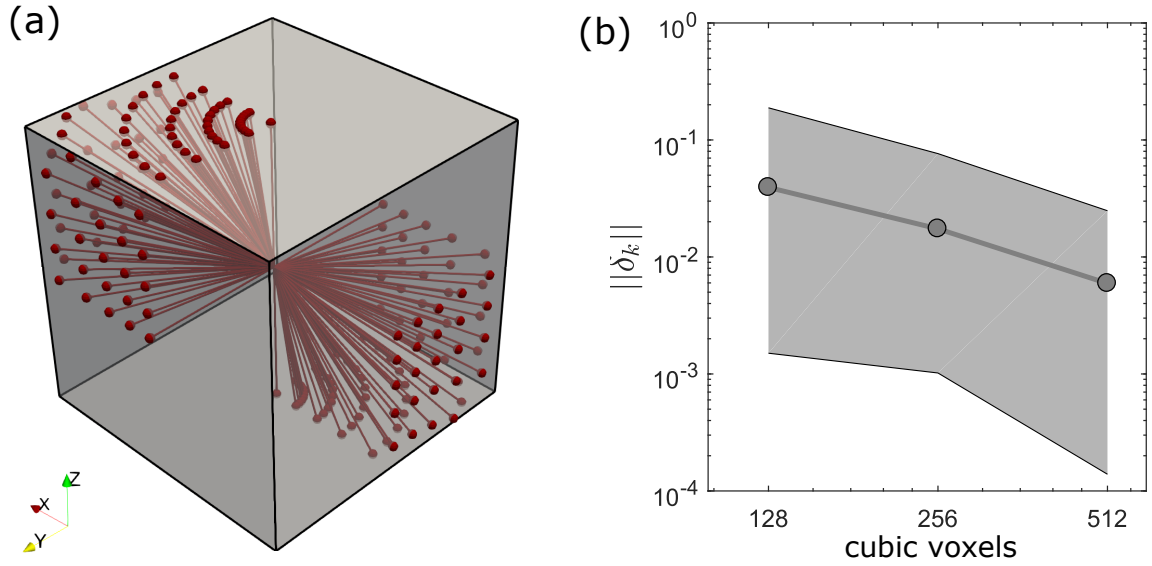

FIGURE 4.7: Panel *a* displays the location of all 100 intersection lineaments considered in the flow benchmark. 52 intersection configurations directly connect in- and outlets of flow (upper and lower z-face), whereas 48 connecting non-boundary flow faces. Panel *b* compares the numerically estimated permeability at highest resolution (1024^3 voxels) to the ones obtained at lower resolutions by calculating their error norms $||\delta_k||$ according to eq. 4.24. Gray dots represent the average error norm for all considered intersection configurations at resolutions lower than 1024^3 voxels. The light gray area highlights the range between minimum and maximum error.

4.4 Results

4.4.1 Intersection flow benchmark

To test the half-hypotenuse assumption (see figure 4.2 for details) as a first-order approximation for the hydraulic radius of the pipe, we conduct a benchmark study in the following. We calculate the directional permeabilities of simple fracture crossings with varying orientations from high-resolutions Stokes-flow simulations (e.g., section 2) and compare them to their analytically derived ECM single-cell counterparts (δx is equal to the full system size L) using the half-hypotenuse parametrization. For each intersection model, two fully persistent fractures with constant hydraulic apertures of 1.25 mm are placed in a cube of length 10 mm. Two fractures with a dip angle of 90 and dip directions separated by 90 (i.e., 90 and 180) are consecutively rotated counter-clockwise by increments of 10 around the center of the cube until we reach a total rotation of 90. We repeat this procedure nine times while consecutively reducing the dip angle of one of the two fractures by increments of 10 for each iteration. The dip angle of the remaining fracture is kept constant (i.e., 90) to maintain connectivity in the z-direction. This results in a total of 100 different intersection configurations (52 representing direct in- and outlets of flow, 48 connecting non-boundary flow faces), producing a wide variety of intersection orientations within two opposing octants in the cube (see figure 4.7 a for all generated intersection lineaments). For each configuration, we produce a binary voxel model (pore-space and matrix) of two crossing parallel plate fractures (similar to a) and d) in figure 4.1). Following the approach described in section 2, we apply different pressures at the bottom and top boundary to numerically estimate the directional permeability (setting the remaining boundaries to no-slip yields the vertical permeability component of the permeability tensor, k_z). We were systematically increasing the numerical resolutions of the Stokes-flow simulations (128^3, 256^3 , 512^3 and 1024^3 voxels) for each intersection configuration (resulting in a total of 400 HPC flow simulations) to determine whether the result at the highest level of detail represents a sufficiently converged solution. This is done by calculating the L2-error-norm $||\delta_k||$ according to:

$$||\delta_k|| = \left| \frac{k_x - k_{1024}}{k_{1024}} \right|, \tag{4.24}$$

whereas k_{1024} represents the directional permeability obtained at the highest resolution (i.e. 1024^3 voxels) and k_x the directional permeability from simulations with lower resolution (i.e., 128^3, 256^3 , 512^3 voxels). The resulting average error norms for all 100 intersection configurations are plotted in figure 4.7 b, which demonstrate the convergence towards the numerical result at the highest resolution. With an average error norm of about 0.6 % and a maximum error of 2.4 % for simulations with 512^3 voxels compared to the simulations at 1024^3 voxels, we assume that the solution at 1024^3 voxels represents a sufficiently accurate solution and can furthermore be used to benchmark the tensors generated with the ECM approach. Next, we follow the approach of section 3.3.3 to generate a single-cell permeability tensor of each intersection model, using a $\delta p / \delta x$ ratio of 16 and extract the vertical permeability component of the tensor (k_{zz}) and compare it with the one resulting from the Stokes-flow simulations. The results (figure 4.8) demonstrate that, if the intersection connects the two pressure boundary

faces (intersection-to-flow-direction angle $\gamma \leq 40$), the actual permeability obtained from the Stokes simulations is reasonably well reproduced with a small underestimation by the fracture-and-pipe model and heavily underestimated by the fracture-only approach (e.g., Hadgu et al., 2017). Using the half-hypotenuse assumption sufficiently integrates the effect of IFL at the scale of a continuum cell. Both models fail to predict the accurate directional permeabilities for intersections that connect no-pressure boundary faces ($\gamma > 40$), indicating that the effect of flow dispersion within the crossing fracture may play a more important role than previously thought. However, the cumulative error boxplot in figure 4.8 indicates that both methods give statistically acceptable predictions of the directional permeabilities (median error of 2.7 % for the fracture-and-pipe model and a median error of 7.9 % for the fracture-only model). Thus, the systematic error observed for $\gamma > 40$ appears negligible.

4.4.2 ECM based permeability upscaling of DFN's

So far, we presented a methodology to transfer a DFN into a regular grid of equivalent continuum cells and demonstrated its accuracy for simple fracture crossings at the scale of the continuum cells. This suggests that we can expect similar accuracy if we represent larger DFN's

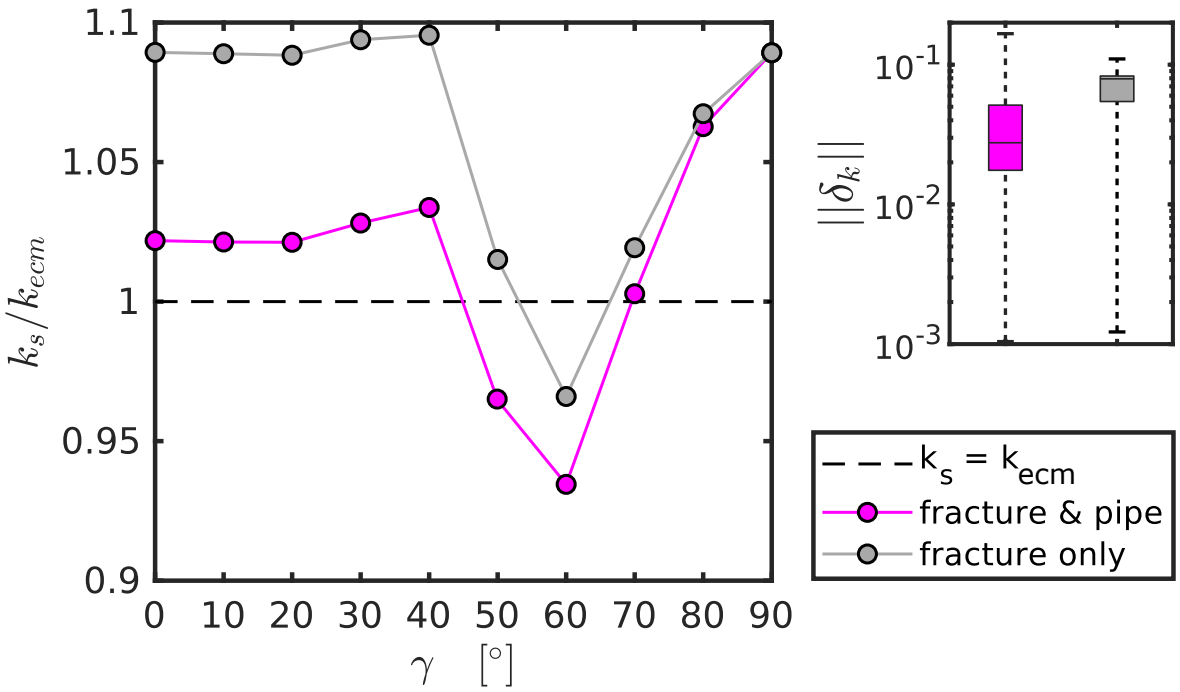

FIGURE 4.8: The left plot shows a comparison of directional permeabilities obtained from high-resolution Stokes-flow simulations (k_s) and analytically counterparts (k_{ecm}) derived with the ECM-approach described in the text as a function of the angle γ between the intersection and the principal flow direction. Magenta dots represent the mean permeability ratios (10 values per point) for the ECM approach described in section 3.3.3 with the half-hypotenuse pipe radius parametrization. Gray dots present the mean permeability ratio for an ECM approach that ignores the effect of intersections. The right plot shows a boxplot of the error norm $||\delta_k||$ computed according to eq. 4.24 with k_{ecm} as k_r for all 100 fracture-and-pipe (magenta) and fracture-only models (gray).

with complex structures by an equivalent continuum representation, provided that the grid resolution is sufficiently large to resolve the DFN in a similar way (i.e., a maximum of two fracture segments and one intersection per cell). As fracture networks typically have a multi-scale character with power-law or log-normal fracture size distributions (e.g., Bonnet et al., 2001; Davy et al., 2006), fulfilling that conditions require huge grid resolutions, making this method infeasible for practical applications. Predicting the effective permeability of the DFN by solving the groundwater flow equations (Darcy's law) would then require prior upscaling of the grid cell conductivities (e.g., Zhou et al., 2010; Hauge et al., 2012), depending on chosen flow solver and the available computational resources. However, averaging or flow-based upscaling

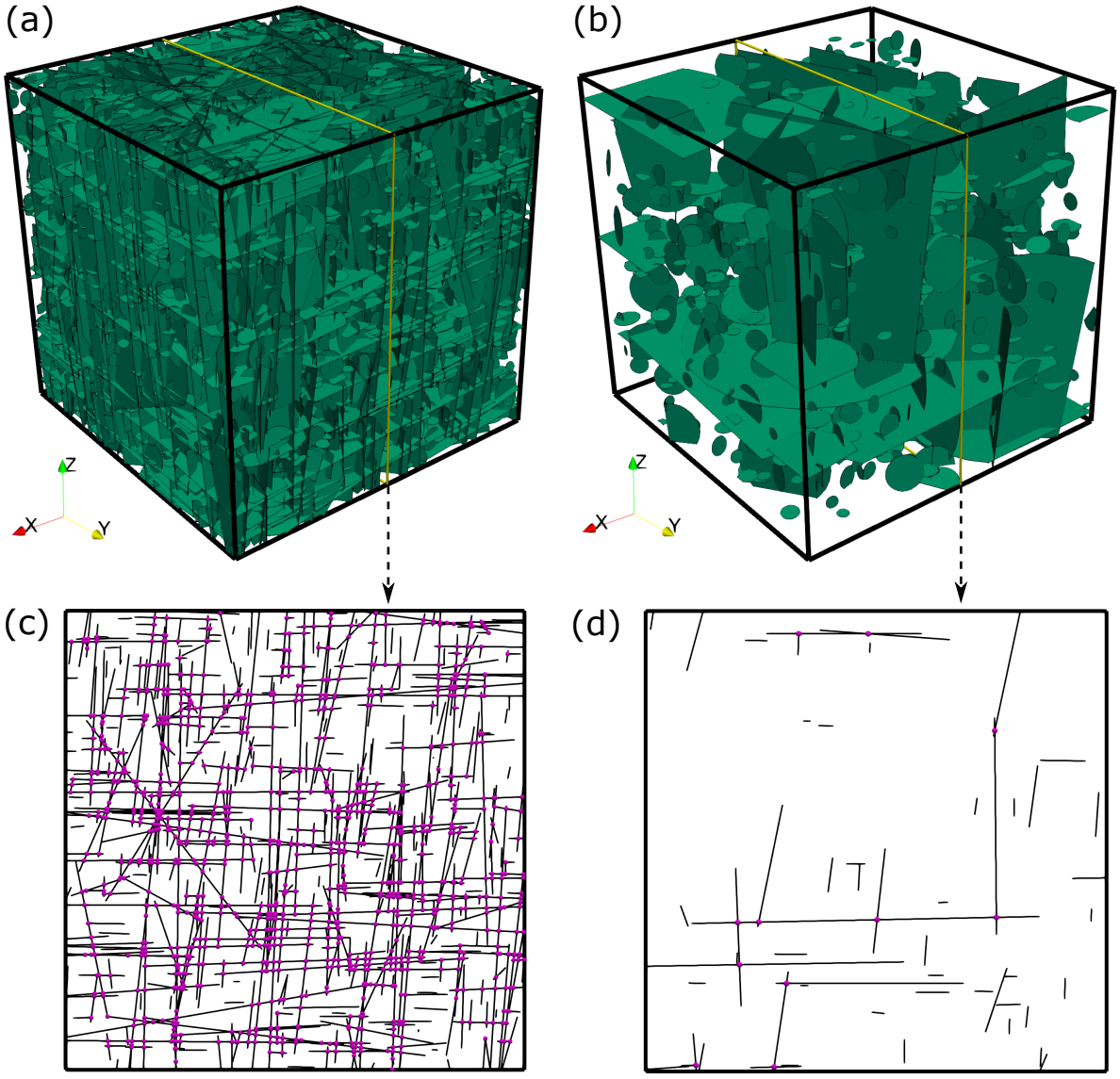

FIGURE 4.9: Panels *a* and *b* display the test DFN's with 10000 and 1000 fractures, respectively. Both are generated with the software ADFNE (Alghalandis, 2017), whereas input parameters are given in the text. Yellow lines depict the location of the slice shown in *c* and *d*. There, black lines indicate fractures and magenta spheres the location of fracture intersections.

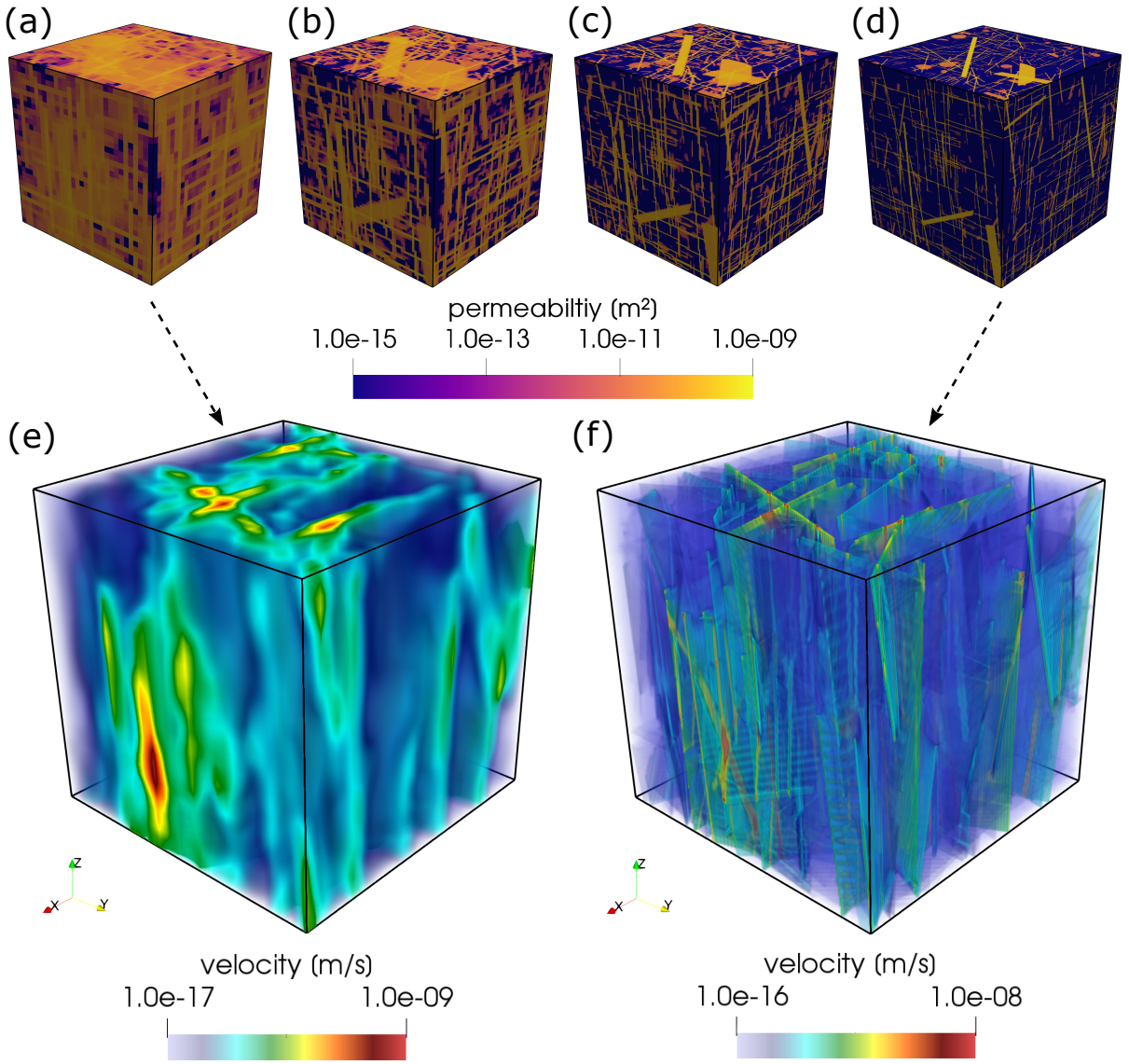

FIGURE 4.10: Panels *a*, *b*, *c* and *d* display the norm of the permeability tensor for each cell in an ECM representations of the 10000 fracture test DFN displayed in figure 4.9 a) for grid resolutions of 32^3, 64^3, 128^3 and 256^3 voxels, respectively. Panels *e* and *f* visualize the resulting velocity distribution for an applied pressure gradient in z-direction.

approaches may misrepresent network-scale flow characteristics, depending on the selected coarse-grid resolution. It is often unclear how the resolution dependency affects the accuracy of effective permeability computations and whether flow anisotropy is conserved. In the following, we will demonstrate that using ECM's of DFN's with sufficiently high resolutions is capable of doing precisely that while avoiding initial upscaling. For this, we compare effective permeability tensors obtained from the previously described massively parallelized continuum flow simulations for different DFN scenarios with varying resolutions of their equivalent continuum counterparts. We generate two test DFN's utilising the open-source MATLAB toolbox ADFNE (Alghalandis, 2017). Similar to Hadgu et al. (2017), the fractures in each DFN are separated into three orthogonal sets, reflecting naturally observed properties reported in SKB

(2010). $S1:\ 90|090$, $S2:\ 90|000$, $S3:\ 00|360$ give the mean dip-angle and dip-direction for the three fracture sets, respectively with a constant Fisher distribution concentration value of 5 accounting for variability around the mean. Fracture sizes l are distributed as a power law

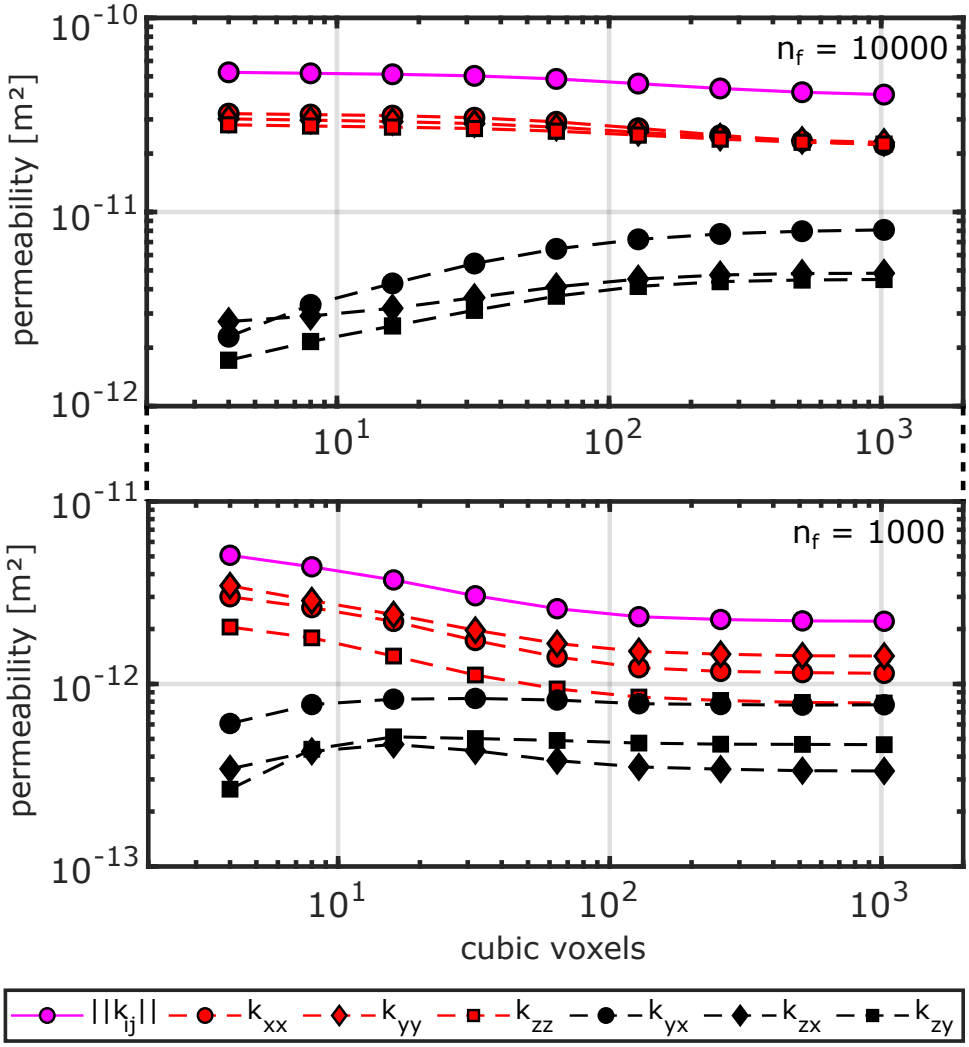

FIGURE 4.11: Absolute permeability values k for the 6 main components of the computed effective permeability tensor (principial components in red, off-diagonal components in black) and the norm of the permeability tensor in magenta as a function of the grid resolution in cubic voxels (number of voxels in x-y-z direction).

according to:

$$l = \left[\left(l_1^{\alpha+1} - l_0^{\alpha+1}\right) u + l_0^{\alpha+1}\right]^{1/\alpha+1}, \tag{4.25}$$

whereas l_1 is the upper cut-off length (500 m) and l_0 the lower cut-off length (15 m), u represents a set of uniformly distributed random numbers in the interval $(0, 1)$ and α the power law exponent (here $\alpha = -2.5$). All fracture centers are randomly placed in a cube with 500 m side lengths (the resulting DFN's are displayed in figure 4.9) with a background matrix permeability of 10^{-18} m^2. A sub-linear scaling of aperture versus length (e.g., Olson, 2003; Klimczak et al., 2010) is employed to correlate the hydraulic apertures a_h of the fractures to their lengths

l:

$$a_h = \beta \, l^{0.5}, \tag{4.26}$$

with a scaling factor β of 10^{-4}. The only difference between the two test DFN's is the overall fracture number, which is 10000 for the DFN-A (plot a in figure 4.9) and 1000 for the DFN-B (b in figure 4.9), such that we obtain a densely and sparsely fractured system, respectively. DFN-A thus represents the scenario of a typical REV network, according to Long et al. (1982) and Oda (1985). DFN-B, on the other hand, reflects a flow scenario closer to the percolation threshold with anisotropic, non-REV behavior (Maillot et al., 2016).
After calculating all fracture intersections with ADFNE's built-in function Intersect (see b and d in figure 4.9 for intersection spots in a 2D slice), we use the method presented in section 3.3.3, which incorporates the permeability parametrization concepts from section 3.3.2, to generate several ECM's with varying grid resolutions. Starting from 4^3 voxels and increasing by powers of two up to 1024^3 voxels yields 9 different continuum representations for each test DFN (see figure 4.10 for examples). For each representation, we compute the effective permeability tensor of the DFN by repeatedly solving the Darcy equations in three principal flow directions. The results are displayed in figure 4.11. For both test DFN's, the norm of the resulting effective permeability tensor ranges within the same order of magnitude. For DFN-A, we obtain a difference of about 30 % from coarse (4^3 voxels, $||k_{ij}|| = 5.24 * 10^{-11}$) to fine ($1024^3$ voxels, $||k_{ij}|| = 4.03 * 10^{-11}$) grid resolution, whereas DFN-B shows a larger difference of about 129 % (coarse $||k_{ij}|| = 5.07 \cdot 10^{-12}$, fine $||k_{ij}|| = 2.21 \cdot 10^{-12}$). Thus, the resolution dependence of the absolute permeability is small for fracture networks with an expected REV-behavior (DFN-A) and more pronounced for fracture networks with non-REV behavior (DFN-B). Interestingly, the individual components of the permeability tensor converge to constant values above resolutions of 128^3 voxels for both test cases, indicating that anisotropy magnitude depends on the level of detail of the ECM grid.

4.5 Discussion

Including a pipe-flow model into the ECM generation process improves the representation of permeability anisotropy therein and potentially impacts overall permeabilities. For example, at the scale of the intersection itself, it significantly modifies the shape and absolute values of the permeability tensor (figure 4.4). However, looking at the presented errors of the intersection benchmark (2.7 % and 7.9 % for the fracture-and-pipe and fracture-only model, respectively) indicates that, from a statistical perspective, the effect of IFL on overall permeability seems minor. Repeating the resolution test from section 3.4.2 with a fracture-only discretization approach for both test DFN's indeed resulted in almost identical permeability values (deviations of about 0.02 %). Thus, the effects of IFL seem to disappear at DFN sizes much larger than intersection size (mean hydraulic radius of approx. 0.7 mm versus 500 m system size in our case). This may be attributed to the fixed aperture-length correlation chosen for the test cases in this study. If, for example, two dominant fractures with larger apertures form an intersection that penetrates the whole system along the direction of flow, the effect of IFL might become

significant again due to the non-linear radius-permeability relation. Also, if small DFN's with sizes closer to the mean hydraulic radius of the intersections (e.g., micro-fracture networks) are considered for permeability prediction, IFL should play an important role. Then, however, additional factors have to be considered as well. For example, Dreuzy et al. (2012) have shown that fracture scale heterogeneity affects network scale connectivity due to flow channeling caused by closure in the aperture field. This may appear if the ECM cell size is similar to the internal correlation length of the fractures (e.g., Méheust and Schmittbuhl, 2003; Kottwitz et al., 2020) which would ultimately require new concepts to account for deviations from the average flow behavior instead of using fracture permeability parametrizations. A possible solution could be to introduce fracture permeability fluctuations if the ECM cell size is smaller than the individual fractures correlation length. Unfortunately, the scaling of the correlation length in fractures is poorly understood, so further research is required before integrating these effects. Additionally, the pipe parametrization we use as a first-order approximation for intersection permeability requires refinement to account for irregular shapes, tortuosity, or closure, representing another exciting question to solve in future studies.

For flow simulations at reservoir scales (similar to the test-cases considered here), the only computationally feasible solution is to use parametrization concepts (e.g., section 3.3.2). For that, we were able to demonstrate that the presented fracture-and-pipe ECM method can provide converged effective permeability tensors if the ECM resolution, i.e., the ratio of system size to discretization step size, is sufficiently large. This resolution dependency for 3D ECM's has not been reported at this level of detail so far but was expected based on previous works of Jackson et al. (2000) and Svensson (2001). Their main identified problem is artificially increased connectivity at lower resolutions, which occurs if the resolution is larger than either the average spacing of the fracture network or the minimal fracture length of the DFN, leading to overestimated permeabilities and misinterpreted anisotropy. Here, we use the average minimal distance of each fracture center to all other fracture centers in the network as a first-order approximation for fracture spacing. With an average spacing of $13.1 \pm 4.5\ m$, continuum grid resolutions above roughly 38 cubic voxels should theoretically start preventing artificial connectivity for DFN-A. For DFN-B, an approximated average spacing of $28.9 \pm 10.9\ m$, the required resolution to damp that effect is even lower (about 17 cubic voxels). Both test DFN's have the same lower cutoff fracture size of 15 m, so artificial connectivity should start decreasing above resolutions of about 33 cubic voxels. Looking at figure 4.11, we observe ongoing permeability convergence at these three mentioned resolutions. We attribute this to the fact that fractures are spaced randomly in space but sampled with a regular grid. Thus, the distance between fracture tips and continuum cell-edges might be larger for low resolutions, again causing permeability overestimations. Only above a resolution of 128 cubic voxels, all these effects seem to dampen out, allowing to declare the solution as sufficiently converged with quantitative errors below 10% for tensor norm and individual components. Hence, we suggest a general upper boundary of a third of the minimal fracture length l_0 as cell size for an ECM discretization of a DFN to provide consistent results.

Based on analytical solutions of flow in fracture networks with constant apertures, Svensson (2001) proposed that the ratio of ECM cell size to hydraulic aperture should not exceed two

to provide small flow errors. So far, the ratio of cell size to the minimal hydraulic aperture in the system was much larger (about 1260) due to the low scaling factor β of the sub-linear aperture to length correlation (eq. 4.26). To achieve similar discretization ratios of Svensson (2001) while maintaining a power-law size scaling, we would have to increase β to 10^{-1}, resulting in minimal and maximal apertures of 0.39 and 2.14 m, respectively. As this would violate the assumption of laminar flow conditions within the fractures, we cannot test their hypothesis and rather recommend staying above the maximum hydraulic aperture a_{h1} of the system, as otherwise the volume-fraction based permeability scaling factor in equations 4.13 and 4.14 exceed unity. In that case, parametrization assumptions might not hold anymore, preventing the use of continuum flow methods. However, as demonstrated here, sticking to $l_0/3 > \delta x > a_{h1}$ as condition for ECM discretization delivers constant effective permeabilities and conserves flow anisotropy for the upscaling. Within that discretization range, mapping a DFN onto an equivalent continuum grid can be used as a geometric upscaling procedure for further effective permeability analysis. Notably, this range strongly depends on the structural characteristics of the considered DFN, especially on the fracture size distribution and corresponding aperture correlation functions. For some DFN's this may require to crop the fracture size distributions from below to a few multiples of the cell size and compensate the hydraulic contribution of lower sized fractures with a background permeability.

4.6 Conclusion

This study analyzed the complexity of fracture intersection flow by conducting Stokes-flow simulations in simple fracture crossings. Intersections aligned with the pressure gradient cause an increase in permeability, as they act as a pipe. This results in intersection flow localization (IFL), i. e., intersections represent preferred pathways for the fluids compared to the connected fractures. We thus extended the state-of-the-art methodology to generate equivalent continuum models (ECM) for effective permeability computations of discrete fracture networks (DFN) to incorporate IFL effects. We integrate those with a directional pipe-flow parametrization with a hydraulic radius of half the hypotenuse size in a right-angled triangle with side lengths of both intersecting hydraulic apertures. By assessing the permeabilities of fracture intersections numerically, we could demonstrate that for system sizes close to the approximated pipe radius (typically mm to cm), the effect of IFL on permeability can be almost one order of magnitude. At larger scales (system size of several hundred m), on the other hand, the impact of IFL on overall flow is minor. There, the cell size with which the ECM is discretized represents the most crucial aspect for the accuracy of ECM-based effective permeability predictions. Based on a resolution test with two different DFN scenarios, we suggest that the ECM cell size should not be smaller than a third of the minimal fracture size and larger than the maximal hydraulic aperture of the system to conserve constant permeabilities and full anisotropy of flow. We conclude that ECM methods equivalently serve as geometric upscaling procedures for fluid flow problems within that range. Whether this holds for transport problems as well needs to be determined in future studies.

Chapter 5

Conclusion & Outlook [1]

5.1 Summary & Conclusions of this Thesis

The general goal of this thesis was to advance 3D numerical modeling of fluid flow in fractured reservoirs to provide accurate predictions of their hydraulic properties at scales covering the smallest micro-fracture up to the whole reservoir. Improving the accuracy and assessing the non-uniqueness of existing single fracture permeability prediction models was the first issue addressed in the scope of this thesis, as it is crucial to upscale fluid flow from fracture- to network scales and. Chapter 2 contributed a new scheme to quantify the vast heterogeneity of naturally occurring fracture morphologies with the help of only two non-dimensional parameters computed from the statistics of the fracture's aperture field and its individual surfaces. By computing effective permeabilities from numerical simulations of high-resolution 3D Stokes flow in an extensive data set of synthetically generated fractures covering a wide variety of statistical fracture configurations, we could derive a new, comparatively better parametrization model for fracture permeability. Quantifying the fracture wall roughness-induced geometrical deviations from the classical parallel-plate model yields a prediction of the average flow behavior for fracture populations with statistically similar geometries and provides the tool to parametrize the hydraulic effects of fluid-rock interactions or mechanical closure by a shift in parameter-space. Furthermore, we confirmed the seminal results of Méheust and Schmittbuhl (2003) by identifying the ratio between long-range aperture correlations and system length as the primary control on the non-uniqueness of permeability predictions and provided functional measures to integrate a variance model into network-scale flow models. The first part of chapter 3 demonstrated the applicability of this model on a data-set of 18 CT-imaged natural discontinuities, as the model originates solely from synthetic data. In the second part of the chapter, we have analyzed long-range aperture correlations in those 3D-imaged discontinuities, as this evidentially represents an essential but rarely reported property of natural fractures. Integrating these results with the few measurements reported in the literature showed that a linear relation to the fracture's mean aperture well approximates the length-scale of long-range aperture correlations. It also facilitates determining a minimal scale at which prescribing an average flow behavior of fractures in network-scale models is valid. There, imaging pore- and fracture-volumes for volumes larger than a few cubic decimeters on a CT-like level of detail is

[1] The outlook part of this chapter is based on the results of the PERMEA project and involves scientific contributions from Kottwitz, M. O., Popov, A. A., and Kaus, B. J. P., Deckert, H., Abe, S., Costa, A., Schmatz, J., Klaver, J., Bauer, W. and Freitag, S.

impossible due to top-end spatial limitations of imaging techniques. Thus, modeling fluid flow in network-scale models requires upscaling both the initial hydraulic structure (via permeability parametrizations) and the governing equations (i.e., from finite-difference Stokes to finite-element Darcy approximations of the fluxes). Chapter 4 provides a computationally efficient framework to predict effective permeability tensors of fracture networks, modeled by discrete reduced-order models such as the discrete fracture network (DFN) method. For this, we started with performing 3D Stokes flow simulations in a bunch of idealistic fracture-intersection models (two parallel plates fractures crossing each other) to (1) demonstrate the process of intersection flow localization (IFL) and (2) work out a parametrization to incorporate these observations into network-scale continuum models. The numerical simulations showed that fracture intersections represent preferred pathways for fluid migration and enhance the overall permeability of the system if its orientation aligns with the applied pressure gradient and its length is of similar size as the system. A directional pipe-flow parametrization well-approximates these hydraulic effects if the hydraulic radius of the pipe has half the length of the hypotenuse in a right-angled triangle with side lengths of both intersecting hydraulic apertures. As a next step, we provided a methodology to generate equivalent continuum models (ECM) from any input DFN as the basis to perform flow-based upscaling (i.e., computing the effective permeability tensor of the system from 3D Darcy flow simulations). For this, we subdivide a DFN into a 3D regular grid of voxel elements, where each has an individual anisotropic permeability tensor based on fractures and intersections crossing the cell. We used this methodology to assess the effective permeabilities of two kilometer-scale test DFN's with ECM's of varying resolutions. Seemingly, IFL affects the effective permeabilities of a fracture system only when a prominent intersection penetrates the whole domain. Yet, the resolution test demonstrated how the resolution dependency of ECM methods biases upscaling accuracy. We concluded that the ECM cell size should not be smaller than a third of the minimal fracture size and larger than the maximal hydraulic aperture of the system to produce converged effective permeability estimates and conserve their anisotropy. Within this range, we argue that the ECM method serves as an accurate and cost-efficient tool to upscale the hydraulic properties of fracture networks while providing the possibility to incorporate matrix hydraulics.

The compiled results of this thesis enhanced the accuracy of multi-scale modeling of fluid flow in fractured reservoirs. Improving current and deriving new parametrizations for complex flow patterns at small scales benefited the integration of those hydraulic effects to larger scales. There, examining the resolution dependency of continuum methods optimized the trade-off between (1) having an efficient numerical method to model fluid flow while (2) properly capturing the multi-scale character of a fractured reservoir as it allows to determine the minimal scale at which reduced-order models like the DFN or ECM method for permeability predictions is statistically valid. Thus, analyzing the variance of hydraulic network properties induced by limited knowledge of reservoir structure in a stochastic manner should benefit the most from these findings. The work conducted in this thesis thus delivers the framework to provide properly upscaled intrinsic permeabilities of multi-scale structures for more sophisticated, multi-physics (i.e., mechanically and/or thermally coupled) simulations in reservoir engineering.

The straightforward scientific extension of this thesis is to apply and validate the developed multi-scale methods on a naturally existing fractured reservoir targeted for subsurface resource utilization. The following section gives an outlook on planned studies from a current research project that targets this.

5.2 Outlook: Insights from the PERMEA project

Understanding the hydraulic complexity of naturally fractured and faulted upper crustal zones is a key asset of subsurface resource utilization. Especially for carbonate rocks, multi-scale characteristics occur from the nanometer- to reservoir-scale (Goldscheider et al., 2010; Hardebol et al., 2015; Volatili et al., 2019). If the rock matrix is considered impermeable, the vast majority of fluids migrate through open discontinuities (for simplicity, further referred to as fractures). In conceptual fault models, fractures arrange in networks with increasing fracture densities in regions close to the fault (so-called damage zones) (Evans et al., 1997; Faulkner et al., 2010). While damage zones may be highly transmissive features of fault zones, the fault core is thought to act as a hydraulic barrier due to the sealing properties of the ground particles in fault gouges (e.g., Morrow et al., 1984). Due to the diversity of tectonic mechanisms that produce faults in the upper crust (Pollard and Aydin, 1988; Wibberley et al., 2008; Vrolijk et al., 2016), the structure of damage zones and fault cores can be highly heterogeneous, which translates to non-stationary and anisotropic hydraulic properties, both spatially and temporally (Aydin, 2000; Faulkner et al., 2010). A recently published summary paper considering numerous multi-scale hydraulic assessments of fault zones illustrates this (Scibek, 2020). Since seismic surveys cannot image individual fractures or fault zone features below a couple of tens of meters, acquiring detailed reservoir data is intricate and limited to direct observations of outcrops, sample measurements, drill cores, and borehole imaging (Xu and Dowd, 2010; Lei et al., 2017). Thus, stochastic methods to extrapolate the data are required to complement field measurements while ensuring proper integration of detailed reservoir data into numerical simulations of fluid flow represents a vital opportunity to improve the uncertainty of hydraulic reservoir assessments.
For reservoirs with fracture-dominant flow, the usual approach is to measure fracture length-, orientation- and density distributions (Dershowitz and Einstein, 1988), which serve as input data for stochastic modeling approaches like the discrete fracture network method (DFN) (Cacas et al., 1990; Bogdanov et al., 2003; Darcel et al., 2003). There, fractures are either placed randomly (Hyman et al., 2015; Maillot et al., 2016; Alghalandis, 2017; Lavoine et al., 2019) or mechanically constrained (Davy et al., 2013; Bonneau et al., 2016; Maillot et al., 2016) in a 3D medium to generate several 3D realizations of fracture networks reflecting naturally observed properties. The pressure drop through an individual fracture then represents the primary controlling factor of the reservoir hydraulics and strongly depends on its aperture-field statistics and surface characteristics (Zimmerman and Bodvarsson, 1996; Foroughi et al., 2018; Mourzenko et al., 2018). Quantifying the deviations from the parallel plates model (Lomize, 1951; Snow, 1969; Witherspoon et al., 1980) as a function of the fractures geometry allows to predict the intrinsic permeability of fractures (Patir and Cheng, 1978; Brown, 1987; Renshaw, 1995)

from numerical simulations of fluid flow. However, the accuracy of that prediction strongly depends on the ratio between the correlation length of the aperture field and the considered scale (Méheust and Schmittbuhl, 2003). Flow characteristics at scales below the correlation length are highly variable and anisotropic due to flow-channeling, -clogging, or -enhancement induced by local aperture variations (Méheust and Schmittbuhl, 2000; Méheust and Schmittbuhl, 2001). These effects dampen out if fracture scales much larger than the aperture correlation length are considered. There, it is possible to define an average flow behavior of fractures with similar geometrical characteristics (e.g., Méheust and Schmittbuhl, 2003; Kottwitz et al., 2020), allowing for easy integration of individual fracture flow characteristics into fracture network flow models by using a corrected parallel plate model. Various numerical techniques (e.g., Jing, 2003; Berre et al., 2019) can be applied to simulate network scale flow with the single-phase Darcy equation, either in a discretized version of the DFN itself or in a continuum representation thereof (Reeves et al., 2008; Hadgu et al., 2017; Sweeney et al., 2020). For the latter, the grid resolution has to be sufficiently high to capture complex and anisotropic network flow patterns (e.g., Svensson, 2001; Kottwitz et al., 2021). However, both of them rely on the modified parallel plate assumption to prescribe fracture hydraulics. Dreuzy et al. (2012) have shown that local aperture variations affect network scale flow if the total system size is close to the aperture correlation length. For kilometer-scale networks, Makedonska et al., 2016 have shown that aperture variations have negligible effects on network flow and transport properties. Thus, an analysis of the correlation length in naturally occurring fractures is required to determine the validity of the modified parallel plate assumption in network flow models.

Combining reservoir information assessed in field campaigns (structural mapping and sampling, UAV-based outcrop evaluation) with laboratory experiments (μCT-scans, petro-physical measurements) and numerical models of fluid flow represents an opportunity to get quantitative insights on reservoir complexity and subsequent permeability predictions. In the scope of the German federal ministry of education and research (BMBF) funded project PERMEA (grant no. 03G0865A), a quarry of densely fractured tight carbonate rocks serves as a natural laboratory for structural and hydraulic data acquisition. Integrating this information into numerical simulations of fluid flow to compute and upscale reservoir permeabilities is a key target of this study. For that, we utilize numerical methods to simulate direct (Stokes) and continuum (Darcy) flow in fractured-porous media at resolutions that allow integrating real data covering multiple orders of magnitude in size scaling. Typically, direct flow simulations require 3D representations of segmented pore-space and rock matrix obtained from imaging techniques (e.g, Cnudde and Boone, 2013; Andrä et al., 2013a). The resulting voxel models serve as input geometries for laminar Stokes flow simulations and subsequent permeability predictions (Osorno et al., 2015; Eichheimer et al., 2019; Eichheimer et al., 2020). They become infeasible for larger scales due to the lack of imaged data and high computational cost. Continuum flow simulations allow the upscaling of flow properties over a regular grid of control volumes with individual permeability tensors by solving the Darcy equations for prescribed pressure boundary conditions. Initial knowledge of the intrinsic permeability structure of the medium is required and can be obtained from experimental measurements (Dastidar et al., 2007), direct flow simulations (Andrä et al., 2013b) and analytical models (Patir and Cheng, 1978; Brown,

1987; Renshaw, 1995; Zimmerman and Bodvarsson, 1996; Kottwitz et al., 2020).
This study will propose a data-oriented multi-scale strategy for fluid flow simulations in fractured porous media for a numerical assessment of damage zone permeability. On the micro-scale (micrometer to a few centimeters), we utilize μCT-scans of various types of fractures, or 3D fault zone features that are sampled from the test side to (1) analyze the statistics of the fractures individual surfaces and aperture field, (2) numerically compute their intrinsic permeabilities, compare to existing parametrizations and (3) determine the aperture correlation length to legitimize the usage of parametrization concepts for fracture permeability in fracture network flow models. On the macro scale (centimeter to a couple of hundreds of meters), we employ classical field mapping and digital fracture analysis on image-based 3D photogrammetry outcrop models (Nesbit et al., 2018; Akara et al., 2020) to quantify fracture length- and orientation-distributions as well as fracture densities for the test site. We generate stochastic DFN models that extrapolate the deterministically mapped fracture properties on outcrop surfaces to 3D with this data. The DFN's are transferred into equivalent continuum models (ECM, e.g., Leung et al., 2012) with a recently developed technique accounting for flow-localization in fracture networks (see Kottwitz et al., 2021) to compute their effective permeabilities. After successfully validating the multi-scale flow simulation methodology with analog flow-through experiments through 3D-printed fracture networks, we explore the effects of individual fracture morphology on damage zone permeability in a numerical parameter study.

5.2.1 Test site description

The Upper Jurassic (Malm) aquifer is a frequent target for geothermal energy production in the southern German Molasse Basin area (Cacace et al., 2013; Homuth et al., 2014; Przybycin et al., 2017). The fracture-dominant formation is outcropping in an active limestone quarry near Ittling in the Franconian Alb, which serves as a test site for structural and hydraulic data acquisition for this study. There, a horizontally layered formation of limestones has been subject to multiple faulting events resulting in a dominant WNW-ESE striking moderately steep (60-80 $^\circ$ dipping to NNE or SSW) conjugate normal fault system and a few NNE-SSW striking conjugate faults steeply dipping ($\sim$80 $^\circ$) towards WNW or ESE. Correlating layers in fault-juxtaposed blocks for both fault sets indicate very low to unrecognizable amounts of slip. Intensive fracturing (joints, calcite veins, and stylolites) is observed throughout the whole quarry and distinguished in two sets that follow similar orientations as the fault systems, i. e., a NNE-SSW and a WNW-ESE striking non-layer-bound joint set, both steeply dipping (80-90 $^\circ$). Stylolites predominantly follow WNW-ESE striking orientations, similar to the latter joint set. Several core plugs were sampled from consecutive layers on an outcrop wall to conduct petro-physical measurements of the rock matrix. Wood's metal injection (WMI), mercury intrusion porosimetry (MIP), and BIB-SEM imaging (following the methodology of Klaver et al., 2015) indicate locally connected moldic pores and vugs (pore diameters between 0.1 and 1 μm, pore throats from 0.008 to 0.04 μm) with homogeneous porosities of $\sim$5 %. Gas permeability measurements conducted in a Hassler-cell (e.g., Filomena et al., 2014) reveal average matrix permeabilities of $1.22 \cdot 10^{-17} \pm 4.98 \cdot 10^{-18} m^2$ with no notable influence of local stylolites. Performing several

pumping tests in 9 drilled, 16-22 meter deep wells within a small subregion of the quarry enabled to relate hydraulic parameters according to the techniques of Cooper and Jacob (1946) and Dupuit (1863). Effective permeabilities range between $2.13 \cdot 10^{-15}$ and $8.02 \cdot 10^{-11}$ m^2 with a mean of $2.58 \cdot 10^{-13} m^2$, whereas 50 % of the measurements fall into a narrower range between $2.07 \cdot 10^{-13}$ and $3.87 \cdot 10^{-13}$ m^2. Local transmissivity fluctuations were thought to be caused by the presence or absence of fractures, identified in well-imaging logs (e.g., Serra and Serra, 2004; Shalaby and Islam, 2017). By utilizing fracture frequency and permeability measures for each well, we related an average hydraulic aperture of 0.186 ± 0.019 mm according to the formula presented in Klimczak et al. (2010). Generally, the relative increase of rock matrix to bulk network permeability measurements indicates fracture-dominant flow, which justifies using the DFN method and related fluid flow modeling techniques to complement and extend the hydraulic assessment of the reservoir.

5.2.2 Digital fracture mapping from photogrammetry models

Structure-from-motion (SFM) photogrammetry represents a cost-efficient tool to obtain georeferenced 3D models of natural objects (Westoby et al., 2012). Numerical analysis of the digital models can be applied to obtain surface measurements of discontinuities (e.g., Baker et al., 2008; Poropat, 2009; Renard and Candela, 2017) or bulk fracture data (e.g., Olariu et al., 2008; Nesbit et al., 2018; Akara et al., 2020). Here, we employ Agisoft Metashape (https://www.agisoft.com/) to generate a 3D outcrop model from high-resolution camera and unmanned aerial vehicle (UAV) images of the test site. Next, we apply a digital mapping routine on visible fractures from the outcrop model to obtain 3D fracture data. For that, we utilize the "PointPicker" tool within the VTK-toolbox (Schroeder et al., 2006) to digitize points on each visible individual fracture trace or plane from the 3D outcrop surface. A fitting routine is applied to all digitized points per fracture to obtain a center point and a mean plane reflecting its orientation. Next, we compute the fracture length by projecting all digitized points onto their mean plane and finding the two that are the furthest away from each other. With this information, we generate a disk that approximates the fractures orientation, location, and length in 3D, which is a common practice in DFN modeling (e.g., Hyman et al., 2015). Repeating this digital mapping procedure for all visible fractures on the outcrop model enables to compute bulk fracture length- and orientation distributions easily. To obtain estimates of fracture spacing and volumetric densities, the most common approach is to conduct classical 1D scan-line surveys (e.g., Priest and Hudson, 1981). Here, we perform those surveys digitally by prescribing a scan-lines start and endpoint on the digital outcrop model and calculating its intersection points with the digitized fracture discs. From this, we can directly infer the P_{11} fracture intensity measure of Dershowitz and Herda (1992) for certain scan-line lengths. If fracture orientations follow Fisher distributions (Fisher et al., 1987), i. e.:

$$f(\alpha) = \frac{\kappa e^{\kappa \cos \alpha} \sin \alpha}{e^{\kappa} - e^{-\kappa}}, \tag{5.1}$$

with α being the angle between a fracture normal and the mean pole of a fracture set and κ the fisher concentration parameter ($\kappa = 0$ indicates a uniform distribution and larger κ values

denote increasing concentration around the mean orientation), we can directly relate the 3D intensity measure P_{32} (e. g., Dershowitz and Herda, 1992) with the conversion factors provided by Wang (2005). By calculating the auto-correlation function of P_{11} for different lengths along the scan-line, we can obtain directional correlation lengths of fracture intensity. By this, we estimate the amount of spatial correlation while generating the stochastic 3D DFN models of the damage zone used for effective permeability predictions.

5.2.3 DFN modeling of damage zone and equivalent permeability estimation

Due to a lack of volumetric fracture data, extrapolation of the outcrop-based data is necessary to assess the permeabilities of the reservoir numerically. Here, DFN modeling is conducted with the open-source Matlab toolbox ADFNE (Alghalandis, 2017) to generate stochastic realizations of 3D fracture networks that reflect the statistical properties obtained from a digital mapping of the test-site. The integration of macro (orientation- and length-distribution, fracture intensity) and micro-scale (fracture permeability, aperture correlation length) fracture data into the generation of stochastic DFN's is described in the following. As shown in the previous section, the fracture radii and orientations for both identified sets result from digital mapping, and prescribing both for generating DFN's with randomly distributed fracture centers is straightforward (e. g., Long et al., 1985; Cacas et al., 1990; Berkowitz, 2002; De Dreuzy et al., 2002; Lei et al., 2017; Smeraglia et al., 2021). However, spatial correlation of fracture positions is thought to be the direct consequence of mechanical behavior of rocks during brittle deformation (Pollard and Aydin, 1988; Olson, 1993). Additionally, it affects the connectivity of fracture networks and their effective properties (Bonneau et al., 2016; Davy et al., 2018). Thus, prescribing spatial correlation within stochastically generated DFN's is vital to reflect the networks' structure in flow simulations. As explained above, directional correlation lengths result from the auto-correlation analysis of 1D scan-line measurements. Those estimates serve as input for algorithms that produce spatially correlated random fields, frequently used in geophysical applications (see Räss et al., 2019). Based on these 3D random fields (here called nucleation fields, NF), we constrain the location of fracture centers while generating the DFN. Each voxel in the 3D NF possesses a scalar value drawn from the standard normal distribution with a prescribed standard deviation. After rounding and setting negative values to zero, we loop over all elements in the NF and generate n_v randomly distributed fracture centers within the bounding coordinates of the current voxel, whereas n_v is its scalar value. All fracture centers generated by this procedure are stored in a point-list of length n_t, from which a random subset of length n_f is drawn in the DFN generation procedure to prescribe the spatial position of all fractures. Note that the ratio of n_f to n_t shouldn't be smaller than $1/32$ to assure that the enforced spatial correlation does not vanish by under-sampling. Furthermore, the chosen size, resolution, and standard deviation of the initial NF should result in a reasonable amount of fracture centers per voxel compared to estimates obtained from fracture intensity measurements. The total number of fractures (n_f) for both determined sets to insert into the 3D volume is again inferred from the 1D virtual scan-line measurements as follows:
The average P_{11} value (e. g., Dershowitz and Herda, 1992) for a scan-line length that corresponds to the fracture intensity correlation length is calculated. Next, its 3D counterpart is

related for each set according to

$$P_{32} = C_{13} \times P_{11}, \tag{5.2}$$

whereas C_{13} is the conversion factor reported by Wang (2005) for a certain angle between scan-line- and mean fracture-orientation and the fisher dispersion parameter κ. The total number of fractures per unit volume (P_{31} in Dershowitz and Herda, 1992) can be related by:

$$P_{31} = \frac{P_{32}}{\bar{A}}, \tag{5.3}$$

with $\bar{A}$ being the integral of the fracture area distribution $f(A)$ according to:

$$\bar{A} = \int_{A_{min}}^{A_{max}} A f(A) dA, \tag{5.4}$$

with fracture area related to its radius r by $A = \pi * r^2$. Thus, the total number of fractures to be inserted n_f within a certain volume V can be referred by:

$$n_f = P_{31} * V. \tag{5.5}$$

As there is no individual information on fracture aperture, but rather an average estimate from the test site pumping tests ($\bar{a}_{exp} = 0.186 \pm 0.019\ mm$) and the measured values from the μ-CT-scans (see table 3.1, $1 \geq a \geq 6 \times 10^{-4} m$), we utilize a sub-linear scaling function to infer mean apertures $\bar{a}$ from length L of the individual fractures as suggested by Olson (2003) or Klimczak et al. (2010):

$$\bar{a} = \beta L^{0.5}. \tag{5.6}$$

The prefactor β is chosen, such that eq. 5.6 produces the pumping-test determined average aperture $\bar{a}_{exp}$ assuming a mean fracture length $\bar{L}$ obtained from the measured size distribution (either log-normal or power-law), i. e.:

$$\beta = \frac{\bar{a}_{exp}}{\sqrt{\bar{L}}}. \tag{5.7}$$

After generating a statistically constrained random DFN realization with ADFNE (Alghalandis, 2017) and calculating all fracture intersections with its built-in function "Intersect", it is transferred into an equivalent continuum model (ECM) according to the method described in Kottwitz et al. (2021), which is an extension of the works of Oda (1985), Chen et al. (1999) and Hadgu et al. (2017). There, the DFN is subdivided into a regular grid of voxels and their permeability tensors are prescribed analytically. For each fracture or fracture intersection, we identify the corresponding grid voxels and add the symmetric permeability tensors K (subscript f for fractures, i for intersections) to the respective voxels according to:

$$K_f = \frac{V_f}{V_c} k_f \left(R_f \begin{bmatrix} 1 & 0 & 0 \\ 0 & 1 & 0 \\ 0 & 0 & 0 \end{bmatrix} R'_f \right). \tag{5.8}$$

or

$$K_i = \frac{V_i}{V_c} k_i \left(R_i \begin{bmatrix} 1 & 0 & 0 \\ 0 & 0 & 0 \\ 0 & 0 & 0 \end{bmatrix} R_i' \right). \tag{5.9}$$

with V_f and V_i denoting the volumes of fracture and intersection per cell, respectively, and V_c the voxel volume. R_f and R_i represent rotation matrices, accounting for the alignment of the analytical permeability tensor with the orientation of the fracture or intersection itself, which can be found with the help of Rodrigues's rotation formula (Rodrigues, 1840). The parametrized permeabilities for fractures and intersections are given by k_f and k_i, respectively. Fracture permeability is prescribed with a modified cubic-law according to the model of Kottwitz et al. (2020), i. e.:

$$k_f = \chi \frac{\bar{a}^2}{12}. \tag{5.10}$$

The mean aperture is given by $\bar{a}$ (see eq. 2.9), χ represents the hydraulic efficiency according to Kottwitz et al. (2020), which itself is a function of the fractures relative closure and effective surface area. Kottwitz et al. (2021) have demonstrated the effect of intersection-flow-localisation (IFL), resulting in an increase of overall permeability if the intersection is aligned with the applied pressure gradient. They have also shown, that the hydraulics of idealized fracture intersections (simple x-crossings) are approximately pipe-like and can thus be approximated by:

$$k_f = \frac{r_h^2}{8}, \tag{5.11}$$

whereas r_h denotes the pipe radius computed from the intersecting hydraulic apertures a_{h1} and a_{h2} according to:

$$r_h = \frac{\sqrt{a_{h1}^2 + a_{h2}^2}}{2}. \tag{5.12}$$

However, the resolution of ECM models for permeability predictions has to be chosen carefully. Applying too low resolutions (large voxel-sizes) can introduce artificial connectivity (e. g., Jackson et al., 2000; Svensson, 2001) biasing flow computations. Applying too high resolutions (small voxel-sizes) instead produces either anti-physical volumetric permeability scaling ratios (i.e., above unity if the voxel-size is below the hydraulic aperture of a fracture) or interferes with the assumption of prescribing an average fracture flow behavior with a modified parallel plates assumption (i.e., if the ratio between aperture correlation length and voxel-size is larger than 1/16). Depending on the fracture network properties, the range of applicable ECM grid resolutions may be limited and needs to be determined individually (Kottwitz et al., 2021), as otherwise fracture-scale heterogeneity may affect network scale flow as pointed out by Dreuzy et al. (2012). They prescribe constant aperture correlation lengths for each fracture in the system, regardless of its length or aperture. However, looking at the in-situ determined aperture correlation lengths for this study (see table 3.2) suggest that their values range in the order of the fractures mean apertures (average $l_c/\bar{a}$ ratio of $\sim$1.5). Following the results of Ogilvie et al. (2006), Watanabe et al. (2008), and Zambrano et al. (2019), the aperture correlation length mainly depends on shear displacement.

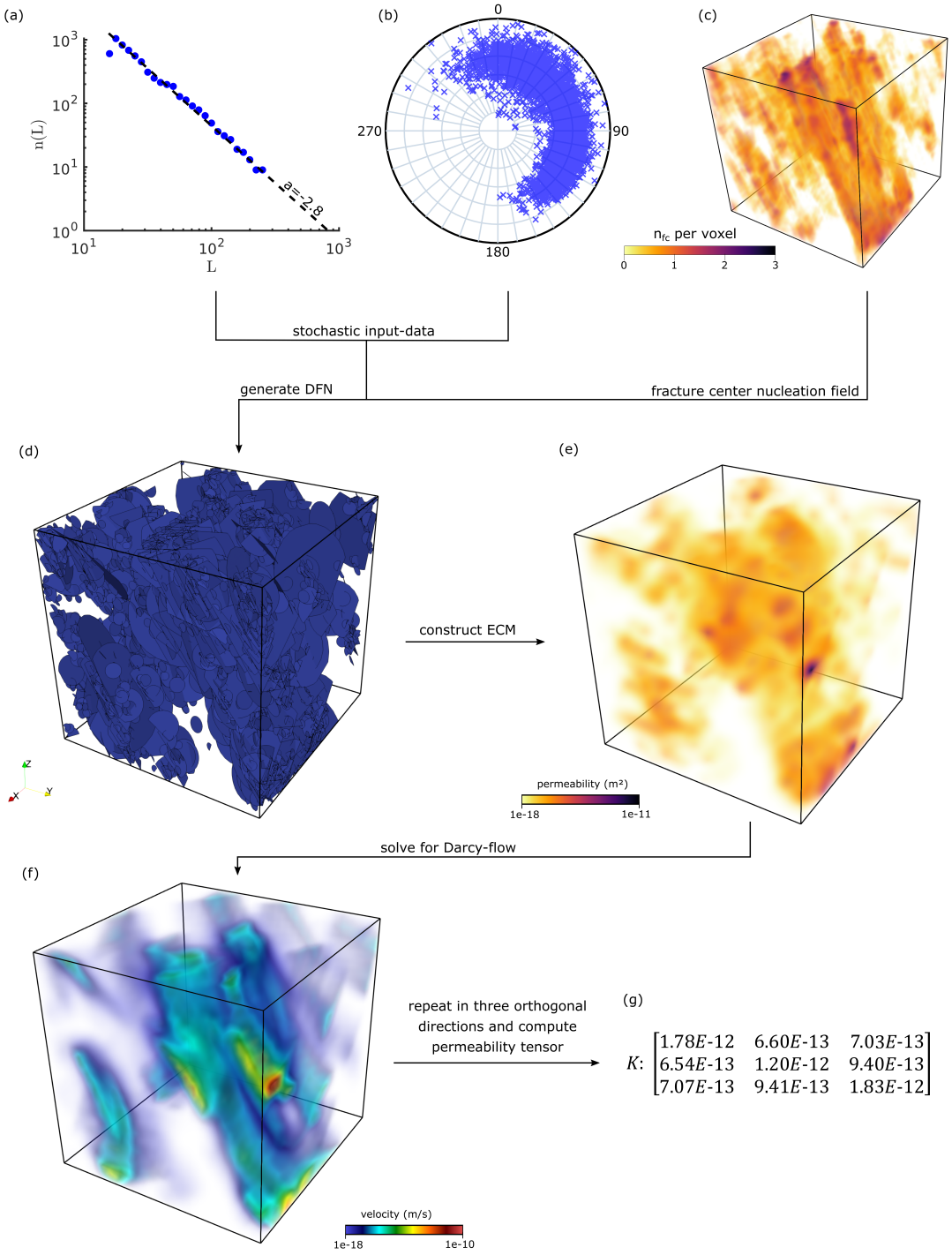

FIGURE 5.1: Sketch of the workflow to obtain the permeability tensor of a DFN that reflects observed fracture-length, -orientation and -position distributions of a natural occurring fracture zone. Panel *a* shows the fracture size distribution (power-law between 15 and 250 *m* in this case with an exponent of -2.8), panel *b* the orientation distribution of two fracture sets (dip-direction and dip of 026|57 and 093|59 for set 1 and 2, respectively with fisher dispersion values of 7). In panel *c*, the nucleation field for fracture centers (see text for details) is displayed, whereas red colors indicate a larger number of fracture centers (n_{fc}) per voxel. The resulting DFN based on the input data from *a*-*c* with 6000 fractures is shown in panel *d*. The permeability structure of the constructed ECM of the DFN in *d* is displayed in *e*, whereas the velocity distribution for a pressure gradient aligned in the vertical direction, obtained from continuum-flow simluations is given in *f*. Repeating this procedure for pressure gradients aligned in both principal directions in the horizontal plane yields the permeability tensor shown in *g*.

As observed faults for the test site show minor to non-recognizable amounts of shear displacement, we assume that it is valid to couple the prescription of fracture aperture correlation length to its mean aperture by $l_c = \bar{a} * 1.5$.. Thus, the minimal voxel-size δx_{min} for discretizing the ECM is given as $\delta x_{min} = 16 * (\bar{a}_{max} * 1.5)$ to full-fill the condition proposed by Méheust and Schmittbuhl (2003) or Kottwitz et al. (2020) that ensures the applicability of prescribing an average fracture flow behaviour. According to Kottwitz et al. (2021), the maximum discretization voxel-size has to be lower than a third of the minimal fracture length (L_{min}) in the system to ensure correct network flow simulations. Hence, the range of applicable δx for ECM discretization ranges between $L_{min}/3 >= \delta_x >= 24\bar{a}_{max}$. In figure 5.1, an application of the described procedure is demonstrated for a hypothetical damage zone.

5.2.4 Multi-scale fluid flow modeling & benchmark validation

Our approach to model fluid flow in fractured-porous media involves direct flow modeling at the micro scale and continuum flow modeling at the macro scale. Direct flow modeling of a single phase of fluid in a digital representation of the rocks pore space is based on the Navier-Stokes equations (e.g., Bear, 1972). For most subsurface flow conditions, it is common to assume laminar flow conditions, i. e. Reynolds numbers below 1 - 10 (Bear, 1972). Then, the Stokes equations approximate the motion of an iso-viscous, iso-thermal and incompressible fluid at steady-state conditions by:

$$\mu \nabla^2 v = \nabla P, \tag{5.13}$$

$$\nabla \cdot v = 0, \tag{5.14}$$

with the fluid's dynamic viscosity μ, pressure P and velocity vector $v = (v_x, v_y, v_z)$, ∇, $\nabla\cdot$, and ∇^2 denote the gradient, divergence, and Laplace operator for 3D Cartesian coordinates, respectively. We use the methodology described and benchmarked in (Eichheimer et al., 2019; Eichheimer et al., 2020) and already applied in Kottwitz et al. (2020) and Kottwitz et al. (2021) to obtain intrinsic permeabilities of fractured-porous media voxel data sets There, the 3D staggered grid finite difference code LaMEM (Kaus et al., 2016) is employed to solve equations 5.13 and 5.14, utilizing the PETSc framework (Balay et al., 2018) for high-performance-computing (HPC) optimized parallelization. The volume average of the resulting velocities (e.g., Osorno et al., 2015) is substituted into Darcy's law to yield an intrinsic permeability value for the direction that corresponds to the direction of the applied pressure gradient.
At the macro scale, the Darcy equations (Darcy, 1856) govern fluid motion under the same simplifications that hold for the Stokes equations and are given for steady-state conditions by:

$$q = -K \nabla P, \tag{5.15}$$

$$\nabla \cdot q = 0, \tag{5.16}$$

whereas the specific discharge is given by q and the positive definite, symmetric hydraulic conductivity tensor by K according to:

$$K = \begin{bmatrix} k_{xx} & k_{yx} & k_{zx} \\ k_{yx} & k_{yy} & k_{zy} \\ k_{zx} & k_{zy} & k_{zz} \end{bmatrix} \frac{\rho g}{\mu}, \tag{5.17}$$

with the principal permeability tensor components k_{xx}, k_{yy} and k_{zz}, the off-diagonal components k_{yx}, k_{zx} and k_{zy} as well as fluid density ρ, gravitational acceleration g and fluid dynamic viscosity μ. In contrast to direct flow simulations that require a physical representation of pore space, continuum flow modeling techniques average the hydraulic properties over certain control volumes. They usually arrange in continuous grids of cells with unique permeability tensors. Here, we utilize a 3D finite element approximation (e.g, Hughes, 1987; Zienkiewicz and Taylor, 2000) for equations 5.16 and 5.15 to simulate pressure diffusion through a grid of rectangular voxel elements with eight internal integration points each to approximate volume integrals with linear interpolation functions by Gauss-Legendre quadrature rule (e.g., Belytschko et al., 2000; Zienkiewicz and Taylor, 2000). Again, the PETSc framework (Balay et al., 2018) is used for HPC scalability and accelerating the solution process with multi-grid solvers. By applying a pressure gradient at two opposing model boundaries and a linear interpolation between both pressures at the remaining four boundaries (see figure A1 in Appendix of Kottwitz et al., 2021), one can obtain the entries of the permeability tensor that correspond to the direction of the applied pressure gradient. Repeating the simulation two times while changing the direction of the applied pressure gradient to the two remaining principal directions in a Cartesian coordinate system yields the full permeability tensor of the considered medium. A comparison of this methodology with 17 different numerical approaches to model fluid flow in fractured porous media (Berre et al., 2020) has proven its applicability. To further validate the above-mentioned direct and continuum methods to simulate fluid flow, we will conduct a benchmark study with a 3D-printed structure of a simple fracture network. Comparing the numerically simulated permeabilities via both methods (3D binarized voxel model and 3D fully anisotropic continuum model with intersection-flow localization compensation) to the ones determined from analog flow-through experiments with synthetic silicon oil (classified fluid with a higher viscosity and a lower sensitivity to surrounding temperatures than water to provide laminar flow conditions) yields the possibility to validate the numerical simulation. After successful validation, the effects of individual fracture morphology (prescribed with varying hydraulic efficiencies) on damage zone permeability are explored in a numerical parameter study.

Author contributions

Chapter 2 - The hydraulic efficiency of single fractures: Correcting the cubic law parametrization for self-affine surface roughness and fracture closure. *Kottwitz, M. O., Popov, A. A., Baumann, T. S., and Kaus, B. J. P.*
MOK wrote the manuscript, performed numerical simulations, analyzed the data and generated the figures. AAP supervised and designed the study, provided the computational framework and edited the manuscript. TSB assisted to data fitting and edited the manuscript. BJPK helped designing the study, assisted to find an analytical model and edited the manuscript.

Chapter 3 - The correlation lengths and permeabilities of natural rock discontinuities. *Kottwitz, M. O., Klaver, J., Schmatz, J., Reinhardt, M., Enzmann, F., Popov, A. A., and Kaus, B. J. P.*
MOK designed the study, wrote the manuscript, performed numerical simulations, analyzed the data and generated the figures. JK, JS, MR and FE scanned, analyzed and segmented the input data sets. JK and MR edited the manuscript. AAP and BJPK provided the computational framework.

Chapter 4 - Equivalent continuum-based upscaling of flow in discrete fracture networks: The fracture-and-pipe model. *Kottwitz, M. O., Popov, A. A., Abe, S., and Kaus, B. J. P.*
MOK designed the study, wrote the manuscript, performed numerical simulations, analyzed the data, generated the figures and assisted in code development. AAP supervised and helped designing the study, implemented the numerical methods and edited the manuscript. SA helped designing the study and edited the manuscript. BJPK edited the manuscript and discussed the results.

Chapter 5 - Outlook: Insights from the PERMEA project. *Kottwitz, M. O., Popov, A. A., and Kaus, B. J. P., Deckert, H., Abe, S., Costa, A., Schmatz, J., Klaver, J., Bauer,W. and Freitag, S.*
MOK designed the study, wrote the manuscript, performed numerical simulations, and generated the figures and assisted in code development. AAP and BJPK provided the computational framework. HD and SA provided the workflow and resources for the digital mapping approach. HD, JS, JK, WB and FS acquired field and experimental data of the test site. HD and AC will provide the 3D printing workflow and experimental permeability measurements.

Eidesstattliche Erklärung

Ich versichere hiermit gemäß 10 Abs. 3d der Promotionsordnung des Fachbereichs 09 (Chemie, Pharmazie und Geowissenschaften) der Johannes Gutenberg-Universität Mainz vom 24.07.2007, die als Dissertation vorgelegte Arbeit selbständig und nur unter Verwendung der in der Arbeit angegebenen Hilfsmittel verfasst zu haben. Ich habe oder hatte die hier als Dissertation vorgelegte Arbeit nicht als Prüfungsarbeit für eine staatliche oder andere wissenschaftliche Prüfung eingereicht. Ich hatte weder die jetzt als Dissertation vorgelegte Arbeit noch Teile davon bei einer anderen Fakultät bzw. einem anderen Fachbereich als Dissertation eingereicht.

(Maximilian Oskar Kottwitz)
Mainz, 2021

Bibliography

Akara, M. E. M., Reeves, D. M., and Parashar, R. (2020). "Enhancing fracture-network characterization and discrete-fracture-network simulation with high-resolution surveys using unmanned aerial vehicles". In: *Hydrogeology Journal* 28.7, pp. 2285–2302. ISSN: 1435-0157. DOI: 10.1007/s10040-020-02178-y.

Alghalandis, Y. F. (2017). "ADFNE: Open source software for discrete fracture network engineering, two and three dimensional applications". In: *Computers and Geosciences* 102, pp. 1–11. ISSN: 0098-3004. DOI: 10.1016/j.cageo.2017.02.002.

Andrä, H., Combaret, N., Dvorkin, J., Glatt, E., Han, J., Kabel, M., Keehm, Y., Krzikalla, F., Lee, M., Madonna, C., Marsh, M., Mukerji, T., Saenger, E. H., Sain, R., Saxena, N., Ricker, S., Wiegmann, A., and Zhan, X. (2013a). "Digital rock physics benchmarks-Part I: Imaging and segmentation". In: *Computers and Geosciences* 50, pp. 25–32. ISSN: 00983004. DOI: 10.1016/j.cageo.2012.09.005.

— (2013b). "Digital rock physics benchmarks-part II: Computing effective properties". In: *Computers and Geosciences* 50, pp. 33–43. ISSN: 00983004. DOI: 10.1016/j.cageo.2012.09.008.

Aydin, A. (2000). "Fractures, faults, and hydrocarbon entrapment, migration and flow". In: *Marine and Petroleum Geology* 17.7, pp. 797–814. ISSN: 02648172. DOI: 10.1016/S0264-8172(00)00020-9.

Azizmohammadi, S. and Matthäi, S. K. (2017). "Is the permeability of naturally fractured rocks scale dependent?" In: *Water Resources Research* 53.9, pp. 8041–8063. DOI: https://doi.org/10.1002/2016WR019764.

Baker, B. R., Gessner, K., Holden, E.-J., and Squelch, A. P. (2008). "Automatic detection of anisotropic features on rock surfaces". In: *Geosphere* 4.2, pp. 418–428.

Balay, S., Abhyankar, S., Adams, M., Brown, J., Brune, P., Buschelman, K., Dalcin, L., Dener, A., Eijkhout, V., Gropp, W, and Others (2018). *PETSc Users Manual: Revision 3.10*. Tech. rep. Argonne National Lab.(ANL), Argonne, IL (United States).

Barenblatt, G. I., Zheltov, I. P., and Kochina, I. N. (1960). "Basic concepts in the theory of seepage of homogeneous liquids in fissured rocks [strata]". In: *Journal of Applied Mathematics and Mechanics* 24.5, pp. 1286–1303. ISSN: 00218928. DOI: 10.1016/0021-8928(60)90107-6.

Barton, N., Bandis, S., and Bakhtar, K. (1985). "Strength, deformation and conductivity coupling of rock joints". In: *International Journal of Rock Mechanics and Mining Sciences and* 22.3, pp. 121–140. ISSN: 01489062. DOI: 10.1016/0148-9062(85)93227-9.

Barton, N. and Choubey, V. (1977). "The shear strength of rock joints in theory and practice". In: *Rock mechanics* 10.1, pp. 1–54. ISSN: 1434-453X. DOI: 10.1007/BF01261801.

Barton, N. and Quadros, E. F. de (1997). "Joint aperture and roughness in the prediction of flow and groutability of rock masses". In: *International Journal of Rock Mechanics and Mining Sciences* 34.3-4, 252–e1.

Batchelor, G. K. (1967). *An Introduction to Fluid Dynamics*. Cambridge Mathematical Library. Cambridge University Press. DOI: 10.1017/CBO9780511800955.

Bear, J. (1972). *Dynamics of fluids in porous media*. Elsevier, New York.

Belytschko, T., Liu, W. K., Moran, B., and Elkhodary, K. (2000). *Nonlinear finite elements for continua and structures*. John Wiley & Sons.

Berg, S., Kutra, D., Kroeger, T., Straehle, C. N., Kausler, B. X., Haubold, C., Schiegg, M., Ales, J., Beier, T., Rudy, M., Eren, K., Cervantes, J. I., Xu, B., Beuttenmueller, F., Wolny, A., Zhang, C., Koethe, U., Hamprecht, F. A., and Kreshuk, A. (2019). "ilastik: interactive machine learning for (bio)image analysis". In: *Nature Methods* 16.12, pp. 1226–1232. ISSN: 1548-7105. DOI: 10.1038/s41592-019-0582-9.

Berkowitz, B. (2002). "Characterizing flow and transport in fractured geological media: A review". In: *Advances in Water Resources* 25.8-12, pp. 861–884. ISSN: 03091708. DOI: 10.1016/S0309-1708(02)00042-8.

Berre, I., Doster, F., and Keilegavlen, E. (2019). "Flow in fractured porous media: A review of conceptual models and discretization approaches". In: *Transport in Porous Media* 130.1, pp. 215–236. DOI: 10.1007/s11242-018-1171-6.

Berre, I. et al. (2020). *Verification benchmarks for single-phase flow in three-dimensional fractured porous media*. arXiv: 2002.07005 [math.NA].

Bertrand, L., Géraud, Y., Le Garzic, E., Place, J., Diraison, M., Walter, B., and Haffen, S. (2015). "A multiscale analysis of a fracture pattern in granite: A case study ofthe Tamariu granite, Catalunya, Spain". In: *Journal of Structural Geology* 78, pp. 52–66. ISSN: 01918141. DOI: 10.1016/j.jsg.2015.05.013.

Best, D. J. and Fisher, N. I. (1979). "Efficient Simulation of the von Mises Distribution". In: *Journal of the Royal Statistical Society. Series C (Applied Statistics)* 28.2, pp. 152–157. ISSN: 00359254, 14679876. DOI: 10.2307/2346732.

Bieniawski, Z. T. (1989). *Engineering rock mass classifications: a complete manual for engineers and geologists in mining, civil, and petroleum engineering*. John Wiley & Sons.

Bodvarsson, G. S., Pruess, K. O., and Sullivan, M. J. (1985). "Injection and Energy Recovery in Fractured Geothermal Reservoirs". In: *Society of Petroleum Engineers Journal* 25.02, pp. 303–312. ISSN: 0197-7520. DOI: 10.2118/11689-PA.

Boffa, J. M., Allain, C., and Hulin, J. P. (1998). "Experimental analysis of fracture rugosity in granular and compact rocks". In: *The European Physical Journal-Applied Physics* 2.3, pp. 281–289. DOI: https://doi.org/10.1051/epjap:1998194.

Bogdanov, I. I., Mourzenko, V. V., Thovert, J.-F., and Adler, P. M. (2003). "Effective permeability of fractured porous media in steady state flow". In: *Water Resources Research* 39.1. DOI: 10.1029/2001WR000756.

Bonneau, F., Caumon, G., and Renard, P. (2016). "Impact of a stochastic sequential initiation of fractures on the spatial correlations and connectivity of discrete fracture networks". In:

Journal of Geophysical Research: Solid Earth 121.8, pp. 5641–5658. ISSN: 2169-9313. DOI: https://doi.org/10.1002/2015JB012451.

Bonnet, E., Bour, O., Odling, N. E., Davy, P., Main, I., Cowie, P., and Berkowitz, B. (2001). "Scaling of fracture systems in geological media". In: *Reviews of Geophysics* 39.3, pp. 347–383. DOI: https://doi.org/10.1029/1999RG000074.

Botros, F. E., Hassan, A. E., Reeves, D. M., and Pohll, G. (2008). "On mapping fracture networks onto continuum". In: *Water Resources Research* 44.8. DOI: 10.1029/2007WR006092.

Bouchaud, E. (1997). "Scaling properties of cracks". In: *Journal of Physics: Condensed Matter* 9.21, pp. 4319–4344. DOI: https://doi.org/10.1088%2F0953-8984%2F9%2F21%2F002.

Bourbiaux, B., Basquet, R., Daniel, J. M., Hu, L., Jenni, S., Lange, G., and Rasolofosaon, P. (2005). "Fractured reservoirs modelling: a review of the challenges and some recent solutions". In: *First Break* 23.9. ISSN: 0263-5046. DOI: 10.3997/1365-2397.2005018.

Brodsky, E. E., Gilchrist, J. J., Sagy, A., and Collettini, C. (2011). "Faults smooth gradually as a function of slip". In: *Earth and Planetary Science Letters* 302.1, pp. 185–193.

Brown, S. R. (1987). "Fluid flow through rock joints: the effect of surface roughness". In: *Journal of Geophysical Research: Solid Earth* 92.B2, pp. 1337–1347. DOI: 10.1029/JB092iB02p01337.

— (1995). "Simple mathematical model of a rough fracture". In: *Journal of Geophysical Research: Solid Earth* 100.B4, pp. 5941–5952. DOI: 10.1029/94JB03262.

Brown, S. R. and Scholz, C. H. (1985). "Broad bandwidth study of the topography of natural rock surfaces". In: *Journal of Geophysical Research: Solid Earth* 90.B14, pp. 12575–12582. DOI: https://doi.org/10.1029/94JB03262.

Brush, D. J. and Thomson, N. R. (2003). "Fluid flow in synthetic rough-walled fractures: Navier-Stokes, Stokes, and local cubic law simulations". In: *Water Resources Research* 39.4. DOI: https://doi.org/10.1029/2002WR001346.

Cacace, M., Blöcher, G., Watanabe, N., Moeck, I., Börsing, N., Scheck-Wenderoth, M., Kolditz, O., and Huenges, E. (2013). "Modelling of fractured carbonate reservoirs: outline of a novel technique via a case study from the Molasse Basin, southern Bavaria, Germany". In: *Environmental Earth Sciences* 70.8, pp. 3585–3602. ISSN: 1866-6299. DOI: 10.1007/s12665-013-2402-3.

Cacas, M. C., Ledoux, E., Marsily, G. de, Tillie, B., Barbreau, A., Durand, E., Feuga, B., and Peaudecerf, P. (1990). "Modeling fracture flow with a stochastic discrete fracture network: calibration and validation: 1. The flow model". In: *Water Resources Research* 26.3, pp. 479–489. DOI: 10.1029/WR026i003p00479.

Candela, T., Renard, F., Bouchon, M., Brouste, A., Marsan, D., Schmittbuhl, J., and Voisin, C. (2009). "Characterization of fault roughness at various scales: Implications of three-dimensional high resolution topography measurements". In: *Mechanics, Structure and Evolution of Fault Zones*. Springer, pp. 1817–1851.

Candela, T., Renard, F., Klinger, Y., Mair, K., Schmittbuhl, J., and Brodsky, E. E. (2012). "Roughness of fault surfaces over nine decades of length scales". In: *Journal of Geophysical Research: Solid Earth* 117.B8. DOI: https://doi.org/10.1029/2011JB009041.

Chen, C., Peng, S., Wu, S., and Xu, J. (2019). "The effect of chemical erosion on mechanical properties and fracture of sandstone under shear loading: an experimental study". In: *Scientific Reports* 9.1, p. 19886. ISSN: 2045-2322. DOI: 10.1038/s41598-019-56196-2.

Chen, M., Bai, M., and Roegiers, J.-C. (1999). "Permeability tensors of anisotropic fracture networks". In: *Mathematical Geology* 31.4, pp. 335–373. DOI: 10.1023/A:1007534523363.

Chen, S.-H., Feng, X.-M., and Isam, S (2008). "Numerical estimation of REV and permeability tensor for fractured rock masses by composite element method". In: *International Journal for Numerical and Analytical Methods in Geomechanics* 32.12, pp. 1459–1477. ISSN: 0363-9061. DOI: https://doi.org/10.1002/nag.679.

Chen, T., Clauser, C., Marquart, G., Willbrand, K., and Mottaghy, D. (2015). "A new upscaling method for fractured porous media". In: *Advances in Water Resources* 80, pp. 60–68. ISSN: 0309-1708. DOI: https://doi.org/10.1016/j.advwatres.2015.03.009.

Christie, M. A. and Blunt, M. J. (2001). *Tenth SPE Comparative Solution Project: A Comparison of Upscaling Techniques*. DOI: 10.2118/66599-MS.

Cnudde, V. and Boone, M. N. (2013). *High-resolution X-ray computed tomography in geosciences: A review of the current technology and applications*. DOI: 10.1016/j.earscirev.2013.04.003.

Cooper, H. and Jacob, C. (1946). "A generalized graphical method for evaluating formation constants and summarizing well-field history". In: *Eos, Transactions American Geophysical Union* 27.4, pp. 526–534. ISSN: 0002-8606. DOI: https://doi.org/10.1029/TR027i004p00526.

Crandall, D., Bromhal, G., and Karpyn, Z. T. (2010). "Numerical simulations examining the relationship between wall-roughness and fluid flow in rock fractures". In: *International Journal of Rock Mechanics and Mining Sciences* 47.5, pp. 784–796. ISSN: 13651609. DOI: 10.1016/j.ijrmms.2010.03.015.

Darcel, C., Bour, O., Davy, P., and Dreuzy, J. R. de (2003). "Connectivity properties of two-dimensional fracture networks with stochastic fractal correlation". In: *Water Resources Research* 39.10. DOI: 10.1029/2002WR001628.

Darcy, H. P. G. (1856). *Les Fontaines publiques de la ville de Dijon. Exposition et application des principes à suivre et des formules à employer dans les questions de distribution d'eau, etc.* V. Dalamont.

Dastidar, R., Sondergeld, C. H., and Rai, C. S. (2007). "An Improved Empirical Permeability Estimator From Mercury Injection For Tight Clastic Rocks". In: *Petrophysics - The SPWLA Journal of Formation Evaluation and Reservoir Description* 48.03. ISSN: 1529-9074.

Davy, P., Bour, O., De Dreuzy, J.-R., and Darcel, C. (2006). "Flow in multiscale fractal fracture networks". In: *Geological Society, London, Special Publications* 261.1, pp. 31–45. ISSN: 0305-8719. DOI: 10.1144/GSL.SP.2006.261.01.03.

Davy, P., Darcel, C., Le Goc, R., Munier, R., Selroos, J. O., and Mas Ivars, D. (2018). "DFN, why, how and what for, concepts, theories and issues". In: *2nd International Discrete Fracture Network Engineering Conference*. URL: id:ARMA-DFNE-18-0310.

Davy, P., Le Goc, R., and Darcel, C. (2013). "A model of fracture nucleation, growth and arrest, and consequences for fracture density and scaling". In: *Journal of Geophysical Research: Solid Earth* 118.4, pp. 1393–1407. DOI: 10.1002/jgrb.50120.

De Dreuzy, J.-R., Davy, P, and Bour, O (2002). "Hydraulic properties of two-dimensional random fracture networks following power law distributions of length and aperture". In: *Water Resources Research* 38.12, pp. 1–9. DOI: https://doi.org/10.1029/2001WR001009.

DErrico, J. (2006). *Surface Fitting using gridfit*. MATLAB Central File Exchange. URL: https://de.mathworks.com/matlabcentral/fileexchange/8998-surface-fitting-using-gridfit.

Dershowitz, W., Wallman, P., and Kinrod, S. (1991). *Discrete fracture modelling for the Stripa site characterization and validation drift inflow predictions. Stripa Project Tech Rep 91–16.* Tech. rep. SKB Swedish Nuclear Fuel and Waste Management Co., Sweden, Stockholm.

Dershowitz, W. S. and Einstein, H. H. (1988). "Characterizing rock joint geometry with joint system models". In: *Rock mechanics and rock engineering* 21.1, pp. 21–51. DOI: 10.1007/BF01019674.

Dershowitz, W. S. and Herda, H. H. (1992). *Interpretation of fracture spacing and intensity*.

Dreuzy, J.-R. de, Méheust, Y., and Pichot, G. (2012). "Influence of fracture scale heterogeneity on the flow properties of three-dimensional discrete fracture networks (DFN)". In: *Journal of Geophysical Research: Solid Earth* 117.B11. DOI: 10.1029/2012JB009461.

Dupuit, J. (1863). *Études théoriques et pratiques sur le mouvement des eaux dans les canaux découverts et à travers les terrains perméabls: avec des considérations relatives au régime des grandes eaux, au débouché à leur donner, et à la marche des alluvions dans les rivière*. Dunod.

Durham, W. B., Bourcier, W. L., and Burton, E. A. (2001). "Direct observation of reactive flow in a single fracture". In: *Water Resources Research* 37.1, pp. 1–12. DOI: https://doi.org/10.1029/2000WR900228.

Durlofsky, L. J. (1991). "Numerical calculation of equivalent grid block permeability tensors for heterogeneous porous media". In: *Water Resources Research* 27.5, pp. 699–708. ISSN: 0043-1397. DOI: https://doi.org/10.1029/91WR00107.

Eichheimer, P, Thielmann, M, Fujita, W, Golabek, G. J., Nakamura, M, Okumura, S, Nakatani, T, and Kottwitz, M. O. (2020). "Combined numerical and experimental study of microstructure and permeability in porous granular media". In: *Solid Earth* 11.3, pp. 1079–1095. DOI: 10.5194/se-11-1079-2020.

Eichheimer, P., Thielmann, M., Popov, A., Golabek, G. J., Fujita, W., Kottwitz, M. O., and Kaus, B. J. P. (2019). "Pore-scale permeability prediction for Newtonian and non-Newtonian fluids". In: *Solid Earth* 10.5, pp. 1717–1731. DOI: 10.5194/se-10-1717-2019.

Espejel, R. L., Alves, T. M., and Blenkinsop, T. G. (2020). "Multi-scale fracture network characterisation on carbonate platforms". In: *Journal of Structural Geology* 140, p. 104160. ISSN: 01918141. DOI: 10.1016/j.jsg.2020.104160.

Evans, J. P., Forster, C. B., and Goddard, J. V. (1997). "Permeability of fault-related rocks, and implications for hydraulic structure of fault zones". In: *Journal of Structural Geology* 19.11, pp. 1393–1404. ISSN: 01918141. DOI: 10.1016/S0191-8141(97)00057-6.

Farmer, C. L. (2002). "Upscaling: a review". In: *International Journal for Numerical Methods in Fluids* 40.1-2, pp. 63–78. ISSN: 0271-2091. DOI: https://doi.org/10.1002/fld.267.

Faulkner, D. R., Jackson, C. A., Lunn, R. J., Schlische, R. W., Shipton, Z. K., Wibberley, C. A., and Withjack, M. O. (2010). *A review of recent developments concerning the structure, mechanics and fluid flow properties of fault zones*. DOI: 10.1016/j.jsg.2010.06.009.

Filomena, C. M., Hornung, J., and Stollhofen, H. (2014). "Assessing accuracy of gas-driven permeability measurements: a comparative study of diverse Hassler-cell and probe permeameter devices". In: *Solid Earth* 5.1, pp. 1–11. DOI: 10.5194/se-5-1-2014.

Fisher, N. I., Lewis, T., and Embleton, B. J. J. (1987). *Statistical Analysis of Spherical Data*. Cambridge: Cambridge University Press. ISBN: 9780521456999. DOI: DOI:10.1017/CBO9780511623059.

Fisher, R. A. (1953). "Dispersion on a sphere". In: *Proceedings of the Royal Society of London. Series A. Mathematical and Physical Sciences* 217.1130, pp. 295–305. DOI: 10.1098/rspa.1953.0064.

Foroughi, S., Jamshidi, S., and Pishvaie, M. R. (2018). "New Correlative Models to Improve Prediction of Fracture Permeability and Inertial Resistance Coefficient". In: *Transport in Porous Media* 121.3, pp. 557–584. DOI: https://doi.org/10.1007/s11242-017-0930-0.

Fossen, H., Schultz, R. A., Shipton, Z. K., and Mair, K. (2007). *Deformation bands in sandstone*. DOI: 10.1144/0016-76492006-036.

Frank, S., Heinze, T., Ribbers, M., and Wohnlich, S. (2020a). *Experimental Reproducibility and Natural Variability of Hydraulic Transport Properties of Fractured Sandstone Samples*. DOI: 10.3390/geosciences10110458.

Frank, S., Heinze, T., and Wohnlich, S. (2020b). *Comparison of Surface Roughness and Transport Processes of Sawed, Split and Natural Sandstone Fractures*. DOI: 10.3390/w12092530.

Geurts, P., Irrthum, A., and Wehenkel, L. (2009). "Supervised learning with decision tree-based methods in computational and systems biology". In: *Molecular BioSystems* 5.12, pp. 1593–1605. ISSN: 1742-206X. DOI: 10.1039/B907946G.

Ghosh, B., Samhar, Ali, A., and Hadi Belhaj, · (2020). "Controlling excess water production in fractured carbonate reservoirs: chemical zonal protection design". In: *Journal of Petroleum Exploration and Production Technology* 10, pp. 1921–1931. DOI: 10.1007/s13202-020-00842-3.

Girault, V. and Raviart, P.-A. (1986). "Finite element methods for Navier-Stokes equations: Theory and algorithms". In: *NASA STI/Recon Technical Report A* 87, p. 52227. URL: https://ui.adsabs.harvard.edu/abs/1986STIA...8752227G.

Glover, P. W. J., Matsuki, K., Hikima, R., and Hayashi, K. (1998a). "Fluid flow in synthetic rough fractures and application to the Hachimantai geothermal hot dry rock test site". In: *Journal of Geophysical Research: Solid Earth* 103.B5, pp. 9621–9635. ISSN: 0148-0227. DOI: https://doi.org/10.1029/97JB01613.

— (1998b). "Synthetic rough fractures in rocks". In: *Journal of Geophysical Research: Solid Earth* 103.B5, pp. 9609–9620. ISSN: 0148-0227. DOI: https://doi.org/10.1029/97JB02836.

Goldscheider, N., Mádl-Szőnyi, J., Erőss, A., and Schill, E. (2010). "Review: Thermal water resources in carbonate rock aquifers". In: *Hydrogeology Journal* 18.6, pp. 1303–1318. ISSN: 1435-0157. DOI: 10.1007/s10040-010-0611-3.

Gong, J and Rossen, W. R. (2017). "Modeling flow in naturally fractured reservoirs: effect of fracture aperture distribution on dominant sub-network for flow". In: *Petroleum Science* 14.1, pp. 138–154. ISSN: 1995-8226. DOI: 10.1007/s12182-016-0132-3.

Gudmundsson, A. (2011). *Rock Fractures in Geological Processes*. Cambridge: Cambridge University Press. ISBN: 9780521863926. DOI: DOI:10.1017/CBO9780511975684.

Hadgu, T., Karra, S., Kalinina, E., Makedonska, N., Hyman, J. D., Klise, K., Viswanathan, H. S., and Wang, Y. (2017). "A comparative study of discrete fracture network and equivalent continuum models for simulating flow and transport in the far field of a hypothetical nuclear waste repository in crystalline host rock". In: *Journal of Hydrology* 553, pp. 59–70. ISSN: 0022-1694. DOI: 10.1016/j.jhydrol.2017.07.046.

Hardebol, N. J., Maier, C., Nick, H., Geiger, S., Bertotti, G., and Boro, H. (2015). "Multiscale fracture network characterization and impact on flow: A case study on the Latemar carbonate platform". In: *Journal of Geophysical Research: Solid Earth* 120.12, pp. 8197–8222. ISSN: 2169-9313. DOI: https://doi.org/10.1002/2015JB011879.

Hauge, V. L., Lie, K.-A., and Natvig, J. R. (2012). "Flow-based coarsening for multiscale simulation of transport in porous media". In: *Computational Geosciences* 16.2, pp. 391–408. DOI: https://doi.org/10.1007/s10596-011-9230-x.

Healy, D., Rizzo, R. E., Cornwell, D. G., Farrell, N. J. C., Watkins, H., Timms, N. E., Gomez-Rivas, E., and Smith, M. (2017). "FracPaQ: A MATLAB™ toolbox for the quantification of fracture patterns". In: *Journal of Structural Geology* 95, pp. 1–16. ISSN: 0191-8141. DOI: 10.1016/j.jsg.2016.12.003.

Homuth, S., Götz, A. E., and Sass, I. (2014). "Lithofacies and depth dependency of thermo- and petrophysical rock parameters of the Upper Jurassic geothermal carbonate reservoirs of the Molasse Basin". In: *Zeitschrift der Deutschen Gesellschaft für Geowissenschaften* 165.3, pp. 469–486. DOI: 10.1127/1860-1804/2014/0074.

Hughes, T. J. R. (1987). *The Finite Element Method: Linear Static and Dynamic Finite Element Analysis*. Prentice-Hall Inc., Englewood Cliffs, New Jersey.

Hyman, J. D., Karra, S., Makedonska, N., Gable, C. W., Painter, S. L., and Viswanathan, H. S. (2015). "dfnWorks: A discrete fracture network framework for modeling subsurface flow and transport". In: *Computers and Geosciences* 84, pp. 10–19. ISSN: 0098-3004. DOI: 10.1016/j.cageo.2015.08.001.

IPCC (2005). *Carbon Dioxide Capture and Storage*. Tech. rep. IPCC, p. 431. URL: https://www.ipcc.ch/report/carbon-dioxide-capture-and-storage/.

Jackson, C. P., Hoch, A. R., and Todman, S. (2000). "Self-consistency of a heterogeneous continuum porous medium representation of a fractured medium". In: *Water Resources Research* 36.1, pp. 189–202. DOI: 10.1029/1999WR900249.

Jacobs, T. D. B., Junge, T., and Pastewka, L. (2017). "Quantitative characterization of surface topography using spectral analysis". In: *Surface Topography: Metrology and Properties* 5.1, p. 13001.

Jin, Y., Dong, J., Zhang, X., Li, X., and Wu, Y. (2017). "Scale and size effects on fluid flow through self-affine rough fractures". In: *International Journal of Heat and Mass Transfer* 105, pp. 443–451. DOI: https://doi.org/10.1016/j.ijheatmasstransfer.2016.10.010.

Jing, L. (2003). "A review of techniques, advances and outstanding issues in numerical modelling for rock mechanics and rock engineering". In: *International Journal of Rock Mechanics*

and Mining Sciences 40.3, pp. 283–353. ISSN: 1365-1609. DOI: 10.1016/S1365-1609(03)00013-3.

Kanafi, M. M. (2016). *Surface generator: artificial randomly rough surfaces*. MATLAB Central File Exchange. URL: https://de.mathworks.com/matlabcentral/fileexchange/60817-surface-generator-artificial-randomly-rough-surfaces.

Karpyn, Z., Landry, C., and Prodanovic, M. (2016). *Induced rough fracture in Berea sandstone core. Retrieved March 01, 2021, from www.digitalrocksportal.org*. DOI: 10.17612/P7J012.

Karpyn, Z. T., Grader, A. S., and Halleck, P. M. (2007). "Visualization of fluid occupancy in a rough fracture using micro-tomography". In: *Journal of Colloid and Interface Science* 307.1, pp. 181–187. ISSN: 00219797. DOI: 10.1016/j.jcis.2006.10.082.

Karpyn, Z. T. and Piri, M. (2007). "Prediction of fluid occupancy in fractures using network modeling and x-ray microtomography. I: Data conditioning and model description". In: *Physical Review E* 76.1, p. 16315. DOI: 10.1103/PhysRevE.76.016315.

Kaufmann, G., Gabrovšek, F., and Romanov, D. (2016). "Dissolution and precipitation of fractures in soluble rock". In: *Hydrol. Earth Syst. Sci. Discuss.* 2016, pp. 1–30. ISSN: 1812-2116. DOI: 10.5194/hess-2016-372.

Kaus, B. J., Popov, A. A., Baumann, T., Pusok, A., Bauville, A., Fernandez, N., and Collignon, M. (2016). "Forward and inverse modelling of lithospheric deformation on geological timescales". In: *Proceedings of NIC Symposium*. URL: http://hdl.handle.net/2128/9842.

Khelifa, C., Zeddouri, A., and Djabes, F. (2014). "Influence of natural fractures on oil production of unconventional reservoirs". In: *Energy Procedia*. Vol. 50. Elsevier Ltd, pp. 360–367. DOI: 10.1016/j.egypro.2014.06.043.

Klaver, J., Hemes, S., Houben, M., Desbois, G., Radi, Z., and Urai, J. L. (2015). "The connectivity of pore space in mudstones: insights from high-pressure Wood's metal injection, BIB-SEM imaging, and mercury intrusion porosimetry". In: *Geofluids* 15.4, pp. 577–591. ISSN: 1468-8115. DOI: https://doi.org/10.1111/gfl.12128.

Klimczak, C., Schultz, R. A., Parashar, R., and Reeves, D. M. (2010). "Cubic law with aperture-length correlation: implications for network scale fluid flow". In: *Hydrogeology Journal* 18.4, pp. 851–862. DOI: https://doi.org/10.1007/s10040-009-0572-6.

Kling, T., Schwarz, J.-O., Wendler, F., Enzmann, F., and Blum, P. (2017). "Fracture flow due to hydrothermally induced quartz growth". In: *Advances in Water Resources* 107, pp. 93–107. DOI: https://doi.org/10.1016/j.advwatres.2017.06.011.

Kluge, C., Milsch, H., and Blöcher, G. (2017). "Permeability of displaced fractures". In: *Energy Procedia* 125, pp. 88–97. DOI: https://doi.org/10.1016/j.egypro.2017.08.077.

Kolditz, O., Shao, H., Wang, W., and Bauer, S. (2016). *NThermo-Hydro-Mechanical-Chemical Processes in Fractured Porous Media: Modelling and Benchmarkingo Title*. Springer Berlin. ISBN: 978-3-319-11894-9. DOI: https://doi.org/10.1007/978-3-319-11894-9.

Kottwitz, M. O., Popov, A. A., Abe, S., and Kaus, B. J. P. (2021). "Equivalent continuum-based upscaling of flow in discrete fracture networks: The fracture-and-pipe model". In: *Solid Earth Discuss.* 2021, pp. 1–27. ISSN: 1869-9537. DOI: 10.5194/se-2020-208.

Kottwitz, M. O., Popov, A. A., Baumann, T. S., and Kaus, B. J. P. (2020). "The hydraulic efficiency of single fractures: correcting the cubic law parameterization for self-affine surface roughness and fracture closure". In: *Solid Earth* 11.3, pp. 947–957. DOI: 10.5194/se-11-947-2020.

La Pointe, P. R., Wallmann, P., and Follin, S. (1995). *Estimation of effective block conductivities based on discrete network analyses using data from the Äspö site (SKB-TR–95-15)*. Tech. rep. Swedish Nuclear Fuel and Waste Management Co.

Lavoine, E, Davy, P, Darcel, C, and Le Goc, R (2019). "On the Density Variability of Poissonian Discrete Fracture Networks, with application to power-law fracture size distributions". In: *Adv. Geosci.* 49, pp. 77–83. ISSN: 1680-7359. DOI: 10.5194/adgeo-49-77-2019.

Lei, Q., Latham, J.-P., and Tsang, C.-F. (2017). "The use of discrete fracture networks for modelling coupled geomechanical and hydrological behaviour of fractured rocks". In: *Computers and Geotechnics* 85, pp. 151–176. ISSN: 0266-352X. DOI: 10.1016/j.compgeo.2016.12.024.

Lemonnier, P and Bourbiaux, B (2010). "Simulation of Naturally Fractured Reservoirs. State of the Art". In: *Oil Gas Sci. Technol. – Rev. IFP* 65.2, pp. 239–262. URL: https://doi.org/10.2516/ogst/2009066.

Leung, C. T. O., Hoch, A. R., and Zimmerman, R. W. (2012). "Comparison of discrete fracture network and equivalent continuum simulations of fluid flow through two-dimensional fracture networks for the DECOVALEX–2011 project". In: *Mineralogical Magazine* 76.8, pp. 3179–3190. DOI: 10.1180/minmag.2012.076.8.31.

LeVeque, R. J. (2002). *Finite Volume Methods for Hyperbolic Problems*. Cambridge: Cambridge University Press. ISBN: 9780521009249. DOI: DOI:10.1017/CBO9780511791253.

Li, B., Mo, Y., Zou, L., Liu, R., and Cvetkovic, V. (2020). "Influence of surface roughness on fluid flow and solute transport through 3D crossed rock fractures". In: *Journal of Hydrology* 582, p. 124284. ISSN: 0022-1694. DOI: 10.1016/j.jhydrol.2019.124284.

Lichtner, P. C., Hammond, G. E., Lu, C., Karra, S., Bisht, G., Andre, B., Mills, R., and Kumar, J. (2015). "PFLOTRAN User Manual: A Massively Parallel Reactive Flow and Transport Model for Describing Surface and Subsurface Processes". In: DOI: 10.2172/1168703.

"Upscaling Petrophysical Properties" (2019). In: *An Introduction to Reservoir Simulation Using MATLAB/GNU Octave: User Guide for the MATLAB Reservoir Simulation Toolbox (MRST)*. Ed. by K.-A. Lie. Cambridge: Cambridge University Press, pp. 558–596. ISBN: 9781108492430. DOI: DOI:10.1017/9781108591416.020.

Lin, G., Liu, J., Mu, L., and Ye, X. (2014). "Weak Galerkin finite element methods for Darcy flow: Anisotropy and heterogeneity". In: *Journal of Computational Physics* 276, pp. 422–437. ISSN: 0021-9991. DOI: https://doi.org/10.1016/j.jcp.2014.07.001.

Liu, R., Li, B., Jiang, Y., and Huang, N. (2016). "Mathematical expressions for estimating equivalent permeability of rock fracture networks". In: *Hydrogeology Journal* 24.7, pp. 1623–1649. DOI: 10.1007/s10040-016-1441-8.

Lomize, G. M. (1951). "Flow in fractured rocks (in Russian)". In: *Gosenergoizdat, Moscow* 127.197, p. 635.

Long, J. C. S., Remer, J. S., Wilson, C. R., and Witherspoon, P. A. (1982). "Porous media equivalents for networks of discontinuous fractures". In: *Water Resources Research* 18.3, pp. 645–658. DOI: 10.1029/WR018i003p00645.

Long, J. C. S., Gilmour, P., and Witherspoon, P. A. (1985). "A Model for Steady Fluid Flow in Random Three-Dimensional Networks of Disc-Shaped Fractures". In: *Water Resources Research* 21.8, pp. 1105–1115. ISSN: 0043-1397. DOI: https://doi.org/10.1029/WR021i008p01105.

Lu, Y. C., Tien, Y. M., and Juang, C. H. (2017). "Uncertainty of 1-D Fracture Intensity Measurements". In: *Journal of Geophysical Research: Solid Earth* 122.11, pp. 9344–9358. ISSN: 2169-9313. DOI: https://doi.org/10.1002/2016JB013620.

Maillot, J, Davy, P, Le Goc, R, Darcel, C, and Dreuzy, J. R. de (2016). "Connectivity, permeability, and channeling in randomly distributed and kinematically defined discrete fracture network models". In: *Water Resources Research* 52.11, pp. 8526–8545. DOI: 10.1002/2016WR018973.

Makedonska, N., Hyman, J. D., Karra, S., Painter, S. L., Gable, C. W., and Viswanathan, H. S. (2016). "Evaluating the effect of internal aperture variability on transport in kilometer scale discrete fracture networks". In: *Advances in Water Resources* 94, pp. 486–497. ISSN: 03091708. DOI: 10.1016/j.advwatres.2016.06.010.

Mandelbrot, B. B. (1982). *The fractal geometry of nature*. Vol. 1. WH freeman.

— (1985). "Self-affine fractals and fractal dimension". In: *Physica scripta* 32.4, p. 257.

March, R., Doster, F., and Geiger, S. (2018). "Assessment of CO2 Storage Potential in Naturally Fractured Reservoirs With Dual-Porosity Models". In: *Water Resources Research* 54.3, pp. 1650–1668. ISSN: 0043-1397. DOI: https://doi.org/10.1002/2017WR022159.

McDonald, M. G. and Harbaugh, A. W. (1988). *A modular three-dimensional finite-difference groundwater flow model*. US Geological Survey.

Méheust, Y. and Schmittbuhl, J. (2000). "Flow enhancement of a rough fracture". In: *Geophysical Research Letters* 27.18, pp. 2989–2992. DOI: 10.1029/1999GL008464.

— (2001). "Geometrical heterogeneities and permeability anisotropy of rough fractures". In: *Journal of Geophysical Research: Solid Earth* 106.B2, pp. 2089–2102. ISSN: 21699356. DOI: 10.1029/2000jb900306.

— (2003). "Scale effects related to flow in rough fractures". In: *Pure and Applied Geophysics* 160.5-6, pp. 1023–1050. DOI: 10.1007/PL00012559.

Morrow, C. A., Shi, L. Q., and Byerlee, J. D. (1984). "Permeability of fault gouge under confining pressure and shear stress". In: *Journal of Geophysical Research: Solid Earth* 89.B5, pp. 3193–3200. ISSN: 0148-0227. DOI: https://doi.org/10.1029/JB089iB05p03193.

Mourzenko, V. V., Thovert, J.-F., and Adler, P. M. (1995). "Permeability of a single fracture; validity of the Reynolds equation". In: *Journal de Physique II* 5.3, pp. 465–482. DOI: 10.1051/jp2:1995133.

— (1996). "Geometry of simulated fractures". In: *Physical Review E* 53.6, p. 5606. DOI: 10.1103/PhysRevE.53.5606.

— (2018). "Conductivity and Transmissivity of a Single Fracture". In: *Transport in Porous Media* 123.2, pp. 235–256. DOI: 10.1007/s11242-018-1037-y.

Nesbit, P. R., Durkin, P. R., Hugenholtz, C. H., Hubbard, S. M., and Kucharczyk, M. (2018). "3-D stratigraphic mapping using a digital outcrop model derived from UAV images and structure-from-motion photogrammetry". In: *Geosphere* 14.6, pp. 2469–2486. ISSN: 1553-040X. DOI: 10.1130/GES01688.1.

Neuman, S. P. (1977). "Theoretical derivation of Darcy's law". In: *Acta Mechanica* 25.3, pp. 153–170. ISSN: 1619-6937. DOI: 10.1007/BF01376989.

Neuman, S. P. (2005). "Trends, prospects and challenges in quantifying flow and transport through fractured rocks". In: *Hydrogeology Journal* 13.1, pp. 124–147. DOI: 10.1007/s10040-004-0397-2.

Noiriel, C., Renard, F., Doan, M. L., and Gratier, J. P. (2010). "Intense fracturing and fracture sealing induced by mineral growth in porous rocks". In: *Chemical Geology* 269.3-4, pp. 197–209. ISSN: 00092541. DOI: 10.1016/j.chemgeo.2009.09.018.

Oda, M. (1985). "Permeability tensor for discontinuous rock masses". In: *Géotechnique* 35.4, pp. 483–495. DOI: 10.1680/geot.1985.35.4.483.

Odling, N. E., Gillespie, P, Bourgine, B, Castaing, C, Chiles, J. P., Christensen, N. P., Fillion, E, Genter, A, Olsen, C, Thrane, L, Trice, R, Aarseth, E, Walsh, J. J., and Watterson, J (1999). "Variations in fracture system geometry and their implications for fluid flow in fractures hydrocarbon reservoirs". In: *Petroleum Geoscience* 5.4, pp. 373–384. ISSN: 1354-0793. DOI: 10.1144/petgeo.5.4.373.

Ogilvie, S. R., Isakov, E., and Glover, P. W. (2006). "Fluid flow through rough fractures in rocks. II: A new matching model for rough rock fractures". In: *Earth and Planetary Science Letters* 241.3-4, pp. 454–465. ISSN: 0012821X. DOI: 10.1016/j.epsl.2005.11.041.

Olariu, M. I., Ferguson, J. F., Aiken, C. L. V., and Xu, X. (2008). "Outcrop fracture characterization using terrestrial laser scanners: Deep-water Jackfork sandstone at Big Rock Quarry, Arkansas". In: *Geosphere* 4.1, pp. 247–259. ISSN: 1553-040X. DOI: 10.1130/GES00139.1.

Olson, J. E. (1993). "Joint pattern development: Effects of subcritical crack growth and mechanical crack interaction". In: *Journal of Geophysical Research: Solid Earth* 98.B7, pp. 12251–12265. ISSN: 0148-0227. DOI: https://doi.org/10.1029/93JB00779.

— (2003). "Sublinear scaling of fracture aperture versus length: An exception or the rule?" In: *Journal of Geophysical Research: Solid Earth* 108.B9. DOI: 10.1029/2001JB000419.

Oron, A. P. and Berkowitz, B. (1998). "Flow in rock fractures: The local cubic law assumption reexamined". In: *Water Resources Research* 34.11, pp. 2811–2825. DOI: 10.1029/98WR02285.

Ortega, O. J., Marrett, R. A., and Laubach, S. E. (2006). "A scale-independent approach to fracture intensity and average spacing measurement". In: *AAPG Bulletin* 90.2, pp. 193–208. ISSN: 0149-1423. DOI: 10.1306/08250505059.

Osorno, M., Uribe, D., Ruiz, O. E., and Steeb, H. (2015). "Finite difference calculations of permeability in large domains in a wide porosity range". In: *Archive of Applied Mechanics* 85.8, pp. 1043–1054. DOI: https://doi.org/10.1007/s00419-015-1025-4.

Patir, N. and Cheng, H. S. (1978). "An average flow model for determining effects of three-dimensional roughness on partial hydrodynamic lubrication". In: *Journal of lubrication Technology* 100.1, pp. 12–17. DOI: 10.1115/1.3453103.

Patterson, J. R., Cardiff, M., and Feigl, K. L. (2020). "Optimizing geothermal production in fractured rock reservoirs under uncertainty". In: *Geothermics* 88, p. 101906. ISSN: 03756505. DOI: 10.1016/j.geothermics.2020.101906.

Peacock, D. C., Sanderson, D. J., and Rotevatn, A. (2018). "Relationships between fractures". In: *Journal of Structural Geology* 106, pp. 41–53. ISSN: 01918141. DOI: 10.1016/j.jsg.2017.11.010.

Perić, M. (2020). "Finite-Volume Methods for Navier-Stokes Equations". In: *Fluids Under Pressure*. Ed. by T. Bodnár, G. P. Galdi, and Š. Nečasová. Cham: Springer International Publishing, pp. 575–638. ISBN: 978-3-030-39639-8. DOI: 10.1007/978-3-030-39639-8_7.

Persson, B. N. J., Albohr, O., Tartaglino, U., Volokitin, A. I., and Tosatti, E. (2004). "On the nature of surface roughness with application to contact mechanics, sealing, rubber friction and adhesion". In: *Journal of Physics: Condensed Matter* 17.1, R1–R62. DOI: https://doi.org/10.1088%2F0953-8984%2F17%2F1%2Fr01.

Piri, M. and Karpyn, Z. T. (2007). "Prediction of fluid occupancy in fractures using network modeling and x-ray microtomography. II: Results". In: *Physical Review E* 76.1, p. 16316. DOI: 10.1103/PhysRevE.76.016316.

Plouraboué, F., Kurowski, P., Hulin, J.-P., Roux, S., and Schmittbuhl, J. (1995). "Aperture of rough cracks". In: *Physical review E* 51.3, pp. 1675–1685. DOI: https://doi.org/10.1103/PhysRevE.51.1675.

Pluymakers, A., Kobchenko, M., and Renard, F. (2017). "How microfracture roughness can be used to distinguish between exhumed cracks and in-situ flow paths in shales". In: *Journal of Structural Geology* 94, pp. 87–97. ISSN: 0191-8141. DOI: https://doi.org/10.1016/j.jsg.2016.11.005.

Pollard, D. D. and Aydin, A. (1988). "Progress in understanding jointing over the past century". In: *GSA Bulletin* 100.8, pp. 1181–1204. ISSN: 0016-7606. DOI: 10.1130/0016-7606(1988)100<1181:PIUJOT>2.3.CO;2.

Pollard, D. D. and Segall, P. (1987). "8 - THEORETICAL DISPLACEMENTS AND STRESSES NEAR FRACTURES IN ROCK: WITH APPLICATIONS TO FAULTS, JOINTS, VEINS, DIKES, AND SOLUTION SURFACES". In: ed. by B. K. B. T. F. M. o. R. ATKINSON. London: Academic Press, pp. 277–349. ISBN: 978-0-12-066266-1. DOI: https://doi.org/10.1016/B978-0-12-066266-1.50013-2.

Ponson, L., Auradou, H., Pessel, M., Lazarus, V., and Hulin, J.-P. (2007). "Failure mechanisms and surface roughness statistics of fractured Fontainebleau sandstone". In: *Physical Review E* 76.3, p. 36108. DOI: https://doi.org/10.1103/PhysRevE.76.036108.

Poropat, G. V. (2009). "Measurement of surface roughness of rock discontinuities". In: *Rock Engineering in Difficult Conditions*.

Power, W. L. and Tullis, T. E. (1991). "Euclidean and fractal models for the description of rock surface roughness". In: *Journal of Geophysical Research: Solid Earth* 96.B1, pp. 415–424. DOI: https://doi.org/10.1029/90JB02107.

Power, W. L., Tullis, T. E., Brown, S. R., Boitnott, G. N., and Scholz, C. H. (1987). "Roughness of natural fault surfaces". In: *Geophysical Research Letters* 14.1, pp. 29–32.

Priest, S. D. and Hudson, J. A. (1981). "Estimation of discontinuity spacing and trace length using scanline surveys". In: *International Journal of Rock Mechanics and Mining Sciences and* 18.3, pp. 183–197. ISSN: 01489062. DOI: 10.1016/0148-9062(81)90973-6.

Priest, S. D. (1993). *Discontinuity Analysis for Rock Engineering*. 1st ed. Springer, Dordrecht, p. 473. ISBN: 978-0-412-47600-6. DOI: https://doi.org/10.1007/978-94-011-1498-1.

Prodanovic, M., Landry, C., Tokan-Lawal, A., and Eichhubl, P. (2016). *Niobrara formation fracture. Retrieved March 01, 2021, from www.digitalrocksportal.org*. URL: doi:10.17612/P7SG6Zhttp://www.digitalrocksportal.org/projects/49.

Prodanovic, M., Bryant, S. L., and Karpyn, Z. T. (2009). "Investigating Matrix/Fracture Transfer via a Level Set Method for Drainage and Imbibition". In: *SPE Journal* 15.01, pp. 125–136. ISSN: 1086-055X. DOI: 10.2118/116110-PA.

Prodanovic, M., Esteva, M., Hanlon, M., Nanda, G., and Agarwal, P. (2015). *Digital Rocks Portal: a repository for porous media images*. DOI: http://dx.doi.org/10.17612/P7CC7K.

Przybycin, A. M., Scheck-Wenderoth, M., and Schneider, M. (2017). "The origin of deep geothermal anomalies in the German Molasse Basin: results from 3D numerical models of coupled fluid flow and heat transport". In: *Geothermal Energy* 5.1, p. 1. ISSN: 2195-9706. DOI: 10.1186/s40517-016-0059-3.

Pyrak-Nolte, L. J. and Nolte, D. D. (2016). "Approaching a universal scaling relationship between fracture stiffness and fluid flow". In: *Nature communications* 7, p. 10663. DOI: https://doi.org/10.1038/ncomms10663.

Räss, L., Kolyukhin, D., and Minakov, A. (2019). "Efficient parallel random field generator for large 3-D geophysical problems". In: *Computers & Geosciences* 131, pp. 158–169. ISSN: 0098-3004. DOI: https://doi.org/10.1016/j.cageo.2019.06.007.

Reeves, D. M., Benson, D. A., and Meerschaert, M. M. (2008). "Transport of conservative solutes in simulated fracture networks: 1. Synthetic data generation". In: *Water Resources Research* 44.5. DOI: 10.1029/2007WR006069.

Renard, F. and Candela, T. (2017). "Scaling of Fault Roughness and Implications for Earthquake Mechanics". In: *Fault Zone Dynamic Processes: Evolution of Fault Properties During Seismic Rupture*, pp. 195–215.

Renard, F., Voisin, C., Marsan, D., and Schmittbuhl, J. (2006). "High resolution 3D laser scanner measurements of a strike-slip fault quantify its morphological anisotropy at all scales". In: *Geophysical Research Letters* 33.4. DOI: https://doi.org/10.1029/2005GL025038.

Renard, P. and De Marsily, G. (1997). *Calculating equivalent permeability: A review*. DOI: 10.1016/s0309-1708(96)00050-4.

Renshaw, C. E. and Park, J. C. (1997). "Effect of mechanical interactions on the scaling of fracture length and aperture". In: *Nature* 386.6624, pp. 482–484. ISSN: 1476-4687. DOI: 10.1038/386482a0.

Renshaw, C. E. (1995). "On the relationship between mechanical and hydraulic apertures in rough-walled fractures". In: *Journal of Geophysical Research: Solid Earth* 100.B12, pp. 24629–24636. DOI: 10.1029/95JB02159.

Rodrigues, O. (1840). "Des lois géométriques qui régissent les déplacements d'un système solide dans l'espace: et de la variation des cordonnées provenant de ces déplacements considérés indépendamment des causes qui peuvent les produire". In: *Journal de mathématiques pures et appliquées 1re série, tome 5*, pp. . 380–440.

Rutqvist, J., Leung, C., Hoch, A., Wang, Y., and Wang, Z. (2013). "Linked multicontinuum and crack tensor approach for modeling of coupled geomechanics, fluid flow and transport in fractured rock". In: *Journal of Rock Mechanics and Geotechnical Engineering* 5.1, pp. 18–31. ISSN: 1674-7755. DOI: 10.1016/j.jrmge.2012.08.001.

Schepp, L. L., Ahrens, B., Balcewicz, M., Duda, M., Nehler, M., Osorno, M., Uribe, D., Steeb, H., Nigon, B., Stöckhert, F., Swanson, D. A., Siegert, M., Gurris, M., and Saenger, E. H. (2020). "Digital rock physics and laboratory considerations on a high-porosity volcanic rock". In: *Scientific Reports* 10.1, p. 5840. ISSN: 2045-2322. DOI: 10.1038/s41598-020-62741-1.

Schmittbuhl, J., Gentier, S., and Roux, S. (1993). "Field measurements of the roughness of fault surfaces". In: *Geophysical Research Letters* 20.8, pp. 639–641. DOI: https://doi.org/10.1029/93GL00170.

Schmittbuhl, J., Schmitt, F., and Scholz, C. (1995). "Scaling invariance of crack surfaces". In: *Journal of Geophysical Research: Solid Earth* 100.B4, pp. 5953–5973. DOI: https://doi.org/10.1029/94JB02885.

Schneider, C. A., Rasband, W. S., and Eliceiri, K. W. (2012). "NIH Image to ImageJ: 25 years of image analysis". In: *Nature Methods* 9.7, pp. 671–675. ISSN: 1548-7105. DOI: 10.1038/nmeth.2089.

Schroeder, W., Martin, K., and Lorensen, B. (2006). *The Visualization Toolkit (4th ed.), Kitware*. ISBN: ISBN 978-1-930934-19-1.

Schultz, R. A., Soliva, R., Fossen, H., Okubo, C. H., and Reeves, D. M. (2008). "Dependence of displacement-length scaling relations for fractures and deformation bands on the volumetric changes across them". In: *Journal of Structural Geology* 30.11, pp. 1405–1411. ISSN: 01918141. DOI: 10.1016/j.jsg.2008.08.001.

Scibek, J. (2020). "Multidisciplinary database of permeability of fault zones and surrounding protolith rocks at world-wide sites". In: *Scientific Data* 7.1, p. 95. ISSN: 2052-4463. DOI: 10.1038/s41597-020-0435-5.

Serra, O. and Serra, L. (2004). *Well logging—Data acquisition and applications: Mery Corbon*. Editions Serralog, France.

Shalaby, M. R. and Islam, M. A. (2017). "Fracture detection using conventional well logging in carbonate Matulla Formation, Geisum oil field, southern Gulf of Suez, Egypt". In: *Journal of Petroleum Exploration and Production Technology* 7.4, pp. 977–989. ISSN: 2190-0566. DOI: 10.1007/s13202-017-0343-1.

Shepard, M. K., Brackett, R. A., and Arvidson, R. E. (1995). "Self-affine (fractal) topography: Surface parameterization and radar scattering". In: *Journal of Geophysical Research: Planets* 100.E6, pp. 11709–11718. ISSN: 0148-0227. DOI: https://doi.org/10.1029/95JE00664.

SKB (1992). *SKB 91. Final disposal of spent nuclear fuel. Importance of the bedrock for safety*. URL: https://inis.iaea.org/search/search.aspx?orig{_}q=RN:24024040.

— (2010). *Data report for the safety assessment SR-Site, Technical Report SKB TR-10-52*. Technical Report TR-10-52. Swedish Nuclear Fuel and Waste Management Co., Stockholm, Sweden.

Smeraglia, L., Mercuri, M., Tavani, S., Pignalosa, A., Kettermann, M., Billi, A., and Carminati, E. (2021). "3D Discrete Fracture Network (DFN) models of damage zone fluid corridors within a reservoir-scale normal fault in carbonates: Multiscale approach using field data

and UAV imagery". In: *Marine and Petroleum Geology* 126, p. 104902. ISSN: 02648172. DOI: 10.1016/j.marpetgeo.2021.104902.

Snow, D. T. (1969). "Anisotropie permeability of fractured media". In: *Water Resources Research* 5.6, pp. 1273–1289. DOI: 10.1029/WR005i006p01273.

St-Onge, G., Mulder, T., Francus, P., and Long, B. (2007). *Continuous Physical Properties of Cored Marine Sediments*. DOI: 10.1016/S1572-5480(07)01007-X.

Strikwerda, J. C. (1984). "Finite Difference Methods for the Stokes and Navier–Stokes Equations". In: *SIAM Journal on Scientific and Statistical Computing* 5.1, pp. 56–68. ISSN: 0196-5204. DOI: 10.1137/0905004.

Svensson, U. (2001). "A continuum representation of fracture networks. Part I: Method and basic test cases". In: *Journal of Hydrology* 250.1, pp. 170–186. ISSN: 0022-1694. DOI: 10.1016/S0022-1694(01)00435-8.

Sweeney, M. R., Gable, C. W., Karra, S., Stauffer, P. H., Pawar, R. J., and Hyman, J. D. (2020). "Upscaled discrete fracture matrix model (UDFM): an octree-refined continuum representation of fractured porous media". In: *Computational Geosciences* 24.1, pp. 293–310. DOI: 10.1007/s10596-019-09921-9.

Thacker, B. H., Doebling, S. W., Hemez, F. M., Anderson, M. C., Pepin, J. E., and Rodriguez, E. A. (2004). "Concepts of Model Verification and Validation". In: DOI: 10.2172/835920.

Tokan-Lawal, A., Prodanovic, M., Landry, C. J., and Eichhubl, P. (2014). *Understanding Tortuosity and Permeability Variations in Naturally Fractured Reservoirs: Niobrara Formation*. DOI: 10.15530/URTEC-2014-1922870.

Tokan-Lawal, A., Prodanović, M., Landry, C. J., and Eichhubl, P. (2017). "Influence of Numerical Cementation on Multiphase Displacement in Rough Fractures". In: *Transport in Porous Media* 116.1, pp. 275–293. ISSN: 1573-1634. DOI: 10.1007/s11242-016-0773-0.

Torbert, S. (2016). *Applied computer science*. Springer. DOI: https://doi.org/10.1007/978-3-319-30866-1.

Volatili, T., Zambrano, M., Cilona, A., Huisman, B. A., Rustichelli, A., Giorgioni, M., Vittori, S., and Tondi, E. (2019). "From fracture analysis to flow simulations in fractured carbonates: The case study of the Roman Valley Quarry (Majella Mountain, Italy)". In: *Marine and Petroleum Geology* 100, pp. 95–110. ISSN: 02648172. DOI: 10.1016/j.marpetgeo.2018.10.040.

Vrolijk, P. J., Urai, J. L., and Kettermann, M. (2016). *Clay smear: Review of mechanisms and applications*. DOI: 10.1016/j.jsg.2015.09.006.

Wang, J. S. Y., Narasimhan, T. N., and Scholz, C. H. (1988). "Aperture correlation of a fractal fracture". In: *Journal of Geophysical Research: Solid Earth* 93.B3, pp. 2216–2224. ISSN: 0148-0227. DOI: https://doi.org/10.1029/JB093iB03p02216.

Wang, X. (2005). *Stereological interpretation of rock fracture traces on borehole walls and other cylindrical surfaces*. URL: http://hdl.handle.net/10919/29105.

Warren, J. E. and Root, P. J. (1963). "The Behavior of Naturally Fractured Reservoirs". In: *Society of Petroleum Engineers Journal* 3.03, pp. 245–255. ISSN: 0197-7520. DOI: 10.2118/426-PA.

Watanabe, N., Hirano, N., and Tsuchiya, N. (2008). "Determination of aperture structure and fluid flow in a rock fracture by high-resolution numerical modeling on the basis of a flow-through experiment under confining pressure". In: *Water Resources Research* 44.6. ISSN: 0043-1397. DOI: https://doi.org/10.1029/2006WR005411.

Westoby, M. J., Brasington, J., Glasser, N. F., Hambrey, M. J., and Reynolds, J. M. (2012). "'Structure-from-Motion' photogrammetry: A low-cost, effective tool for geoscience applications". In: *Geomorphology* 179, pp. 300–314. ISSN: 0169555X. DOI: 10.1016/j.geomorph.2012.08.021.

Wibberley, C. A. J., Yielding, G., and Toro, G. D. (2008). *Recent advances in the understanding of fault zone internal structure: a review*. Ed. by C. A. J. Wibberley, W Kurz, J Imber, R. E. Holdsworth, and C Collettini. DOI: 10.1144/SP299.2.

Witherspoon, P. A., Wang, J. S. Y., Iwai, K., and Gale, J. E. (1980). "Validity of cubic law for fluid flow in a deformable rock fracture". In: *Water resources research* 16.6, pp. 1016–1024. DOI: 10.1029/WR016i006p01016.

Xu, C. and Dowd, P. (2010). "A new computer code for discrete fracture network modelling". In: *Computers and Geosciences* 36.3, pp. 292–301. ISSN: 0098-3004. DOI: 10.1016/j.cageo.2009.05.012.

Zambrano, M., Pitts, A. D., Salama, A., Volatili, T., Giorgioni, M., and Tondi, E. (2019). "Analysis of Fracture Roughness Control on Permeability Using SfM and Fluid Flow Simulations: Implications for Carbonate Reservoir Characterization". In: *Geofluids* 2019. Ed. by J. Jang, p. 4132386. ISSN: 1468-8115. DOI: 10.1155/2019/4132386.

Zeeb, C., Gomez-Rivas, E., Bons, P. D., Virgo, S., and Blum, P. (2013). "Fracture network evaluation program (FraNEP): A software for analyzing 2D fracture trace-line maps". In: *Computers and Geosciences* 60, pp. 11–22. ISSN: 00983004. DOI: 10.1016/j.cageo.2013.04.027.

Zhang, M., Prodanović, M., Mirabolghasemi, M., and Zhao, J. (2019). "3D Microscale Flow Simulation of Shear-Thinning Fluids in a Rough Fracture". In: *Transport in Porous Media* 128.1, pp. 243–269. ISSN: 1573-1634. DOI: 10.1007/s11242-019-01243-9.

Zhou, H., Li, L., and Jaime Gómez-Hernández, J (2010). "Three-dimensional hydraulic conductivity upscaling in groundwater modeling". In: *Computers and Geosciences* 36.10, pp. 1224–1235. ISSN: 0098-3004. DOI: https://doi.org/10.1016/j.cageo.2010.03.008.

Zienkiewicz, O. C. and Taylor, R. L. (2000). *The Finite Element Method, 5th ed.* Butterworth-Heinemann, Oxford.

Zimmerman, R. W. and Bodvarsson, G. S. (1996). "Hydraulic conductivity of rock fractures". In: *Transport in porous media* 23.1, pp. 1–30. DOI: 10.1007/BF00145263.

Zimmerman, R. W. and Main, I. (2004). "Hydromechanical behavior of fractured rocks". In: *International Geophysics Series.* 89, pp. 363–422.

Zou, L., Jing, L., and Cvetkovic, V. (2017). "Modeling of flow and mixing in 3D rough-walled rock fracture intersections". In: *Advances in Water Resources* 107, pp. 1–9. ISSN: 0309-1708. DOI: 10.1016/j.advwatres.2017.06.003.